On the kinetostatic optimization of revolute-coupled planar manipulators

D. Chablat [a,*], J. Angeles [b]

[a] *Institut de Recherche en Communications et Cybernètique de Nantes, 1, rue de la Noë, B.P. 6597, 44321 Nantes, France* [1]

[b] *Department of Mechanical Engineering and Centre for Intelligent Machines, McGill University, 817 Sherbrooke Street West, Montreal, Que., Canada H3A 2K6*

Abstract

Proposed in this paper is a kinetostatic performance index for the optimum dimensioning of planar manipulators of the serial type. The index is based on the concept of *distance* of the underlying Jacobian matrix to a given isotropic matrix that is used as a reference model for the purpose of performance evaluation. Applications of the index fall in the realm of design, but control applications are outlined. The paper focuses on planar manipulators, the basic concepts being currently extended to their three-dimensional counterparts. © 2002 Elsevier Science Ltd. All rights reserved.

1. Introduction

Various performance indices have been devised to assess the kinetostatic performance of serial manipulators. Among these, the concepts of *service angle* [1], *dexterous workspace* [2] and *manipulability* [3] are worth mentioning. All these different concepts allow the definition of the kinetostatic performance of a manipulator from correspondingly different viewpoints. However, with the exception of Yoshikawa's manipulability index [3], none of these considers the invertibility of the Jacobian matrix. A dimensionless quality index was recently introduced by Lee et al. [4] based on the ratio of the Jacobian determinant to its maximum absolute value, as applicable to parallel manipulators. This index does not take into account the location of the operation point in

---

[*] Corresponding author. Tel.: +33-02-40-37-69-54; fax: +33-02-40-37-69-30.

E-mail addresses: damien.chablat@irccyn.ec-nantes.fr (D. Chablat), angeles@cim.mcgill.ca (J. Angeles).

[1] *URLS:* (D. Chablat), www.cim.mcgill.ca (J. Angeles). IRCCyN: UMR 6597 CNRS, Ecole Centrale de Nantes, Universite de Nantes, Ecole des Mines de Nantes.

the end-effector, for the Jacobian determinant is independent of this location. The proof of the foregoing fact is available in [5], as pertaining to serial manipulators, its extension to their parallel counterparts being straightforward. The *condition number* of a given matrix is well known to provide a measure of invertibility of the matrix [6]. It is thus natural that this concept found its way in this context. Indeed, the condition number of the Jacobian matrix was proposed by Salisbury and Craig [7] as a figure of merit to minimize when designing manipulators for maximum accuracy. In fact, the condition number gives, for a square matrix, a measure of the relative roundoff-error amplification of the computed results [6] with respect to the data roundoff-error. As is well known, however, the dimensional inhomogeneity of the entries of the Jacobian matrix prevents the straightforward application of the condition number as a measure of Jacobian invertibility. The *characteristic length* was introduced in [8] to cope with the above-mentioned inhomogeneity. Apparently, nevertheless, this concept has found strong opposition within some circles, mainly because of the lack of a direct geometric interpretation of the concept. It is the aim of this paper to shed more light on this debate, while proposing a novel performance index that lends itself to a straightforward manipulation and leads to sound geometric relations. Briefly stated, the performance index proposed here is based on the concept of *distance* in the space of $m \times n$ matrices, which is based, in turn, on the concept of inner product of this space. The performance index underlying this paper thus measures the distance of a given Jacobian matrix from an isotropic matrix of the same gestalt. With the purpose of rendering the Jacobian matrix dimensionally homogeneous, we resort to the concept of posture-dependent *conditioning length*. Thus, given at an arbitrary serial manipulator in an arbitrary posture, it is possible to define a unique length that renders this matrix dimensionally homogeneous and of minimum distance to isotropy. The characteristic length of the manipulator is then defined as the conditioning length corresponding to the posture that renders the above-mentioned distance a minimum over all possible manipulator postures. This paper is devoted to planar manipulators, the concepts being currently extended to spatial ones.

2. Algebraic background

Given two arbitrary $m \times n$ matrices **A** and **B** of real entries, their inner product, represented by $(\mathbf{A}, \mathbf{B})$, is defined as

$$(\mathbf{A}, \mathbf{B}) \equiv \mathrm{tr}(\mathbf{AWB}^{\mathrm{T}}), \tag{1}$$

where **W** is a *positive-definite* $n \times n$ weighting matrix that is introduced to allow for suitable normalization. The entries of **W** need not be dimensionally homogeneous, and, in fact, they should not if **A** and **B** are not. However, the product $\mathbf{AWB}^{\mathrm{T}}$ must be dimensionally homogeneous; else, its trace is meaningless. The *norm* of the space of $m \times n$ matrices induced by the above inner product is thus the *Frobenius norm*, namely,

$$\|\mathbf{A}\|^2 = \mathrm{tr}(\mathbf{AWA}^{\mathrm{T}}). \tag{2a}$$

Moreover, we shall be handling only nondimensional matrix entries, and hence, we choose **W** nondimensional as well, and so as to yield a value of unity for the norm of the $n \times n$ identity matrix **1**. Hence,

$$\mathbf{W} \equiv \frac{1}{n}\mathbf{1}. \tag{2b}$$

The foregoing inner product is thus expressed as

$$(\mathbf{A}, \mathbf{B}) \equiv \frac{1}{n}\mathrm{tr}(\mathbf{A}\mathbf{B}^{\mathrm{T}}). \tag{2c}$$

Henceforth we shall use only the Frobenius norm; for brevity, this will be simply referred to as the *norm* of a given matrix.

When comparing two dimensionless $m \times n$ matrices $\mathbf{A}$ and $\mathbf{B}$, we can define their distance $d(\mathbf{A}, \mathbf{B})$ as the Frobenius norm of their difference, namely,

$$d(\mathbf{A}, \mathbf{B}) \equiv \|\mathbf{A} - \mathbf{B}\|, \tag{3a}$$

i.e.,

$$d(\mathbf{A}, \mathbf{B}) \equiv \sqrt{\frac{1}{n}\mathrm{tr}\left[(\mathbf{A} - \mathbf{B})(\mathbf{A} - \mathbf{B})^{\mathrm{T}}\right]}. \tag{3b}$$

An $m \times n$ isotropic matrix, with $m < n$, is one with a singular value $\sigma > 0$ of multiplicity m, and hence, if the $m \times n$ matrix $\mathbf{C}$ is isotropic, then

$$\mathbf{C}\mathbf{C}^{\mathrm{T}} = \sigma^2\mathbf{1}, \tag{4}$$

where $\mathbf{1}$ is the $m \times m$ identity matrix. Note that the generalized inverse of $\mathbf{C}$ can be computed without a roundoff-error, for it is proportional to $\mathbf{C}^{\mathrm{T}}$, namely,

$$\left(\mathbf{C}\mathbf{C}^{\mathrm{T}}\right)^{-1}\mathbf{C}^{\mathrm{T}} = \frac{1}{\sigma^2}\mathbf{C}^{\mathrm{T}}. \tag{5}$$

Furthermore, the condition number $\kappa(\mathbf{A})$ of a square matrix $\mathbf{A}$ is defined [6] as

$$\kappa(\mathbf{A}) = \|\mathbf{A}\|\|\mathbf{A}^{-1}\|, \tag{6}$$

where *any* norm can be used. For the purpose of the paper, we shall use the Frobenius norm for matrices and the Euclidean norm for vectors. Henceforth we assume, moreover, a planar n-revolute manipulator, as depicted in Fig. 1, with Jacobian matrix $\mathbf{J}$ given in [5] as
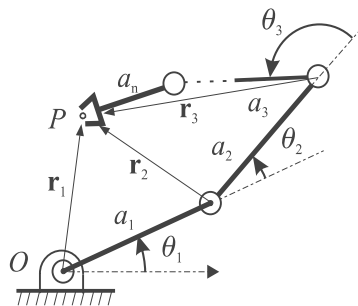

Fig. 1. Planar *n*-revolute manipulator.

$$\mathbf{J} = \begin{bmatrix} 1 & 1 & \cdots & 1 \\ \mathbf{Er}_1 & \mathbf{Er}_2 & \cdots & \mathbf{Er}_n \end{bmatrix}, \tag{7}$$

where $\mathbf{r}_i$ is the vector directed from the center of the ith revolute to the operation point P of the end-effector, while matrix $\mathbf{E}$ is defined as

$$\mathbf{E} = \begin{bmatrix} 0 & -1 \\ 1 & 0 \end{bmatrix}, \tag{8}$$

i.e., $\mathbf{E}$ represents a counterclockwise rotation of $90°$. It will prove convenient to partition $\mathbf{J}$ in the form

$$\mathbf{J} = \begin{bmatrix} \mathbf{A} \\ \mathbf{B} \end{bmatrix}$$

with $\mathbf{A}$ and $\mathbf{B}$ defined as

$$\mathbf{A} = \begin{bmatrix} 1 & 1 & \cdots & 1 \end{bmatrix} \quad \text{and} \quad \mathbf{B} = \begin{bmatrix} \mathbf{Er}_1 & \mathbf{Er}_2 & \cdots & \mathbf{Er}_n \end{bmatrix}.$$

Therefore, while the entries of $\mathbf{A}$ are dimensionless, those of $\mathbf{B}$ have units of length. Thus, the sole singular value of $\mathbf{A}$, i.e. the nonnegative square root of the scalar of $\mathbf{AA}^{\mathrm{T}}$, is $\sqrt{n}$, and hence, dimensionless, and pertains to the mapping from joint-rates into end-effector angular velocity. The singular values of $\mathbf{B}$, which are the nonnegative square roots of the eigenvalues of $\mathbf{BB}^{\mathrm{T}}$, have units of length, and account for the mapping from joint-rates into operation-point velocity. It is thus apparent that the singular values of $\mathbf{J}$ have different dimensions and hence, it is impossible to compute $\kappa(\mathbf{J})$ as in Eq. (6), for the norm of $\mathbf{J}$, as defined in Eqs. (2a) and (2b), is meaningless. The normalization of the Jacobian for the purpose of rendering it dimensionless has been judged to be dependent on the normalizing length [9] . As a means to avoid the arbitrariness of the choice of that normalizing length, the characteristic length L was introduced in [10]. Since the calculation of L is based on the minimization of an objective function that is elusive to a straightforward geometric interpretation, namely, the condition number of the normalized Jacobian, the characteristic length has been found cumbersome to use in manipulator design. We introduce below the concept of *conditioning length* to render the Jacobian matrix dimensionless, which will allow us to define the characteristic length using a geometric approach. In the sequel, we will need the partial derivative of the trace of a square matrix $\mathbf{N}$ with respect to a scalar argument x of $\mathbf{N}$. The said derivative is readily obtained as

$$\frac{\partial}{\partial x} \operatorname{tr}(\mathbf{N}) = \operatorname{tr}\left(\frac{\partial \mathbf{N}}{\partial x}\right). \tag{9a}$$

Moreover, in some instances, we will need the partial derivative of a scalar function f of the matrix argument $\mathbf{N}$ with respect to the scalar x, which is, in turn, an argument of $\mathbf{N}$. In this case, the desired partial derivative is obtained by application of the *chain rule*:

$$\frac{\partial f}{\partial x} = \operatorname{tr}\left(\frac{\partial f}{\partial \mathbf{N}} \frac{\partial \mathbf{N}^{\mathrm{T}}}{\partial x}\right). \tag{9b}$$

In particular, when $f(\mathbf{N})$ is the kth *moment* N_k of $\mathbf{N}$ with respect to x, defined as

$$N_k \equiv \operatorname{tr}(\mathbf{N}^k), \tag{9c}$$

the partial derivative of N_k with respect to x is given by

$$\frac{\partial N_k}{\partial x} = k \operatorname{tr}\left(\mathbf{N}^{k-1}\frac{\partial \mathbf{N}^{\mathrm{T}}}{\partial x}\right). \tag{9d}$$

Furthermore, we recall that the trace of any square matrix $\mathbf{N}$ equals that of its transpose, i.e.,

$$\operatorname{tr}(\mathbf{N}^{\mathrm{T}}) = \operatorname{tr}(\mathbf{N}) \tag{10}$$

and, finally, the trace of a product of various matrices compatible under multiplication does not change under a cyclic permutation of the factors, i.e., if $\mathbf{A}$, $\mathbf{B}$, and $\mathbf{C}$ are three matrices whose product $\mathbf{ABC}$ is possible and square, then $\operatorname{tr}(\mathbf{ABC}) = \operatorname{tr}(\mathbf{BCA}) = \operatorname{tr}(\mathbf{CAB})$.

3. Isotropic sets of points

Consider the set $\mathscr{S} \equiv \{P_k\}_1^n$ of n points in the plane, of position vectors $\{\mathbf{p}_k\}_1^n$ and centroid C, of position vector $\mathbf{c}$, i.e.,

$$\mathbf{c} \equiv \frac{1}{n}\sum_1^n \mathbf{p}_k. \tag{11}$$

The summation appearing in the right-hand side of the above expression is known as the *first moment of $\mathscr{S}$ with respect to the origin O* from which the position vectors stem. The *second moment of $\mathscr{S}$ with respect to C* is defined as a tensor $\mathbf{M}$, namely,

$$\mathbf{M} \equiv \sum_1^n (\mathbf{p}_k - \mathbf{c})(\mathbf{p}_k - \mathbf{c})^{\mathrm{T}}. \tag{12}$$

It is now apparent that the *root-mean-square* value of the distances $\{d_k\}_1^n$ of $\mathscr{S}$, d_{rms}, to the centroid is directly related to the trace of $\mathbf{M}$, namely,

$$d_{\mathrm{rms}} = \sqrt{\frac{1}{n}\sum_1^n (\mathbf{p}_k - \mathbf{c})^{\mathrm{T}}(\mathbf{p}_k - \mathbf{c})} \equiv \sqrt{\frac{1}{n}\operatorname{tr}(\mathbf{M})}. \tag{13}$$

Further, the *moment of inertia* $\mathbf{I}$ of $\mathscr{S}$ with respect to the centroid is defined as that of a set of unit masses located at the points of $\mathscr{S}$, i.e.,

$$\mathbf{I} \equiv \sum_1^n \left[\|\mathbf{p}_k - \mathbf{c}\|^2 \mathbf{1} - (\mathbf{p}_k - \mathbf{c})(\mathbf{p}_k - \mathbf{c})^{\mathrm{T}}\right] \tag{14a}$$

in which $\mathbf{1}$ is the 2×2 identity matrix. Hence, in light of definitions (12) and (13),

$$\mathbf{I} = \operatorname{tr}(\mathbf{M})\mathbf{1} - \mathbf{M}. \tag{14b}$$

We shall refer to $\mathbf{I}$ as the *geometric moment of inertia* of $\mathscr{S}$ about its centroid. It is now apparent that $\mathbf{I}$ is composed of two parts, an isotropic matrix of norm $\operatorname{tr}(\mathbf{M})$ and the second moment of $\mathscr{S}$ with the sign reversed. Moreover, the moment of inertia $\mathbf{I}$ can be expressed in a form that is more explicitly dependent upon the set $\{\mathbf{p}_k - \mathbf{c}\}_1^n$, if we recall the concept of *cross-product matrix* [5],

Briefly stated, for any three-dimensional vector $\mathbf{v}$, we define the cross-product matrix $\mathbf{P}_k$ of $(\mathbf{p}_k - \mathbf{c})$, or of any other three-dimensional vector for that matter, as

$$\mathbf{P}_k \equiv \frac{\partial[(\mathbf{p}_k - \mathbf{c}) \times \mathbf{v}]}{\partial \mathbf{v}}. \tag{15a}$$

Further, we recall the identity [5]

$$\mathbf{P}_k^2 \equiv -\|\mathbf{p}_k - \mathbf{c}\|^2 \mathbf{1} + (\mathbf{p}_k - \mathbf{c})(\mathbf{p}_k - \mathbf{c})^{\mathrm{T}}. \tag{15b}$$

It is now apparent that the moment of inertia of $\mathscr{S}$ takes the simple form

$$\mathbf{I} = -\sum_1^n \mathbf{P}_k^2. \tag{16}$$

We thus have:

Definition 1 (*Isotropic set*). The set $\mathscr{S}$ is said to be isotropic if its second-moment tensor with respect to its centroid is isotropic.

As a consequence, we have:

Lemma 1. *The geometric moment of inertia of an isotropic set of points about its centroid is isotropic.*

3.1. Geometric properties of isotropic sets of points

We describe below some properties of isotropic sets of points that will help us better visualize the results that follow.

3.1.1. Union of two isotropic sets of points

Consider two isotropic sets of points in the plane, $\mathscr{S}_1 = \{P_k\}_1^n$ and $\mathscr{S}_2 = \{P_k\}_{n+1}^{n+m}$. If the centroid C of the position vector $\mathbf{c}$ of $\mathscr{S}_1$ coincides with that of $\mathscr{S}_2$, i.e., if

$$\mathbf{c} \equiv \frac{1}{n} \sum_1^n \mathbf{p}_k \equiv \frac{1}{m} \sum_{n+1}^{n+m} \mathbf{p}_k, \tag{17}$$

then the set $\mathscr{S} = \mathscr{S}_1 \cup \mathscr{S}_2$ is isotropic.

For example, let $\mathscr{S}_1$ be a set of three isotropic points and $\mathscr{S}_2$ a set of four isotropic points, as displayed in Fig. 2, i.e.,

$$\mathscr{S}_1 = \left\{ \begin{bmatrix} -\sqrt{6}/2 \\ -\sqrt{2}/2 \end{bmatrix}, \begin{bmatrix} \sqrt{6}/2 \\ -\sqrt{2}/2 \end{bmatrix}, \begin{bmatrix} 0 \\ \sqrt{2} \end{bmatrix} \right\},$$

$$\mathscr{S}_2 = \left\{ \begin{bmatrix} 0 \\ -\sqrt{2} \end{bmatrix}, \begin{bmatrix} -\sqrt{2} \\ 0 \end{bmatrix}, \begin{bmatrix} 0 \\ \sqrt{2} \end{bmatrix}, \begin{bmatrix} \sqrt{2} \\ 0 \end{bmatrix} \right\}, \tag{18a}$$
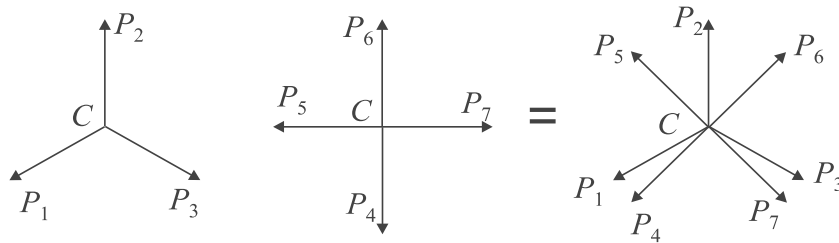
Fig. 2. Union of two isotropic sets of points.

where the centroid C is the origin. The second moment of $\mathscr{S}$ with respect to C is isotropic, namely,

$$\mathbf{M} \equiv \sum_{1}^{3+4}(\mathbf{p}_k - \mathbf{c})(\mathbf{p}_k - \mathbf{c})^{\mathrm{T}} = \begin{bmatrix} 7 & 0 \\ 0 & 7 \end{bmatrix} = (7)\mathbf{1}, \tag{18b}$$

where $\mathbf{1}$ denotes the 2×2 identity matrix. Furthermore, the geometric moment of inertia of $\mathscr{S}$ is

$$\mathbf{1} = (14)\mathbf{1} - (7)\mathbf{1} = (7)\mathbf{1}.$$

We thus have:

Lemma 2. *The union of two isotropic sets of points sharing the same centroid is also isotropic.*

3.1.2. Rotation of an isotropic set of points

Let $\mathbf{R}$ denote a rotation matrix in the plane through an angle α, and $\mathscr{S} = \{P_k\}_1^n$ a set of isotropic points. A new set of points $\mathscr{S}' = \{P'_k\}_1^n$ is defined upon rotating $\mathscr{S}$ through an angle α about C as a rigid body. The second moment of $\mathscr{S}'$ with respect to C is shown below to be isotropic as well. Indeed, letting this moment be $\mathbf{M}'$, we have

$$\mathbf{M}' \equiv \sum_{1}^{n} \left(\mathbf{p}'_k - \mathbf{c}'\right)\left(\mathbf{p}'_k - \mathbf{c}'\right)^{\mathrm{T}},$$

where, by definition,

$$\mathbf{p}'_k - \mathbf{c}' = \mathbf{R}(\mathbf{p}_k - \mathbf{c}).$$

Thus,

$$\mathbf{M}' \equiv \sum_{1}^{n} \mathbf{R}(\mathbf{p}_k - \mathbf{c})(\mathbf{p}_k - \mathbf{c})^{\mathrm{T}}\mathbf{R}^{\mathrm{T}} = \mathbf{R}\left[\sum_{1}^{n}(\mathbf{p}_k - \mathbf{c})(\mathbf{p}_k - \mathbf{c})^{\mathrm{T}}\right]\mathbf{R}^{\mathrm{T}}.$$

But the summation in brackets is the second moment $\mathbf{M}$ of the set $\mathscr{S}$, which is, by assumption, isotropic, and hence, takes the form

$$\mathbf{M} = \sum_{1}^{n}(\mathbf{p}_k - \mathbf{c})(\mathbf{p}_k - \mathbf{c})^{\mathrm{T}} = \sigma^2\mathbf{1}$$

for a real number $\sigma > 0$ and $\mathbf{1}$ denoting the 2×2 identity matrix. Hence,

$$\mathbf{M}' = \sigma^2\mathbf{R}\mathbf{R}^{\mathrm{T}} = \sigma^2\mathbf{1}$$

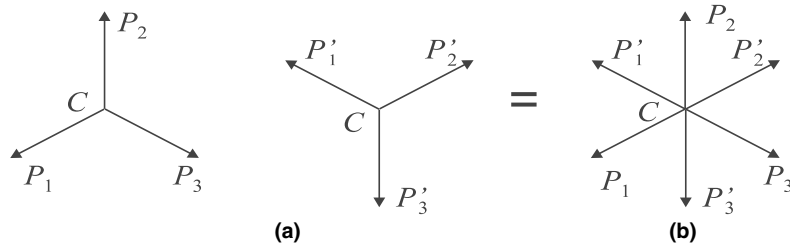thereby proving that the rotated set is isotropic as well. We thus have:

Fig. 3. (a) Rotation of an isotropic set $\mathscr{S}$ and (b) union of $\mathscr{S}$ with its rotated image.

Lemma 3. *The rotation of an isotropic set of points as a rigid body with respect to its centroid is also isotropic.*

The counterclockwise rotation of an isotropic set of three points, $\mathscr{S}$, through an angle of 60° and the union of the original set and its rotated counterpart are depicted in Fig. 3. Note that the union of the two sets is isotropic as well.

3.1.3. Trivial isotropic set of points

An isotropic set of points can be defined by the union or rotation, or a combination of both, of isotropic sets. The simplest set of isotropic points is the set of vertices of a regular polygon. We thus have:

Definition 2 (*Trivial isotropic set*). A set of *n* points $\mathscr{S}$ is called *trivial* if it is the set of vertices of a regular polygon with *n* vertices.

Trivial isotropic sets, $\mathscr{S} = \{P_k\}_1^n$, are depicted in Fig. 4 for $n = 3, \ldots, 6$.
Also note that:

Lemma 4. *A trivial isotropic set $\mathscr{S}$ remains isotropic under every reflection about an axis passing through the centroid C.*

4. An outline of kinematic chains

The connection between sets of points and planar manipulators of the serial type is the concept of *simple kinematic chain*. For completeness, we recall here some basic definitions pertaining to this concept.

4.1. Simple kinematic chains

The kinematics of manipulators is based on the concept of *kinematic chain*. A kinematic chain is a set of *rigid bodies*, also called *links*, coupled by *kinematic pairs*. In the case of planar chains, two lower kinematic pairs are possible, with the revolute allowing pure rotation of the two coupled links, and the prismatic pair allowing a pure relative translation, along one direction, of the same
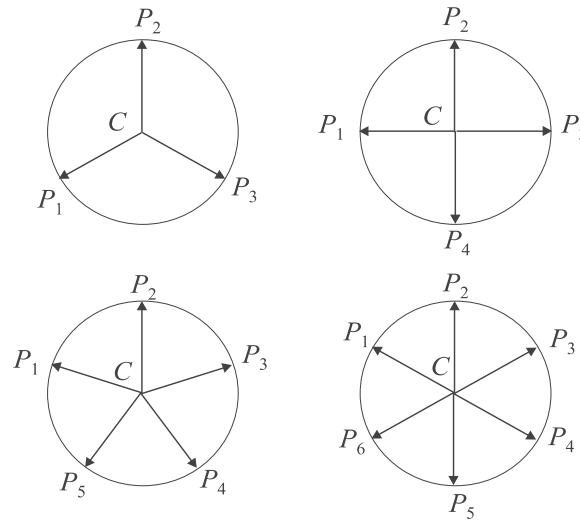
Fig. 4. Trivial isotropic sets for $n = 3, \ldots, 6$.

links. For the purpose of this paper, we study only revolute pairs, but prismatic pairs are also common in manipulators.

Definition 3 (*Simple kinematic chain*). A kinematic chain is said to be simple if each and every one of its links is coupled to at most two other links.

A simple kinematic chain can be *open* or *closed*; in studying serial manipulators we are interested in the former. In such a chain, we distinguish exactly two links, the terminal ones, coupled to only one other link. These links are thus said to be *simple*, with all other links being *binary*. In the context of manipulator kinematics, one terminal link is arbitrarily designated as *fixed*, with the other terminal link being the *end-effector* (EE), which is the one executing the task at hand. The task is defined, in turn, as a sequence of poses – positions and orientations – of the EE, with the position being given at a specific point P of the EE that we term the *operation point*.

4.2. Isotropic kinematic chains

To every set $\mathscr{S}$ of n points it is possible to associate a number of kinematic chains. To do this, we number the points from 1 to n, thereby defining $n - 1$ links, the ith link carrying joints i and $i + 1$. Links are thus correspondingly numbered from 1 to n, the nth link, or EE, carrying joint n on its proximal (to the base) end and the operation point P on its distal end. Furthermore, we define an additional link, the base, which is numbered as 0.

It is now apparent that, since we can number a given set $\mathscr{S}$ of n points in $n!$ possible ways, we can associate $n!$ kinematic chains to the above set $\mathscr{S}$ of n points. Clearly, these chains are, in general, different, for the lengths of their links are different as well. Nevertheless, some pairs of identical chains in the foregoing set are possible.

Definition 4 (*Isotropic kinematic chain*). If the foregoing set $\mathscr{S}$ of n points is isotropic, and the operation point P is defined as the centroid of $\mathscr{S}$, then any kinematic chain stemming from $\mathscr{S}$ is isotropic.

5. The posture-dependent conditioning length of planar *n*-revolute manipulators

Under the assumption that the manipulator finds itself at a *posture* $\mathscr{P}$ that is given by its set of joint angles, $\{\theta_k\}_1^n$, we start by dividing the last n rows of the Jacobian by a length $l_{\mathscr{P}}$, as yet to be determined. This length will be found so as to minimize the distance of the normalized Jacobian to a corresponding isotropic matrix **K**, subscript $\mathscr{P}$ reminding us that, as the manipulator changes its posture, so does the length $l_{\mathscr{P}}$. This length will be termed the *conditioning length* of the manipulator at $\mathscr{P}$.

5.1. A dimensionally homogeneous Jacobian matrix

In order to distinguish the original Jacobian matrix from its dimensionally homogeneous counterpart, we shall denote the latter by $\overline{\mathbf{J}}$, i.e.,

$$\overline{\mathbf{J}} = \begin{bmatrix} 1 & 1 & \cdots & 1 \\ (1/l_{\mathscr{P}})\mathbf{Er}_1 & (1/l_{\mathscr{P}})\mathbf{Er}_2 & \cdots & (1/l_{\mathscr{P}})\mathbf{Er}_n \end{bmatrix}.$$

Now the conditioning length will be defined via the minimization of the distance of the dimensionally homogeneous Jacobian matrix $\overline{\mathbf{J}}$ of an *n*-revolute manipulator to an isotropic $3 \times n$ model *matrix* **K** whose entries are dimensionless and has the same gestalt as any $3 \times n$ Jacobian matrix. To this end, we define an isotropic set $\mathscr{K} = \{K_i\}_1^n$ of n points in a *dimensionless* plane, of position vectors $\{\mathbf{k}_i\}_1^n$, which thus yields the dimensionless matrix

$$\mathbf{K} = \begin{bmatrix} 1 & 1 & \cdots & 1 \\ \mathbf{Ek}_1 & \mathbf{Ek}_2 & \cdots & \mathbf{Ek}_n \end{bmatrix}. \tag{19}$$

Further, we compute the product $\mathbf{KK}^{\mathrm{T}}$:

$$\mathbf{KK}^{\mathrm{T}} = \begin{bmatrix} n & \sum_1^n \mathbf{k}_i^{\mathrm{T}}\mathbf{E}^{\mathrm{T}} \\ \sum_1^n \mathbf{Ek}_i & \sum_1^n \mathbf{Ek}_i\mathbf{k}_i^{\mathrm{T}}\mathbf{E}^{\mathrm{T}} \end{bmatrix}.$$

Upon expansion of the summations occurring in the above matrix, we have

$$\sum_1^n \mathbf{k}_i\mathbf{E}^{\mathrm{T}} = \left(\sum_1^n \mathbf{Ek}_i \right)^{\mathrm{T}} = \mathbf{E}\left(\sum_1^n \mathbf{k}_i \right)^{\mathrm{T}}, \tag{20a}$$

$$\sum_1^n \mathbf{Ek}_i\mathbf{k}_i^{\mathrm{T}}\mathbf{E}^{\mathrm{T}} = \mathbf{E}\left(\sum_1^n \mathbf{k}_i\mathbf{k}_i^{\mathrm{T}} \right)\mathbf{E}^{\mathrm{T}}. \tag{20b}$$

Now, by virtue of the assumed isotropy of $\mathscr{K}$, the terms in parentheses in the foregoing expressions become

$$\sum_{1}^{n} \mathbf{k}_i = \mathbf{0},$$

$$\sum_{1}^{n} \mathbf{k}_i \mathbf{k}_i^{\mathrm{T}} = k^2 \mathbf{1}_{2\times2},$$

where the factor k^2 is as yet to be determined and $\mathbf{1}_{2\times2}$ denotes the 2×2 identity matrix. Hence, the product $\mathbf{KK}^{\mathrm{T}}$ takes the form

$$\mathbf{KK}^{\mathrm{T}} = \begin{bmatrix} n & \mathbf{0}^{\mathrm{T}} \\ 0 & k^2 \mathbf{1}_{2\times2} \end{bmatrix}. \tag{21}$$

Now, in order to determine k^2, we recall that matrix $\mathbf{K}$ is isotropic, and hence that the product $\mathbf{KK}^{\mathrm{T}}$ has a triple eigenvalue. It is now apparent that the triple eigenvalue of the said product must be n, which means that

$$k^2 = n, \tag{22}$$

and hence,

$$\sum_{1}^{n} \mathbf{k}_i \mathbf{k}_i^{\mathrm{T}} = (n) \mathbf{1}_{2\times2}.$$

5.2. Example 1. A three-DOF planar manipulator

Shown in Fig. 5(a) is an isotropic set $\mathscr{K}$ of three points, of position vectors $\{\mathbf{k}_i\}_1^n$, in a non-dimensional plane. The position vectors are given by

$$\mathbf{k}_1 = \frac{1}{2} \begin{bmatrix} \sqrt{6} \\ \sqrt{2} \end{bmatrix}, \quad \mathbf{k}_2 = \frac{1}{2} \begin{bmatrix} -\sqrt{6} \\ \sqrt{2} \end{bmatrix}, \quad \mathbf{k}_3 = \begin{bmatrix} 0 \\ -\sqrt{2} \end{bmatrix}. \tag{23a}$$

Hence, the corresponding model matrix is

$$\mathbf{K} = \begin{bmatrix} 1 & 1 & 1 \\ -\sqrt{2}/2 & -\sqrt{2}/2 & \sqrt{2} \\ \sqrt{6}/2 & -\sqrt{6}/2 & 0 \end{bmatrix}, \tag{23b}$$
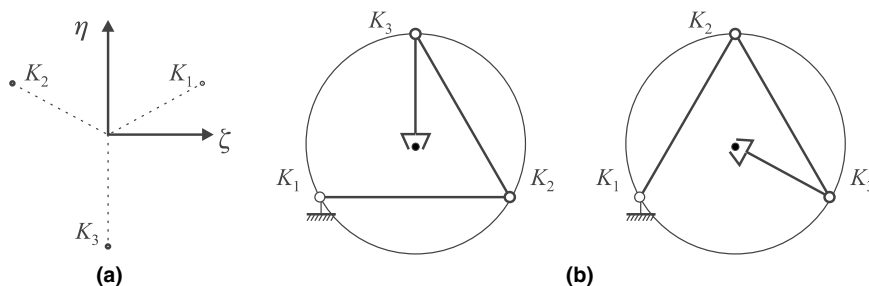

Fig. 5. Two isotropic manipulator postures stemming from the same isotropic set upon a relabelling of its points.

which can readily be proven to be isotropic, with a triple singular value of $k = \sqrt{3}$. When the order of the three vectors is changed, the isotropic condition is obviously preserved, for such a reordering amounts to nothing but a relabelling of the points of $\mathcal{K}$. Also note that two isotropic matrices $\mathbf{K}$ are associated with two symmetric postures, as displayed in Fig. 5(b).

5.3. Example 2. A four-DOF redundant planar manipulator

An isotropic set $\mathcal{K}$ of four points, $\{K_i\}_1^4$ is defined in a nondimensional plane, with position vectors $\mathbf{k}_i$ given below:

$$\mathbf{k}_1 = \begin{bmatrix} \sqrt{2} \\ \sqrt{2} \end{bmatrix}, \quad \mathbf{k}_2 = \begin{bmatrix} -\sqrt{2} \\ \sqrt{2} \end{bmatrix}, \quad \mathbf{k}_3 = \begin{bmatrix} -\sqrt{2} \\ -\sqrt{2} \end{bmatrix}, \quad \mathbf{k}_4 = \begin{bmatrix} \sqrt{2} \\ -\sqrt{2} \end{bmatrix}, \tag{24a}$$

which thus lead to

$$\mathbf{K} = \begin{bmatrix} 1 & 1 & 1 & 1 \\ -\sqrt{2} & -\sqrt{2} & \sqrt{2} & \sqrt{2} \\ \sqrt{2} & -\sqrt{2} & -\sqrt{2} & \sqrt{2} \end{bmatrix}. \tag{24b}$$

We thus have $4! = 24$ isotropic kinematic chains for a four-DOF planar manipulator, but we represent only 6 in Fig. 6 because the choice of the first point is immaterial, since this choice amounts to a rotation of the overall manipulator as a rigid body.
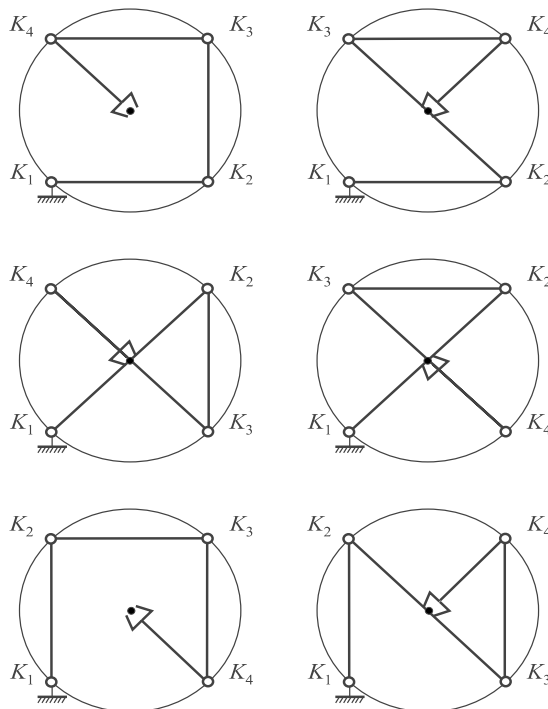

Fig. 6. Six isotropic postures for the same isotropic set.

5.4. Computation of the conditioning length

We can now formulate a least-square problem aimed at finding the conditioning length $l_{\mathscr{P}}$ that renders the distance from $\overline{\mathbf{J}}$ to $\mathbf{K}$ a minimum. The task will be eased if we work rather with the reciprocal of $l_{\mathscr{P}}$, $\lambda \equiv 1/l_{\mathscr{P}}$, and hence,

$$z \equiv \frac{1}{2}\frac{1}{n}\mathrm{tr}\left[(\overline{\mathbf{J}} - \mathbf{K})(\overline{\mathbf{J}} - \mathbf{K})^{\mathrm{T}}\right] \to \min_{\lambda}. \tag{25}$$

Upon expansion,

$$z = \frac{1}{2}\frac{1}{n}\mathrm{tr}\left(\overline{\mathbf{J}}\overline{\mathbf{J}}^{\mathrm{T}} - \overline{\mathbf{J}}\mathbf{K}^{\mathrm{T}} - \mathbf{K}\overline{\mathbf{J}}^{\mathrm{T}} + \mathbf{K}\mathbf{K}^{\mathrm{T}}\right).$$

Since the trace of a matrix equals that of its transpose, i.e.,

$$\mathrm{tr}\left(\overline{\mathbf{J}}\mathbf{K}^{\mathrm{T}}\right) = \mathrm{tr}\left(\mathbf{K}\overline{\mathbf{J}}^{\mathrm{T}}\right)$$

the foregoing expression for z reduces to

$$z \equiv \frac{1}{2}\frac{1}{n}\mathrm{tr}\left(\overline{\mathbf{J}}\overline{\mathbf{J}}^{\mathrm{T}} - 2\mathbf{K}\overline{\mathbf{J}}^{\mathrm{T}} + \mathbf{K}\mathbf{K}^{\mathrm{T}}\right). \tag{26}$$

It is noteworthy that the above minimization problem is (a) quadratic in λ, for $\overline{\mathbf{J}}$ is linear in λ and (b) unconstrained, which means that the problem accepts a unique solution. This solution can be found, additionally, in closed form. Indeed, the optimum value of λ is readily obtained upon setting up the normality condition of the above problem, namely,

$$\frac{\partial z}{\partial \lambda} \equiv \frac{1}{2n}\mathrm{tr}\left(\frac{\partial\left(\overline{\mathbf{J}}\overline{\mathbf{J}}^{\mathrm{T}}\right)}{\partial \lambda}\right) - \frac{1}{n}\mathrm{tr}\left(\mathbf{K}\frac{\partial\overline{\mathbf{J}}^{\mathrm{T}}}{\partial \lambda}\right) = 0, \tag{27}$$

where we have used the linearity property of the trace and the derivative operators. We calculate below the quantities involved:

$$\overline{\mathbf{J}}\overline{\mathbf{J}}^{\mathrm{T}} = \begin{bmatrix} n & \lambda\sum_1^n \mathbf{r}_j^{\mathrm{T}}\mathbf{E}^{\mathrm{T}} \\ \lambda\sum_1^n 3\mathbf{E}\mathbf{r}_j & \lambda^2\sum_1^n \mathbf{E}\mathbf{r}_j\mathbf{r}_j^{\mathrm{T}}\mathbf{E}^{\mathrm{T}} \end{bmatrix}, \quad \mathbf{K}\overline{\mathbf{J}}^{\mathrm{T}} = \begin{bmatrix} n & \lambda\sum_1^n \mathbf{r}_j^{\mathrm{T}}\mathbf{E}^{\mathrm{T}} \\ \sum_1^n \mathbf{E}\mathbf{k}_j & \lambda\sum_1^n \mathbf{E}\mathbf{k}_j\mathbf{r}_j^{\mathrm{T}}\mathbf{E}^{\mathrm{T}} \end{bmatrix}.$$

Thus,

$$\frac{\partial\left(\overline{\mathbf{J}}\overline{\mathbf{J}}^{\mathrm{T}}\right)}{\partial \lambda} = \begin{bmatrix} 0 & \sum_1^n \mathbf{r}_j^{\mathrm{T}}\mathbf{E}^{\mathrm{T}} \\ \sum_1^n \mathbf{E}\mathbf{r}_j & 2\lambda\sum_1^n \mathbf{E}\mathbf{r}_j\mathbf{r}_j^{\mathrm{T}}\mathbf{E}^{\mathrm{T}} \end{bmatrix}, \quad \mathbf{K}\frac{\partial\overline{\mathbf{J}}^{\mathrm{T}}}{\partial \lambda} = \begin{bmatrix} 0 & \sum_1^n \mathbf{r}_j^{\mathrm{T}}\mathbf{E}^{\mathrm{T}} \\ \mathbf{0} & \sum_1^n \mathbf{E}\mathbf{k}_j\mathbf{r}_j^{\mathrm{T}}\mathbf{E}^{\mathrm{T}} \end{bmatrix},$$

whence the normality condition (27) becomes

$$\lambda\sum_1^n \|\mathbf{r}_j\|^2 - \sum_1^n \mathbf{k}_j^{\mathrm{T}}\mathbf{r}_j = 0.$$

Now, if we notice that $\|\mathbf{r}_j\|$ is the distance d_j from the operation point P to the center of the jth revolute, the first summation of the above equation yields nd_{rms}^2, with d_{rms} denoting the root-mean-square value of the set of distances $\{d_j\}_1^n$, and hence,
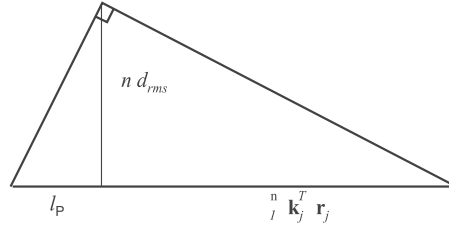
Fig. 7. A geometric interpretation of the conditioning length.

$$\lambda = \frac{\sum_1^n \mathbf{k}_i^{\mathrm{T}} \mathbf{r}_j}{nd_{\mathrm{rms}}^2} \quad \Rightarrow \quad l_{\mathscr{P}} = \frac{nd_{\mathrm{rms}}^2}{\sum_1^n \mathbf{k}_j^{\mathrm{T}} \mathbf{r}_j}. \tag{28}$$

Thus, the conditioning length is defined so that $\sqrt{n}d_{\mathrm{rms}}$ is the geometric mean between $l_{\mathscr{P}}$ and the sum of the projections of the set $\{\mathbf{r}_j\}_1^n$ onto the corresponding vectors of the set $\{\mathbf{k}_j\}_1^n$, as illustrated in Fig. 7.

5.5. A rotation of the isotropic set as a rigid body

Since a rigid-body rotation of a set of isotropic points preserves isotropy, we can find the orientation of this set, as parameterized by the angle of rotation α, that renders z a minimum, for a given manipulator posture. Let this rotation be $\mathbf{R}(\alpha)$, which can be expressed as [11]

$$\mathbf{R}(\alpha) = (\cos \alpha)\mathbf{1} + (\sin \alpha)\mathbf{E} \tag{29}$$

with $\mathbf{E}$ defined in Eq. (8). Thus, upon rotating the set $\mathscr{K}$ through an angle α about its centroid C or, equivalently, about the operation point P, the isotropic matrix $\mathbf{K}$ becomes $\tilde{\mathbf{K}}$, and is given by

$$\tilde{\mathbf{K}} = \begin{bmatrix} 1 & 1 & \cdots & 1 \\ \mathbf{E}\mathbf{R}(\alpha)\mathbf{k}_1 & \mathbf{E}\mathbf{R}(\alpha)\mathbf{k}_2 & \cdots & \mathbf{E}\mathbf{R}(\alpha)\mathbf{k}_n \end{bmatrix}. \tag{30a}$$

The objective function z then becomes

$$z = \frac{1}{2n}\left[\mathrm{tr}\left(\overline{\mathbf{J}}\overline{\mathbf{J}}^{\mathrm{T}}\right) - 2\mathbf{tr}\left(\overline{\mathbf{J}}\tilde{\mathbf{K}}^{\mathrm{T}}\right) + \mathbf{tr}\left(\tilde{\mathbf{K}}\tilde{\mathbf{K}}^{\mathrm{T}}\right)\right] \to \min_{\alpha}. \tag{30b}$$

Before setting up the normality conditions for the problem at hand, we note that

$$\tilde{\mathbf{K}}\tilde{\mathbf{K}}^{\mathrm{T}} = \begin{bmatrix} n & \left(\sum_1^n \mathbf{k}_i\right)^{\mathrm{T}}\mathbf{E}^{\mathrm{T}}\mathbf{R}^{\mathrm{T}}(\alpha) \\ \mathbf{R}(\alpha)\mathbf{E}\sum_1^n \mathbf{k}_i & \mathbf{R}(\alpha)\mathbf{E}\left(\sum_1^n \mathbf{k}_i\mathbf{k}_i^{\mathrm{T}}\right)\mathbf{E}^{\mathrm{T}}\mathbf{R}^{\mathrm{T}}(\alpha) \end{bmatrix}, \tag{31}$$

which can be shown to reduce to

$$\tilde{\mathbf{K}}\tilde{\mathbf{K}}^{\mathrm{T}} = \begin{bmatrix} n & \left(\sum_1^n \mathbf{k}_i\right)^{\mathrm{T}}\mathbf{E}^{\mathrm{T}}\mathbf{R}^{\mathrm{T}}(\alpha) \\ \mathbf{R}(\alpha)\mathbf{E}\sum_1^n \mathbf{k}_i & k^2\mathbf{1}_{2\times 2} \end{bmatrix},$$

and hence,

$$\frac{\partial\left[\text{tr}\left(\tilde{\mathbf{K}}\tilde{\mathbf{K}}^{\text{T}}\right)\right]}{\partial\alpha} = 0.$$

On the other hand, $\overline{\mathbf{J}}$ is independent of α, and hence, the normality condition of problem (30b) reduces to

$$\frac{\partial z}{\partial\alpha} \equiv -\frac{1}{n}\left[\text{tr}\left(\overline{\mathbf{J}}\frac{\partial\tilde{\mathbf{K}}^{\text{T}}}{\partial\alpha}\right)\right] = \mathbf{0}. \tag{32}$$

We calculate below the partial derivative required above:

$$\frac{\partial\tilde{\mathbf{K}}}{\partial\alpha} = \begin{bmatrix} 0 & 0 & \cdots & 0 \\ \mathbf{R}'(\alpha)\mathbf{E}\mathbf{k}_1 & \mathbf{R}'(\alpha)\mathbf{E}\mathbf{k}_2 & \cdots & \mathbf{R}'(\alpha)\mathbf{E}\mathbf{k}_n \end{bmatrix},$$

where $\mathbf{R}'(\alpha)$ can be expressed, in light of relation (29), as

$$\mathbf{R}'(\alpha) = \mathbf{E}\mathbf{R}(\alpha),$$

and hence,

$$\frac{\partial\tilde{\mathbf{K}}}{\partial\alpha} = \begin{bmatrix} 0 & 0 & \cdots & 0 \\ \mathbf{E}\mathbf{R}(\alpha)\mathbf{E}\mathbf{k}_1 & \mathbf{E}\mathbf{R}(\alpha)\mathbf{E}\mathbf{k}_2 & \cdots & \mathbf{E}\mathbf{R}(\alpha)\mathbf{E}\mathbf{k}_n \end{bmatrix}$$

whence,

$$\text{tr}\left(\overline{\mathbf{J}}\frac{\partial\tilde{\mathbf{K}}^{\text{T}}}{\partial\alpha}\right) = \lambda\,\text{tr}\left\{\sum_1^n\mathbf{E}\mathbf{r}_j\left[\mathbf{E}\mathbf{r}(\alpha)\mathbf{E}\mathbf{k}_j\right]^{\text{T}}\right\} = \lambda\sum_1^n\mathbf{r}_j^{\text{T}}\mathbf{E}^{\text{T}}\mathbf{E}\mathbf{R}(\alpha)\mathbf{E}\mathbf{K}_j = \lambda\sum_1^n\mathbf{r}_j^{\text{T}}\mathbf{R}(\alpha)\mathbf{E}\mathbf{k}_j.$$

Now, under the plausible assumption that $l_{\mathscr{P}}$ is finite, $\lambda \neq 0$, and hence, the normality condition (32) reduces to

$$\sum_1^n\mathbf{r}_j^{\text{T}}\mathbf{R}(\alpha)\mathbf{E}\mathbf{k}_j = 0.$$

Further, substitution of expression (29) into the above expression leads to

$$(\cos\alpha)\sum_1^n\mathbf{r}_j^{\text{T}}\mathbf{E}\mathbf{k}_j - (\sin\alpha)\sum_1^n\mathbf{r}_j^{\text{T}}\mathbf{k}_j = 0. \tag{33}$$

Therefore, the value of α minimizing the distance of $\overline{\mathbf{J}}$ to $\tilde{\mathbf{K}}(\alpha)$ is, for the given posture $\mathscr{P}$,

$$\alpha = \arctan\left[\frac{\sum_1^n\mathbf{r}_j^{\text{T}}\mathbf{E}\mathbf{k}_j}{\sum_1^n\mathbf{r}_j^{\text{T}}\mathbf{k}_j}\right] \equiv \arctan\left[\frac{(1/n)\sum_1^n\mathbf{r}_j^{\text{T}}\mathbf{E}\mathbf{k}_j}{(1/n)\sum_1^n\mathbf{r}_j^{\text{T}}\mathbf{k}_j}\right]. \tag{34}$$

Thus, the angle α through which the given isotropic set $\mathscr{K}$ is to be rotated in order to obtain the conditioning length of the manipulator pose $\mathscr{P}$ is given as the arctan function of the ratio of a numerator N to a denominator D, whose geometric interpretations are straightforward: D is simply the mean value of the projections of the $\mathbf{r}_j$ vectors onto their corresponding $\mathbf{k}_j$ vectors. Now, since $\mathbf{E}\mathbf{k}_j$ is vector $\mathbf{k}_j$ rotated 90° counterclockwise, N is the mean value of the projections of the $\mathbf{r}_j$ vectors onto their corresponding $\mathbf{E}\mathbf{k}_j$ vectors. We can call the latter the *transverse projections*

of the said vectors. Once we have found the optimum value α_{opt} of α for a given manipulator posture, we redefine, for conciseness,

$$\mathbf{K} \leftarrow \tilde{\mathbf{K}}(\alpha_{opt}). \tag{35}$$

With α_{opt} known, $l_{\mathscr{P}}$ is readily computed from Eq. (28). Now, if we regard the columns of $\overline{\mathbf{J}}$ and $\mathbf{K}$ as three-dimensional vectors, then a rotation $\mathbf{Q}$ of the corresponding three-dimensional space about an axis normal to the plane of the sets $\{\mathbf{r}_j\}_1^n$ and $\{\mathbf{k}_j\}_1^n$ through an angle q can be represented as

$$\mathbf{Q} = \begin{bmatrix} 1 & \mathbf{0}^T \\ \mathbf{0} & \mathbf{R}(q) \end{bmatrix},$$

where $\mathbf{R}(q)$ is a 2×2 rotation matrix similar to $\mathbf{R}(\alpha)$, as defined in Eq. (29). Hence, under rotation $\mathbf{Q}$, $\overline{\mathbf{J}}$ and $\mathbf{K}$ change as described below:

$$\begin{aligned}
\mathbf{Q}\overline{\mathbf{J}} &= \begin{bmatrix} 1 & \mathbf{0}^T \\ \mathbf{0} & \mathbf{R}(q) \end{bmatrix} \begin{bmatrix} 1 & 1 & \cdots & 1 \\ (1/l_{\mathscr{P}})\mathbf{E}\mathbf{r}_1 & (1/l_{\mathscr{P}})\mathbf{E}\mathbf{r}_2 & \cdots & (1/l_{\mathscr{P}})\mathbf{E}\mathbf{r}_n \end{bmatrix} \\
&= \begin{bmatrix} 1 & 1 & \cdots & 1 \\ \mathbf{R}(q)\mathbf{E}\mathbf{r}_1 & \mathbf{R}(q)\mathbf{E}\mathbf{r}_2 & \cdots & \mathbf{R}(q)\mathbf{E}\mathbf{r}_n \end{bmatrix}, \\
\mathbf{Q}\mathbf{K} &= \begin{bmatrix} 1 & 1 & \cdots & 1 \\ \mathbf{R}(q)\mathbf{E}\mathbf{k}_1 & \mathbf{R}(q)\mathbf{E}\mathbf{k}_2 & \cdots & \mathbf{R}(q)\mathbf{E}\mathbf{k}_n \end{bmatrix}.
\end{aligned}$$

Now it is apparent that z, as defined in Eq. (25), is invariant under a rotation $\mathbf{R}(q)$ of the sets $\mathscr{S}$ and $\mathscr{K}$. Indeed, under such a rotation,

$$\begin{aligned}
z_{\mathbf{Q}} &\equiv \frac{1}{2}\frac{1}{n}\text{tr}\left(\mathbf{Q}\overline{\mathbf{J}}\overline{\mathbf{J}}^T\mathbf{Q}^T - \mathbf{Q}\mathbf{K}\overline{\mathbf{J}}^T\mathbf{Q}^T - \mathbf{Q}\overline{\mathbf{J}}\mathbf{K}^T\mathbf{Q}^T + \mathbf{Q}\mathbf{K}\mathbf{K}^T\mathbf{Q}^T\right) \\
&= \frac{1}{2}\frac{1}{n}\text{tr}\left[\mathbf{Q}\left(\overline{\mathbf{J}}\overline{\mathbf{J}}^T - \mathbf{K}\overline{\mathbf{J}}^T - \overline{\mathbf{J}}\mathbf{K}^T + \mathbf{K}\mathbf{K}^T\right)\mathbf{Q}^T\right].
\end{aligned}$$

If we recall relation (10), the above expression becomes

$$z_{\mathbf{Q}} \equiv \frac{1}{2}\frac{1}{n}\text{tr}\left[\mathbf{Q}^T\mathbf{Q}\left(\overline{\mathbf{J}}\overline{\mathbf{J}}^T - \mathbf{K}\overline{\mathbf{J}}^T - \overline{\mathbf{J}}\mathbf{K}^T + \mathbf{K}\mathbf{K}^T\right)\right] = z. \tag{36}$$

We thus have proven:

Lemma 5. *The distance of $\overline{\mathbf{J}}$ to $\mathbf{K}$ is invariant under a rotation of the sets $\mathscr{S}$ and $\mathscr{K}$.*

5.6. The optimum posture

It is now apparent that we can always orient the $\mathscr{K}$ set optimally, so that, for any posture $\mathscr{P}$, $\overline{\mathbf{J}}$ lies at a minimum distance from the corresponding matrix $\mathbf{K}$. Moreover, by virtue of Lemma 5, a rotation of the whole manipulator as a rigid body about its first joint, i.e., a motion of the manipulator with all its joints but the first one locked, does not affect z. That is, z is a function of only $\{\theta_i\}_2^n$, which can thus be termed the set of *conditioning joint variables*, with the associated joints being the *conditioning joints*. Now we aim at finding the *optimum posture* $\mathscr{P}_o$ that yields a

dimensionless Jacobian $\overline{\mathbf{J}}$ lying at a minimum distance to the reference matrix $\mathbf{K}$. To this end, we adopt a given set $\mathcal{K}$ at a given orientation at the outset, which thus leads to a constant matrix $\mathbf{K}$ in the process of finding $\mathcal{P}_o$, with the optimum orientation of $\mathcal{K}$ being readily determined from Eq. (34) once $\mathcal{P}_o$ has been found. Thus, in the derivations that follow, θ_1 can be set arbitrarily equal to zero, or to any other constant value, for that matter. We now aim at solving the problem

$$z = \frac{1}{2}\frac{1}{n}\text{tr}\left(\overline{\mathbf{J}}\overline{\mathbf{J}}^{\text{T}} - 2\mathbf{K}\overline{\mathbf{J}}^{\text{T}} + \mathbf{K}\mathbf{K}^{\text{T}}\right) \to \min_{\{\theta_i\}_2^n}. \tag{37}$$

An attempt to solving this problem using the approach of the foregoing sections proved to be impractical. Indeed, since z depends on the set of conditioning joint variables both via the set $\{\mathbf{r}_j\}_1^n$ and via λ, this dependence leads to a normality condition that does not lend itself to a closed-form solution. As a consequence, the said normality condition does not lead to a direct geometric interpretation of the optimum posture.

We thus follow a different approach here. For each posture, the value of λ is computed using Eq. (28), while α is computed with Eq. (34). With the foregoing expressions substituted into the expression of z given in Eq. (37), the corresponding normality conditions for angles $\{\theta_i\}_2^n$ yield a system of algebraic equations in the foregoing conditioning variables that are amenable to solutions using modern methods, like polynomial continuation, Gröbner bases, or resultant methods [12], that yield all roots of the problem at hand. These roots then lead to the globally optimum posture $\mathcal{P}_o$.

5.7. The characteristic length

The optimum postures of a given manipulator, i.e., those with a Jacobian matrix closest to a corresponding model matrix $\mathbf{K}$ are thus found upon solving the optimization problem (37). Moreover, the conditioning length associated with the posture yielding a global minimum of the foregoing distance is defined as the *characteristic length* of the manipulator at hand. Prior to discussing some examples, we would like to find out whether the characteristic length thus found bears a minimality geometric property, e.g., whether the characteristic length is the minimum conditioning length of the manipulator over its whole workspace. To this end, we rewrite the objective function z in the form

$$z = \frac{1}{2n}\left(\lambda^2 n d_{\text{rms}}^2 - 2\lambda \sum_1^n \mathbf{k}_j^{\text{T}}\mathbf{r}_j + \sum_1^n \|\mathbf{k}_j\|^2\right). \tag{38}$$

Upon substitution of the sum $\sum_1^n \mathbf{k}_j^{\text{T}}\mathbf{r}_j$ in terms of the optimum value of λ found in Eq. (28) into Eq. (38), we obtain

$$z = \frac{1}{2n}\sum_1^n \|\mathbf{k}_j\|^2 - \frac{1}{2}\lambda^2 d_{\text{rms}}^2 \equiv \frac{1}{2n}\sum_1^n \|\mathbf{k}_j\|^2 - \frac{1}{2}\left(\frac{d_{\text{rms}}}{l_{\mathcal{P}}}\right)^2. \tag{39}$$

It is apparent from the above expression that minimizing z is not equivalent to minimizing $l_{\mathcal{P}}$, but rather to maximizing the ratio $d_{\text{rms}}/l_{\mathcal{P}}$. Hence, minimizing z is equivalent to minimizing the inverse ratio, i.e., $l_{\mathcal{P}}/d_{\text{rms}}$. In other words, minimizing z is equivalent to minimizing the ratio of the conditioning length to the rms value of the distances of the joint centers from the operation point.

5.8. Examples. A three-DOF planar manipulator

5.8.1. An isotropic manipulator

In the first example, we have $a_1 = a_2 = l$ and $a_3 = \sqrt{3}l/3$, with the $\{\mathbf{r}_j\}_1^3$ vectors given by

$$\mathbf{r}_1 = l \begin{bmatrix} \cos(\theta_1) + \cos(\theta_{12}) + \cos(\theta_{123}) \\ \sin(\theta_1) + \sin(\theta_{12}) + \sin(\theta_{123}) \end{bmatrix},$$

$$\mathbf{r}_2 = l \begin{bmatrix} \cos(\theta_{12}) + \cos(\theta_{123}) \\ \sin(\theta_{12}) + \sin(\theta_{123}) \end{bmatrix}, \quad \mathbf{r}_3 = \frac{\sqrt{3}l}{3} \begin{bmatrix} \cos(\theta_{123}) \\ \sin(\theta_{123}) \end{bmatrix}$$

with the definition $\theta_{ij\cdots p} \equiv \theta_i + \theta_j + \cdots + \theta_p$. Moreover, the model matrix $\mathbf{K}$ used for this case is that found for the case of an isotropic set of three points, as discussed in Section 5.2, and reproduced below for quick reference:

$$\mathbf{K} = \begin{bmatrix} 1 & 1 & 1 \\ -\sqrt{2}/2 & -\sqrt{2}/2 & \sqrt{2} \\ \sqrt{6}/2 & -\sqrt{6}/2 & 0 \end{bmatrix}. \tag{40}$$

One optimum posture found with the procedure discussed in Section 5.6 is displayed in Fig. 8, with the objective function attaining a minimum of zero at this posture, which means that the manipulator can match exactly an isotropic model matrix $\mathbf{K}$ within its workspace, with the manipulator thus being termed *isotropic*. The objective function attains the values displayed in Fig. 9 over its whole workspace.

At the optimum posture, we have the values of the joint variables given below:

$$\theta_1 = 0°, \quad \theta_2 = 120°, \quad \theta_3 = 150°$$

with the conditioning length $l_{\mathscr{P}}$ being equal to $(\sqrt{6}/6)l$, which is thus the characteristic length of this manipulator, as found using an alternative approach in [5]. Moreover, the normalized Jacobian $\overline{\mathbf{J}}$ becomes

$$\overline{\mathbf{J}} = \begin{bmatrix} 1 & 1 & 1 \\ -\sqrt{2}/2 & -\sqrt{2}/2 & \sqrt{2} \\ \sqrt{6}/2 & -\sqrt{6}/2 & 0 \end{bmatrix}.$$
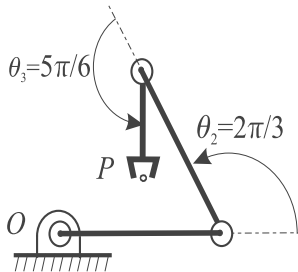
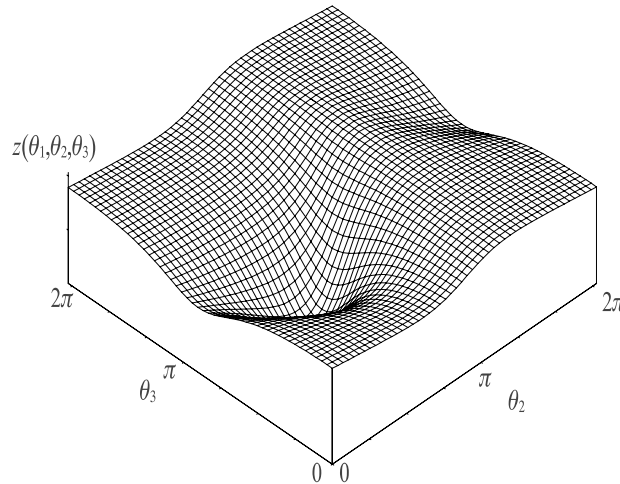Fig. 8. An isotropic posture with $\theta_1 = 0°$.

Fig. 9. Objective function of the isotropic manipulator.

5.8.2. An equilateral manipulator

In the second example, we assume that all the link lengths are equal to l, and hence,

$$\mathbf{r}_1 = l \begin{bmatrix} \cos(\theta_1) + \cos(\theta_{12}) + \cos(\theta_{123}) \\ \sin(\theta_1) + \sin(\theta_{12}) + \sin(\theta_{123}) \end{bmatrix},$$
$$\mathbf{r}_2 = l \begin{bmatrix} \cos(\theta_{12}) + \cos(\theta_{123}) \\ \sin(\theta_{12}) + \sin(\theta_{123}) \end{bmatrix}, \quad \mathbf{r}_3 = l \begin{bmatrix} \cos(\theta_{123}) \\ \sin(\theta_{123}) \end{bmatrix}. \tag{41}$$

We call this manipulator *equilateral*.

For this case, we use the same model matrix $\mathbf{K}$ that we used in the previous example, for the manipulator has the same number of joints, and only one $\mathbf{K}$ was found – up to a reflection – for this number of joints. The minimization of the objective function leads to the optimum values

$$\theta_1 = 0°, \quad \theta_2 = 81.8°, \quad \theta_3 = 155.2°,$$

which correspond to a minimum value of $z = 0.178$, with the associated characteristic length being $l_{\mathscr{P}} = 0.563l$. The corresponding posture is displayed in Fig. 10, while the objective function, evaluated throughout the workspace of the manipulator, is displayed in Fig. 11.
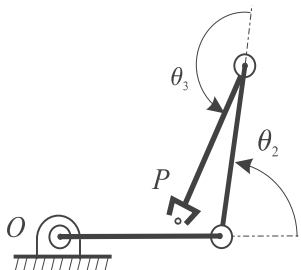
Fig. 10. The posture closest to isotropy with $\theta_1 = 0°$.
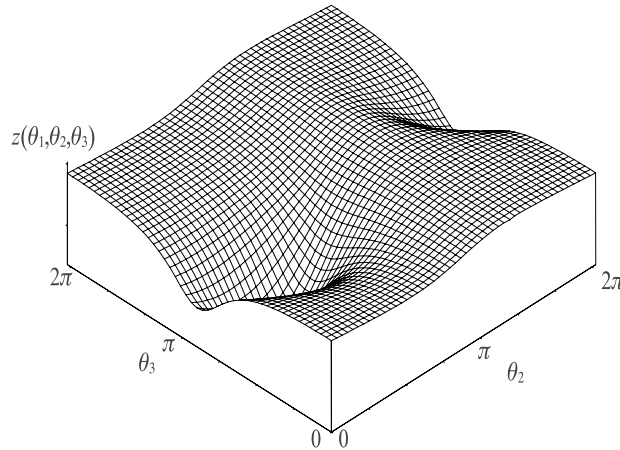
Fig. 11. Objective function of the equilateral manipulator.

Finally, the normalized Jacobian at the posture of Fig. 10 is

$$\bar{\mathbf{J}} = \begin{bmatrix} 1 & 1 & 1 \\ -0.268 & -0.268 & 1.489 \\ 1.061 & -0.714 & -0.966 \end{bmatrix}.$$

5.9. The isocontours of the objective function

The minimum of the objective function z corresponds to the posture closest to isotropy. At the other end of the spectrum, the maximum of this function is attained at those singular postures whereby the rank of the Jacobian matrix is 2. The curves of constant z-values, termed the *iso-contours* of the manipulator, can be used to define a performance index to compare manipulators, as described below. The isocontours were obtained with *Surfer*, a Surface Mapping System, for θ_2 and $\theta_3 \in [0, 2\pi]$. The isocontours of the isotropic manipulator, of the first example, are displayed in Fig. 12; those of the equilateral manipulator in Fig. 13.

It is apparent from the two foregoing figures that the isocontours can be closed or open. If closed, the curves enclose the optimum point in the space of conditioning joints; in the second case, the curves are periodic. The shape of the closed curves, additionally, provides useful information on the manipulator performance: For the isotropic manipulator, when the objective function is below 0.25, the curves are close to circular, as shown in Fig. 14; for the equilateral manipulator, these curves are close to elliptical, as shown in Fig. 15. This means that, in the neighborhood of an optimum, the isocontours behave in a way similar to the *manipulability ellipsoid* [3]: An isotropic manipulator entails a manipulability ellipsoid with semiaxes of identical lengths.

6. Applications to design and control

Manipulators are designed for a family of tasks, more so than for a specific task – manipulator design for a specific task defeats the purpose of using a manipulator, in the first place! The first
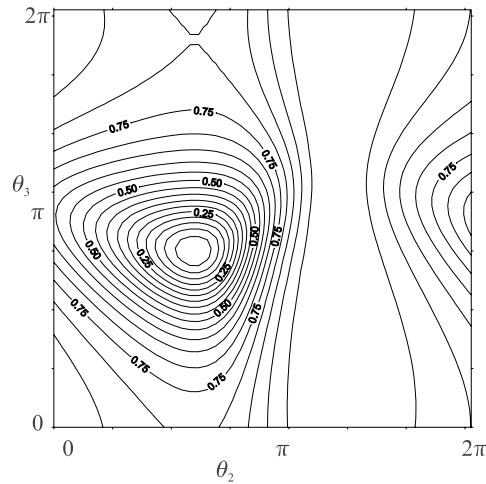
Fig. 12. The isocontours of the objective function of the isotropic manipulator.
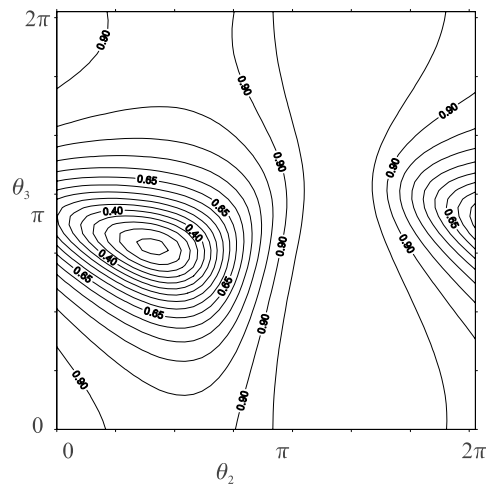

Fig. 13. The isocontours of the objective function of the equilateral manipulator.

step in designing a manipulator, moreover, is to dimension its links. It is apparent that from a purely geometric viewpoint, the link lengths are not as important as the link-length ratios. Once these ratios are optimally determined, the link lengths can be obtained based on requirements such as maximum reach for a given family of tasks, e.g., whether the manipulator is being used for cleaning a wide body or a regional aircraft. Now, the maximum reach is directly proportional to the d_{rms} value of the distance of the joint centers to the operation point at the optimum posture, and hence, we can obtain the optimum link-length ratios by assuming that d_{rms} is equal to one unit of length. This means that minimizing the objective function z, as given by Eq. (39), is equivalent to minimizing the normalized conditioning length $l_{\mathscr{P}}$, where the normalization is carried out upon
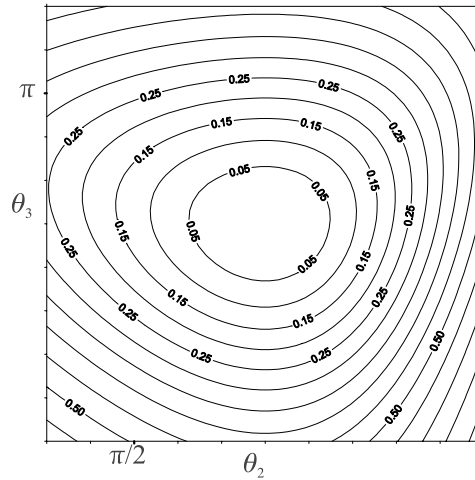
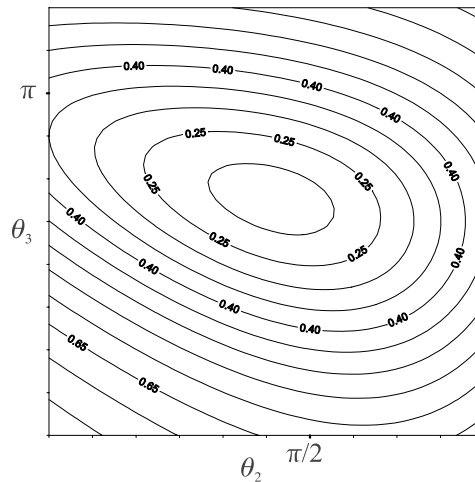Fig. 14. The isocontours closest to isotropy of the objective function of the isotropic manipulator.

Fig. 15. The isocontours closest to isotropy of the objective function of the equilateral manipulator.

dividing this length by d_{rms}. Furthermore, when deciding on the manipulator link-length ratios, we may specify a certain *useful workspace region* as a subset of the whole workspace. How to decide on the boundaries of this region is something that can be done based on the value of z, so that we can establish a maximum allowable value of z, say $z_M < z_{max}$ that we are willing to tolerate so as to keep the manipulator far enough from singularities. In this regard, the area enclosed by the isocontour $z = z_M$ will give a nondimensional measure, and hence, a measure independent of the scale of the manipulator, of the useful workspace region.

Under no constraints on the link-length ratios, for example, the designer should choose the optimum ratios of the isotropic manipulator of Fig. 8. On the other hand, when the manipulator is given, and it is desired to control it so as to keep it away from singularities, function z can be

used again as a measure of the distance to singularities: when z attains its global maximum, the manipulator finds itself at a rank-two singularity. A rank-one singularity occurs at a local maximum. Furthermore, if a manipulator of given link-length ratios – e.g., one out of a family of manipulators with identical architectures, but of different scales, like the Puma 260, 560, or 760 – is to be used for are welding, then (a) the most suitable dimensions should be chosen according to the dimensions of the welding seam, and (b) the seam should be placed with respect to the manipulator in such a way that as the EE traces that seam with the welding nozzle at a given angle with the seam, the objective function z must remain within a maximum value z_M. This means that the seam should lie as close as possible to the optimum posture of Fig. 10. Furthermore, note that a rotation of the manipulator about the first joint axis, while keeping its other two joints locked, does not perturb z, and hence, a set of optimum postures is available. This set comprises the circle centered at the center of the first joint, of radius d_1 – the distance of the operation point P to the center of the first joint. This circle is similar to the *isotropy circle* of isotropic manipulators [5], and thus, can be termed the *conditioning circle*. Therefore, a good criterion to properly place the seam is that the seam lie as close as possible to the conditioning circle.

Finally, while detecting singularities of nonredundant robots is a rather trivial task, detecting those of their redundant counterparts is more involved, and a fast estimation of the proximity of a given manipulator posture to singularity is always advantageous. This estimation is provided by the objective function z proposed in this paper.

7. Conclusions

The conditioning length $l_{\mathscr{P}}$ was defined for a given posture of a planar manipulator. This concept allows us to normalize the Jacobian matrix so as to render it in nondimensional form. We base the definition of the characteristic length on an objective function z that gives a geometric significance to the conditioning length. Moreover, the objective function introduced here is defined as a measure of the distance of the normalized – nondimensional – Jacobian matrix to an isotropic reference matrix. Isotropic sets of points in the plane are defined as well as operations on these sets. The paper is limited to planar manipulators, with the treatment of spatial manipulators being as yet to be reported.

References

[1] I.B. Vinogradov, A.E. Kobrinski, Y.E. Stepanenko, L.T. Tives, Details of kinematics of manipulators with the method of volumes, Mekh. Mashin (27–28) (1971) 5–16 (in Russian).

[2] A.V. Kumar, K.J. Waldron, The workspace of a mechanical manipulator, ASME J. Mech. Design (1981) 665–672.

[3] T. Yoshikawa, Manipulability of robotic mechanisms, Int. J. Robotics Res. 4 (2) (1985) 3–9.

[4] J. Lee, J. Duffy, K. Hunt, A practical quality index based on the octahedral manipulator, Int. J. Robotic Res. 17 (10) (1998) 1081–1090.

[5] J. Angeles, Fundamentals of Robotic Mechanical Systems, Springer, New York, 1997.

[6] G.H. Golub, C.F. Van Loan, Matrix Computations, The John Hopkins University Press, Baltimore, 1989.

[7] J.K. Salisbury, J.J. Craig, Articulated hands: force control and kinematic issues, Int. J. Robotics Res. 1 (1) (1982) 4–17.

[8] J. Angeles, C.S. López-Cajún, Kinematic isotropy and the conditioning index of serial manipulators, Int. J. Robotics Res. 11 (6) (1992) 560–571.

[9] B. Paden, S. Sastry, Optimal kinematic design of 6R manipulator, Int. J. Robotics Res. 7 (2) (1988) 43–61.

[10] F. Ranjbaran, J. Angeles, M.A. Gonzáles-Palacios, R.V. Patel, The mechanical design of a seven-axes manipulator with kinematic isotropy, J. Intell. Robotic Syst. 14 (1995) 21–41.

[11] O. Bottema, B. Roth, Theorical Kinematics, North-Holland, Amsterdam, 1979.

[12] J. Nielsen, B. Roth, in: Computational Methods in Mechanical Systems, NATO ASI Series F, vol. 161, Springer, Heidelberg, 1998, pp. 233–252.

Architecture Optimization of a 3-DOF Translational Parallel Mechanism for Machining Applications, the Orthoglide

Damien Chablat and Philippe Wenger

Abstract—**This paper addresses the architecture optimization of a three-degree-of-freedom translational parallel mechanism designed for machining applications. The design optimization is conducted on the basis of a prescribed Cartesian workspace with prescribed kinetostatic performances. The resulting machine, the Orthoglide, features three fixed parallel linear joints which are mounted orthogonally, and a mobile platform which moves in the Cartesian x-y-z space with fixed orientation. The interesting features of the Orthoglide are a regular Cartesian workspace shape, uniform performances in all directions, and good compactness. A small-scale prototype of the Orthoglide under development is presented at the end of this paper.**

Index Terms—**Isotropic design, optimal design, parallel mechanism, singularity, workspace.**

I. INTRODUCTION

PARALLEL kinematic machines (PKM) are commonly claimed to offer several advantages over their serial counterparts, like high structural rigidity, high dynamic capacities, and high accuracy [1], [2]. Thus, PKM are interesting alternative designs for high-speed machining applications.

This is why PKM tools attract the interest of more and more researchers and companies. Since the first prototype was presented in 1994 during the IMTS in Chicago, IL, by Gidding and Lewis (the VARIAX), many other prototypes have appeared.

However, the existing PKM suffer from two major drawbacks, namely, a complex workspace and highly nonlinear input/output relations. For most PKM, the Jacobian matrix which relates the joint rates to the output velocities is not constant and not isotropic. Consequently, the performances (e.g., maximum speeds, forces, accuracy, and rigidity) vary considerably for different points in the Cartesian workspace and for different directions at one given point. This is a serious drawback for machining applications [1], [3], [4]. To be of interest for machining applications, a PKM should preserve good workspace properties, that is, regular shape and acceptable kinetostatic performances throughout. In milling applications, the machining conditions must remain constant along the

whole tool path [5]. In many research papers, this criterion is not taken into account in the algorithmic methods used for the optimization of the workspace volume [6], [7].

Most industrial three-axis machine tools have a serial kinematic architecture with orthogonal linear joint axes along the x, y, and z directions. Thus, the motion of the tool in any of these directions is linearly related to the motion of one of the three actuated axes. Also, the performances are constant throughout the Cartesian workspace, which is a parallelepiped. The main drawback is inherent to the serial arrangement of the links, namely, poor dynamic performances. The purpose of this paper is to design a translational three-axis PKM with the advantages of serial machine tools but without their drawbacks. Starting from a Delta-type architecture with three fixed linear joints and three articulated parallelograms, an optimization procedure is conducted in which two criteria are used successively, the conditioning of the Jacobian matrix of the PKM [8]–[11], and the manipulability ellipsoid [12]. The first criterion leads to an isotropic architecture that features a configuration where the tool forces and velocities are equal in all directions. The second criterion makes it possible to define the actuated joint limits and the link lengths with respect to a desired Cartesian workspace size and prescribed limits on the transmission factors. The resulting PKM, the Orthoglide, has a Cartesian workspace shape that is close to a cube whose sides are parallel to the planes xy, yz, and xz, respectively. A systematic design procedure is proposed to define the geometric parameters as a function of the size of a prescribed cubic Cartesian workspace and bounded velocity and force transmission factors throughout.

The next section presents the existing PKM. The design parameters and the kinematics of the mechanism to be optimized are reported in Section III. Section IV is devoted to the design procedure of the Orthoglide and the presentation of the prototype.

II. EXISTING PKM

Most existing PKM can be classified into two main families. The PKM of the first family have fixed foot points and variable-length struts. These PKM are generally called "hexapods" when they have six degrees of freedom (DOFs). Hexapods have a Stewart–Gough parallel kinematic architecture. Many prototypes and commercial hexapod PKM already exist, including the VARIAX (Gidding and Lewis), the CMW300 (Compagnie Mécanique des Vosges), the TORNADO 2000 (Hexel), the MIKROMAT 6X (Mikromat/IWU), the hexapod OKUMA (Okuma), the hexapod G500 (GEODETIC). In this first family,

we find also hybrid architectures with a two-axis wrist mounted in series to a 3-DOF "tripod" positioning structure (e.g., the TRICEPT from Neos-Robotics [13]). Since many machining tasks require only three translational DOFs, several three-axis translational PKM have been proposed. There are several ways to design such mechanisms [20], [14]–[16]. In the first family, we find the Tsai mechanism and its variants. In these mechanisms, the mobile platform is connected to the base by three extensible limbs with a special arrangement of the universal joints that restrains completely the orientation of the mobile platform [18], [19].

The PKM of the second family have fixed length struts with moveable foot points gliding on fixed linear joints. In this category, we find the HEXAGLIDE (ETH Zürich) which features six parallel (also in the geometrical sense) and coplanar linear joints. The HexaM (Toyoda) is another example with three pairs of adjacent linear joints lying on a vertical cone [21]. A hybrid parallel/kinematic PKM with three inclined linear joints and a two-axis wrist is the GEORGE V (IFW Uni Hanover). Many three-axis translational PKMs belong to this second family and use an architecture close to the linear Delta robot originally designed by Reymond Clavel for pick-and-place operations [22]. In this architecture, three parallelograms are used to provide the moving platform with pure translations. The TRIGLIDE (Mikron) has three parallel linear joints in a horizontal plane. The LINAPOD and the INDEX V100 have three vertical (non-coplanar) linear joints [23]. The Urane SX (Renault Automation) and the QUICKSTEP (Krause and Mauser) have three non-coplanar horizontal linear joints [24]. The aforementioned five machines have parallel linear joints. This feature provides these machines with high stiffness in the direction of the linear joints and poor stiffness in the orthogonal directions. Thus, these machines are more suitable for specialized operations like drilling, than for general machining tasks. The STAR mechanism has three horizontal linear joints intersecting at one point [14]. Isotropic conditions for the STAR mechanisms were studied in [25], but a special type of singularity was shown to occur at the isotropic configuration if one prescribes unitary transmission factors [26]. At this singularity (a so-called "RPM-IO-II singularity" in the classification of [27]), there is a loss of both input and output motions and, at the same time, a redundant passive motion of each leg occurs. Recently, one 3-DOF translational mechanism with gliding foot points was found in three separate works to be isotropic throughout the Cartesian workspace [15]–[17]. The mobile platform is connected to three orthogonal linear drives through three identical planar three-revolute jointed serial chains. Full isotropy is clearly an outstanding property. On the other hand, bulky legs are required to assure stiffness because these legs are subject to bending.

PKM with fixed-length struts and moveable foot points are interesting because the actuators are fixed and the moving masses are lower than in the hexapods and tripods.

III. PROBLEM FORMULATION

A. Design Parameters

The machine tool we want to design is a spatial translational PKM dedicated to general three-axis machining tasks with the following requirements:
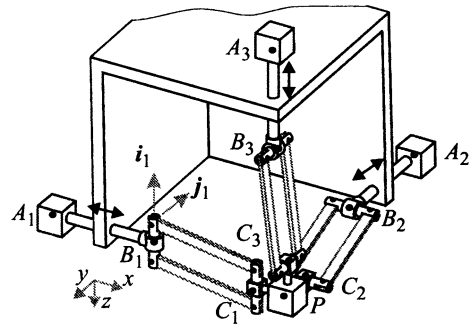

Fig. 1.   Basic kinematic architecture.

1) a configuration should exist where the transmission factors are equal to one in all directions, like in a translational serial machine;
2) the Cartesian workspace shape should be close to a cube of prescribed size with regular performances throughout;
3) the design should be symmetric and use simple joints to lower the manufacturing costs;
4) the PKM should be intrinsically stiff;
5) the PKM should have fixed linear actuated joints to lower the moving masses.

To meet the last requirement, we start with a PKM architecture of the second family, i.e., with fixed linear joints. The use of three articulated parallelograms assembled in an overconstrained way is an interesting solution to comply with requirement 4). Requirements 1) and 2) will be satisfied in Section IV by the isotropic conditions and limited transmission factors constraints. It will be shown that requirement 1) imposes that the three actuated linear joint must be orthogonal, hence the name "orthoglide." To fulfill requirement 3), finally, the three legs should use only revolute joints and be identical.

Fig. 1 shows the basic kinematic architecture of a PKM that complies with requirements 3), 4), and 5), and that we will optimize with respect to requirements 1) and 2). For more simplicity, the figure shows the PKM with the optimized (i.e., orthogonal) linear joints arrangement.

The linear joints can be actuated by means of linear motors or by conventional rotary motors with ball screws. Like the Delta-type PKM, the output body is connected to the linear joints through a set of three parallelograms of equal lengths $L = B_i C_i$, so that it can move only in translation. The three legs are $PRPaR$ identical chains, where P, R, and Pa stands for prismatic, revolute and parallelogram joint, respectively. Thus, the mechanism is overconstrained. The arrangement of the joints in the $PRPaR$ chains have been defined to eliminate any special singularity [26]. Each base point A_i is fixed on the ith linear axis such that $A_1 A_2 = A_1 A_3 = A_2 A_3$. The points B_i and C_i are located on the ith parallelogram, as shown in Fig. 2.

The design parameters to be optimized are the parallelogram length, the position and orientation of each linear actuated joint axis, and the range of the linear actuators.

B. Kinematic Equations and Singular Configurations

Let θ_i and β_i denote the joint angles of the parallelogram about the axes $\mathbf{i}_i$ and $\mathbf{J}_i$, respectively (Fig. 2). Let $\boldsymbol{\rho}_1$, $\boldsymbol{\rho}_2$, and $\boldsymbol{\rho}_3$ denote the linear joint variables, $\boldsymbol{\rho}_i = A_i B_i$.
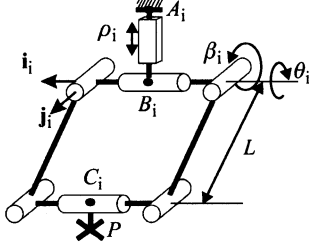
Fig. 2.   Leg kinematics.

Let $\dot{\boldsymbol{\rho}}$ be referred to as the vector of actuated joint rates and $\dot{\mathbf{p}}$ as the velocity vector of point P

$$\dot{\boldsymbol{\rho}} = [\dot{\rho}_1 \ \dot{\rho}_2 \ \dot{\rho}_3]^T, \qquad \dot{\mathbf{p}} = [\dot{x} \ \dot{y} \ \dot{z}]^T.$$

$\dot{\mathbf{p}}$ can be written in three different ways by traversing the three chains $A_i B_i C_i P$

$$\dot{\mathbf{p}} = \mathbf{n}_i \dot{\rho}_i + (\dot{\theta}_i \mathbf{i}_i + \dot{\beta}_i \mathbf{J}_i) \times (\mathbf{c}_i - \mathbf{b}_i) \qquad (1)$$

where $\mathbf{b}_i$ and $\mathbf{c}_i$ are the position vectors, in a given reference frame, of the points B_i and C_i, respectively, and $\mathbf{n}_i$ is the direction vector of the linear joints, for $i = 1, 2, 3$.

We want to eliminate the two passive joint rates $\dot{\theta}_i$ and $\dot{\beta}_i$ from (1), which we do upon dot-multiplying (1) by $\mathbf{c}_i - \mathbf{b}_i$

$$(\mathbf{c}_i - \mathbf{b}_i)^T \dot{\mathbf{p}} = (\mathbf{c}_i - \mathbf{b}_i)^T \mathbf{n}_i \dot{\rho}_i. \qquad (2)$$

Equation (2) can now be cast in vector form, namely

$$\mathbf{A}\dot{\mathbf{p}} = \mathbf{B}\dot{\boldsymbol{\rho}}$$

where $\mathbf{A}$ and $\mathbf{B}$ are the parallel and serial Jacobian matrices, respectively

$$\mathbf{A} = \begin{bmatrix} (\mathbf{c}_1 - \mathbf{b}_1)^T \\ (\mathbf{c}_2 - \mathbf{b}_2)^T \\ (\mathbf{c}_3 - \mathbf{b}_3)^T \end{bmatrix} \qquad (3a)$$

$$\mathbf{B} = \begin{bmatrix} \eta_1 & 0 & 0 \\ 0 & \eta_2 & 0 \\ 0 & 0 & \eta_3 \end{bmatrix} \qquad (3b)$$

with $\eta_i = (\mathbf{c}_i - \mathbf{b}_i)^T \mathbf{n}_i$ for $i = 1, 2, 3$.

The parallel singularities occur when the determinant of the matrix $\mathbf{A}$ vanishes, i.e., when $\det(\mathbf{A}) = 0$. In such configurations, it is possible to move locally the mobile platform, whereas the actuated joints are locked. These singularities are particularly undesirable because the structure cannot resist any force. Equation (3a) shows that the parallel singularities occur when the three vectors $\mathbf{c}_i - \mathbf{b}_i$ are linearly dependent, that is, when the pairs of points (B_i, C_i) lie in parallel planes (Fig. 3). To interpret this singularity, it is more convenient to regard the points C_i as coincident (this does not change the analysis, since each offset $C_i P$ can be included in ρ_i). Then, a parallel singularity occurs when the points B_1, B_2, B_3, and $C = C_1 = C_2 = C_3 = P$ are coplanar. Since, at a parallel singular configuration, P is always equally distant from B_1, B_2, and B_3, P is at the center of a circle of radius L that cuts the x, y, and z axes at B_1, B_2, B_3,
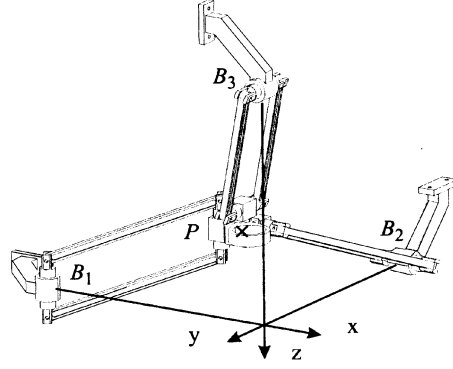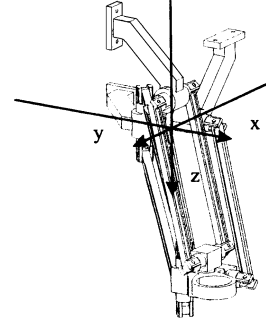

Fig. 3.   Parallel singular configuration in the general case.

Fig. 4.   Parallel singular configuration when $B_i C_i$ are parallel.

respectively, where x, y, and z are parallel to the three linear actuated joints, respectively (Fig. 3). The parallel singularities are defined by the surface generated by P when this circle "glides" along the x, y, and z axes. A particular parallel singularity occurs when the links $B_i C_i$ are parallel. The surface generated is a sphere of radius L and centered at the intersection of the x, y, and z axes (Fig. 4).

Serial singularities arise when the serial Jacobian matrix $\mathbf{B}$ is no longer invertible, i.e., when $\det(\mathbf{B}) = 0$. At a serial singularity, a direction exists along which any Cartesian velocity cannot be produced. Equation (3b) shows that $\det(\mathbf{B}) = 0$ when for one leg i, $(\mathbf{b}_i - \mathbf{A}_i) \perp (\mathbf{c}_i - \mathbf{b}_i)$, where $\mathbf{A}_i$ is the position vector of A_i. Thus, the serial singularities form three planes orthogonal to the x, y, and z axes, respectively.

It will be shown in Section IV-D that the optimization of the Orthoglide puts the serial and parallel singularities far away from the Cartesian workspace. Also, even if the direct and inverse kinematics may, theoretically, have several solutions, only one solution exists in the Cartesian workspace [28].

IV. OPTIMIZATION OF THE DESIGN PARAMETERS

The aim of this section is to define the geometric parameters of the Orthoglide as a function of the size of a prescribed cubic Cartesian workspace with bounded transmission factors. We first show that the orthogonal arrangement of the linear joints is imposed by the condition on the isotropy and manipulability: we want the Orthoglide to have an isotropic configuration with velocity and force transmission factors equal to one. Then, we impose that the transmission factors remain under prescribed bounds throughout the prescribed Cartesian workspace and we deduce the link dimensions and the joint limits. Limiting

the force and velocity transmission factors makes it possible to guarantee a minimal kinematic stiffness throughout the Cartesian workspace. The structural stiffness (i.e., including the stiffness of all rods) is guaranteed by the overconstrained design and preliminary rods stiffness analyses [2]. A more detailed study of the Othoglide structural stiffness is currently conducted at IR-CCyN with finite element analyses.

A. Condition Number and Isotropic Configuration

The Jacobian matrix is said to be isotropic when its condition number attains its minimum value of one [28]. The condition number of the Jacobian matrix is an interesting performance index which characterizes the distortion of a unit ball under the transformation represented by the Jacobian matrix. The Jacobian matrix of a manipulator is used to relate the joint rates and the Cartesian velocities, and the static load on the output link and the joint torques or forces. Thus, the condition number of the Jacobian matrix can be used to measure the uniformity of the distribution of the tool velocities and forces in the Cartesian workspace.

B. Isotropic Configuration of the Orthoglide

For parallel manipulators, it is more convenient to study the conditioning of the Jacobian matrix that is related to the inverse transformation, $\mathbf{J}^{-1}$. When $\mathbf{B}$ is not singular, $\mathbf{J}^{-1}$ is defined by

$$\dot{\boldsymbol{\rho}} = \mathbf{J}^{-1}\dot{\mathbf{p}} \quad \text{with} \quad \mathbf{J}^{-1} = \mathbf{B}^{-1}\mathbf{A}.$$

Thus

$$\mathbf{J}^{-1} = \begin{bmatrix} (1/\eta_1)(\mathbf{c}_1 - \mathbf{b}_1)^T \\ (1/\eta_2)(\mathbf{c}_2 - \mathbf{b}_2)^T \\ (1/\eta_3)(\mathbf{c}_3 - \mathbf{b}_3)^T \end{bmatrix} \quad (4)$$

with $\eta_i = (\mathbf{c}_i - \mathbf{b}_i)^T \mathbf{n}_i$ for $i = 1, 2, 3$.

The matrix $\mathbf{J}^{-1}$ is isotropic when $\mathbf{J}^{-1}\mathbf{J}^{-T} = \sigma^2 \mathbf{1}_{3\times3}$, where $\mathbf{1}_{3\times3}$ is the 3×3 identity matrix. Thus, we must have

$$\frac{1}{\eta_1}\|\mathbf{c}_1 - \mathbf{b}_1\| = \frac{1}{\eta_2}\|\mathbf{c}_2 - \mathbf{b}_2\| = \frac{1}{\eta_3}\|\mathbf{c}_3 - \mathbf{b}_3\| \quad (5a)$$

$$(\mathbf{c}_1 - \mathbf{b}_1)^T(\mathbf{c}_2 - \mathbf{b}_2) = 0 \quad (5b)$$

$$(\mathbf{c}_2 - \mathbf{b}_2)^T(\mathbf{c}_3 - \mathbf{b}_3) = 0 \quad (5c)$$

$$(\mathbf{c}_3 - \mathbf{b}_3)^T(\mathbf{c}_1 - \mathbf{b}_1) = 0. \quad (5d)$$

Equation (5a) states that the angle between the axis of the linear joint and the link B_iC_i must be the same for each leg i. Equations (5b)–(5d) mean that the links B_iC_i must be orthogonal to each other. Fig. 5 shows the isotropic configuration of the Orthoglide. Note that the orthogonal arrangement of the linear joints is not a consequence of the isotropy condition, but it stems from the condition on the transmission factors at the isotropic configuration, as shown in the next section.

C. Transmission Factors

For serial three-axis machine tools, a motion of an actuated joint yields the same motion of the tool (the transmission factors are equal to one). For parallel machines, these motions are
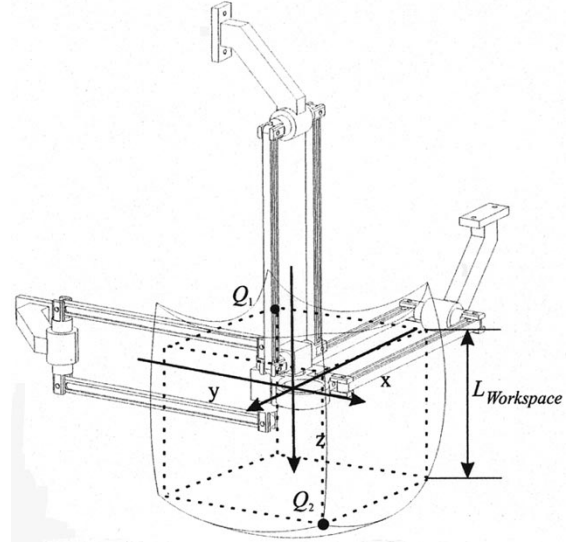

Fig. 5. Isotropic configuration and Cartesian workspace of the Orthoglide mechanism and points Q_1 and Q_2.

generally not equivalent. When the mechanism is close to a parallel singularity, a small joint rate can generate a large velocity of the tool. This means that the positioning accuracy of the tool is lower in some directions for some configurations close to parallel singularities because the encoder resolution is amplified. In addition, a velocity amplification in one direction is equivalent to a loss of stiffness in this direction.

The manipulability ellipsoids of the Jacobian matrix of robotic manipulators was defined two decades ago [9]. This concept has then been applied as a performance index to parallel manipulators [3]. Note that, although the concept of manipulability is close to the concept of condition number, they do not provide the same information. The condition number quantifies the proximity to an isotropic configuration, i.e., where the manipulability ellipsoid is a sphere, or, in other words, where the transmission factors are the same in all the directions, but it does not inform about the value of the transmission factor.

The manipulability ellipsoid of $\mathbf{J}^{-1}$ is used here for defining the orientation of the linear joints and defining the joint limits of the Orthoglide, such that the transmission factors are bounded in the prescribed Cartesian workspace.

We want the transmission factors to be equal to one at the isotropic configuration, as for a serial machine tool. This condition implies that the three terms of (5a) must be equal to one

$$\frac{1}{\eta_1}\|\mathbf{c}_1 - \mathbf{b}_1\| = \frac{1}{\eta_2}\|\mathbf{c}_2 - \mathbf{b}_2\| = \frac{1}{\eta_3}\|\mathbf{c}_3 - \mathbf{b}_3\| = 1 \quad (6)$$

which implies that $(\mathbf{b}_i - \mathbf{a}_i)$ and $(\mathbf{c}_i - \mathbf{b}_i)$ must be collinear for each i.

Since, at this isotropic configuration, links B_iC_i are orthogonal, (6) implies that the links A_iB_i are orthogonal, i.e., the linear joints are orthogonal. For joint rates belonging to a unit ball, namely, $\|\dot{\boldsymbol{\rho}}\| \leq 1$, the Cartesian velocities belong to an ellipsoid such that

$$\dot{\boldsymbol{p}}^T \left(\mathbf{J}\mathbf{J}^T\right) \dot{\boldsymbol{p}} \leq 1.$$

The eigenvectors of matrix $(\mathbf{JJ}^T)^{-1}$ define the direction of its principal axes of this ellipsoid, and the square roots ξ_1, ξ_2, and ξ_3 of the eigenvalues of $(\mathbf{JJ}^T)^{-1}$ are the lengths of the aforementioned principal axes. The velocity transmission factors in the directions of the principal axes are defined by $\psi_1 = 1/\xi_1$, $\psi_2 = 1/\xi_2$, and $\psi_3 = 1/\xi_3$. To limit the variations of this factor, we impose

$$\psi_{\min} \leq \psi_i \leq \psi_{\max} \qquad (7)$$

throughout the Cartesian workspace. This condition determines the link lengths and the linear joint limits. To simplify the problem, we set $\psi_{\min} = 1/\psi_{\max}$.

D. Design of the Orthoglide for a Prescribed Cartesian Workspace

For usual machine tools, the Cartesian workspace is generally given as a function of the size of a right-angled parallelepiped. Due to the symmetrical architecture of the Orthoglide, the Cartesian workspace has a fairly regular shape. In fact, the workspace is defined by the intersection of three orthogonal cylinders topped with spheres. As shown in Fig. 5, it is easy to include a cube whose sides are parallel to the planes xy, yz, and xz, respectively. The aim of this section is to define the position of the base point A_i, the link lengths L, and the linear actuator range $\Delta\rho$ with respect to the limits on the transmission factors defined in (7) and as a function of the size of the prescribed Cartesian workspace $L_{\text{Workspace}}$.

The proposed optimization scheme is divided into three steps.

1) First, two points Q_1 and Q_2 are determined in the prescribed cubic Cartesian workspace (Fig. 5) such that if the transmission factor bounds are satisfied at these points, they are satisfied in all the prescribed Cartesian workspace.

2) The points Q_1 and Q_2 are used to define the leg length L as function of the size of the prescribed cubic Cartesian workspace.

3) Finally, the positions of the base points A_i and the linear actuator range $\Delta\rho$ are calculated such that the prescribed cubic Cartesian workspace is fully included in the Cartesian workspace of the Orthoglide.

Step 1: The transmission factors are equal to one at the isotropic configuration. These factors increase or decrease when the tool center point moves away from the isotropic configuration and they tend toward zero or infinity in the vicinity of the singularity surfaces. It turns out that the points Q_1 and Q_2 defined at the intersection of the Cartesian workspace boundary with the axis $x = y = z$ (in a reference frame [O, x, y, z] centered at the intersection of the three linear joint axes, Fig. 5) are the closest ones to the singularity surfaces, as illustrated in Fig. 6, which shows on the same top view the Orthoglide in the two parallel singular configurations of Figs. 3 and 4. Thus, we may postulate the intuitive result that if the prescribed bounds on the transmission factors are satisfied at Q_1 and Q_2, then these bounds are satisfied throughout the prescribed cubic Cartesian workspace. In fact, this result can be proved using interval analysis [29].
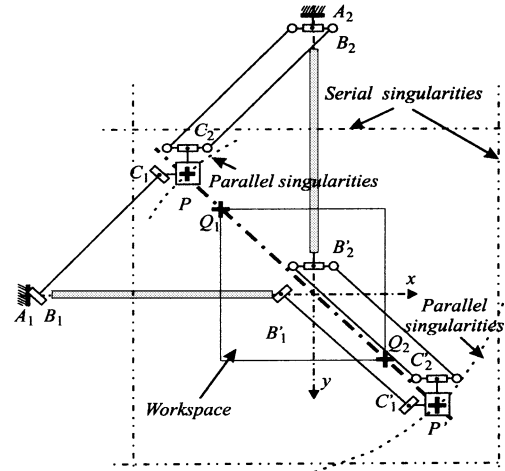

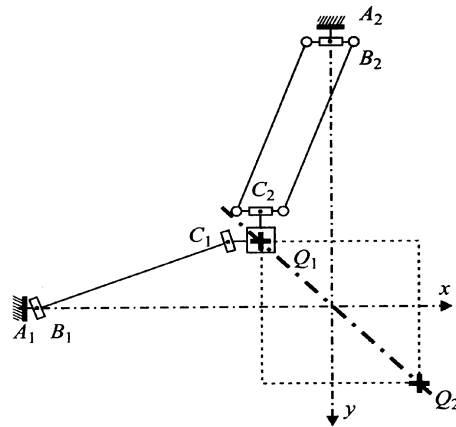Fig. 6. Points Q_1 and Q_2 and the singular configurations (top view).

Fig. 7. Q_1 configuration.

Step 2: At the isotropic configuration, the angles θ_i and β_i are equal to zero by definition. When the tool center point P is at Q_1, $\rho_1 = \rho_2 = \rho_3 = \rho_{\min}$ (Fig. 7). When P is at Q_2, $\rho_1 = \rho_2 = \rho_3 = \rho_{\max}$ (Fig. 8).

We pose $\rho_{\min} = 0$ for more simplicity.

The position of P along the z axis can be written equivalently as $z = -\sin(\beta_1)L$ and $z = \sin(\theta_2)\cos(\beta_2)L$ by traversing the two chains $A_1B_1C_2P$ and $A_2B_2C_2P$, respectively. On the axis (Q_1Q_2), $\beta_1 = \beta_2 = \beta_3$ and $\theta_1 = \theta_2 = \theta_3$. We note

$$\beta_1 = \beta_2 = \beta_3 = \beta \quad \text{and} \quad \theta_1 = \theta_2 = \theta_3 = \theta. \qquad (8)$$

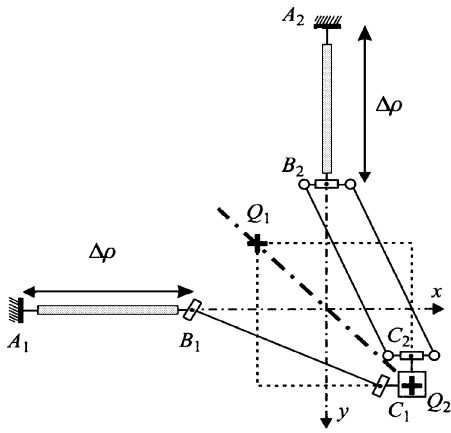Thus, the angle β can be written as a function of θ

$$\beta = -\arctan(\sin(\theta)). \qquad (9)$$

Finally, by substituting (9) into (4), the inverse Jacobian matrix $\mathbf{J}^{-1}$ can be simplified as follows:

$$\mathbf{J}^{-1} = \begin{bmatrix} 1 & -\tan(\theta) & -\tan(\theta) \\ -\tan(\theta) & 1 & -\tan(\theta) \\ -\tan(\theta) & -\tan(\theta) & 1 \end{bmatrix}.$$

Thus, the square roots of the eigenvalues of $(\mathbf{JJ}^T)^{-1}$ are

$$\xi_1 = |2\tan(\theta) - 1| \quad \text{and} \quad \xi_2 = \xi_3 = |\tan(\theta) + 1|.$$

Fig. 8. Q_2 configuration.

And the three velocity transmission factors are

$$\psi_1 = \frac{1}{|2\tan(\theta) - 1|} \quad \text{and} \quad \psi_2 = \psi_3 = \frac{1}{|\tan(\theta) + 1|}. \tag{10}$$

The joint limits on θ are located on both sides of the isotropic configuration. To calculate the joint limits, we solve the following inequations:

$$\frac{1}{\psi_{max}} \leq \frac{1}{|2\tan(\theta) - 1|} \leq \psi_{\max} \tag{11a}$$

$$\frac{1}{\psi_{max}} \leq \frac{1}{|\tan(\theta) + 1|} \leq \psi_{\max} \tag{11b}$$

where the value of $\psi_{\max}$ depends on the performance requirements. Two sets of joint limits ($[\theta_{Q_1}\beta_{Q_1}]$ and $[\theta_{Q_2}\beta_{Q_2}]$) are found in symbolic form. The detail of this calculation is given in the Appendix.

The position vectors $\mathbf{q}_1$ and $\mathbf{q}_2$ of the points Q_1 and Q_2, respectively, can be easily defined as a function of L (Figs. 7 and 8)

$$\mathbf{q}_1 = [q_1 \ q_1 \ q_1]^T \quad \text{and} \quad \mathbf{q}_2 = [q_2 \ q_2 \ q_2]^T \tag{12a}$$

with

$$q_1 = -\sin(\beta_{Q_1})L \quad \text{and} \quad q_2 = -\sin(\beta_{Q_2})L. \tag{12b}$$

The size of the Cartesian workspace is

$$L_{\text{Workspace}} = |q_2 - q_1|. $$

Thus, L can be defined as a function of $L_{\text{Workspace}}$

$$L = \frac{L_{\text{Workspace}}}{|\sin(\beta_{Q_2}) - \sin(\beta_{Q_1})|}.$$

Step 3: We want to determine the positions of the base points, namely, $a = OA_1 = OA_2 = OA_3$. When the tool center point P is at Q_1' defined as the projection onto the y axis of Q_1, $\rho_2 = 0$ and (Fig. 9)
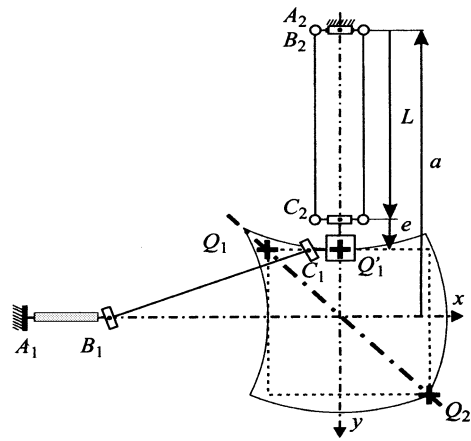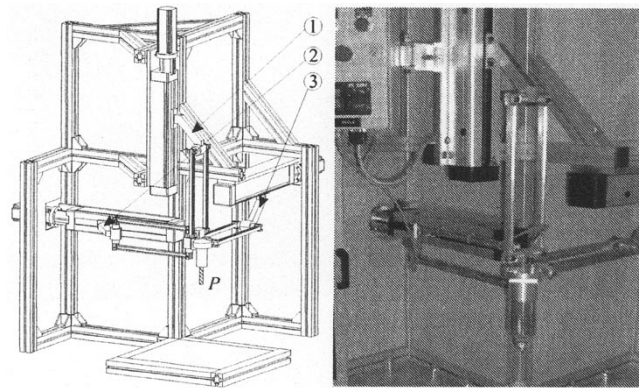
$$OA_2 = OQ_1' + Q_1'C_2 + C_2A_2.$$

Fig. 9.   Point Q_1' used for the determination of a.

Fig. 10.   Catia model of the Orthoglide (left) and prototype (right).

Since $\rho_2 = 0$, $C_2A_2 = C_2B_2 = L$. With $OA_2 = a$, $Q_1'C_2 = PC_2 = -e$, and $OQ_1' = q_1$, we get

$$a = q_1 - e - L.$$

Since q_1 is known from (12a) and (17b), a can be calculated as function of e, L, and $\psi_{\max}$.

Now, we have to calculate the linear joint range $\Delta\rho = \rho_{\max}$ (we have posed $\rho_{\min} = 0$).

When the tool center point P is at Q_2, $\rho = \rho_{\max}$. Projecting $A_2P = A_2B_2 + B_2C_2 + C_2P$ on the y axis yields

$$\rho_{\max} = q_2 - a - \cos(\theta_{Q_2})\cos(\beta_{Q_2})L - e.$$

E. Prototype

Using the aforementioned two kinetostatic criteria, a small-scale prototype has been constructed in our laboratory (Fig. 10). The three parts (1), (2), and (3) have been designed to prevent each parallelogram from colliding with the corresponding linear motion guide. Also, the shifted position of the tool center point P limits the collisions between the parallelograms and the workpiece. The actuated joints used for this prototype are rotary motors with ball screws. The prescribed performances of the Orthoglide prototype are a Cartesian velocity of 1.2 m/s and an acceleration of 14 m/s^2 at the isotropic point. The desired payload is 4 kg. The size of its
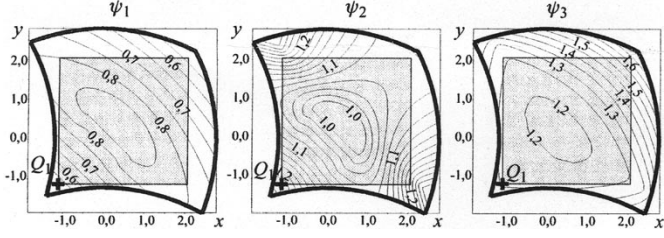
Fig. 11. Three velocity transmission factors in a z cross section of the Cartesian workspace passing through Q_1.

prescribed cubic Cartesian workspace is $200 \times 200 \times 200$ mm. We limit the variations of the velocity transmission factors as

$$1/2 \leq \psi_i \leq 2. \tag{13}$$

The resulting length of the three parallelograms is $L = 310$ mm and the resulting range of the linear joints is $\Delta\rho = 257$ mm. Thus, the ratio of the range of the actuated joints to the size of the prescribed Cartesian workspace is $r = 200/257 = 0.78$. This ratio is high compared to other PKM. The three velocity transmission factors are depicted in Fig. 11. These factors are given in a z cross section of the Cartesian workspace passing through Q_1.

V. Conclusions

The Orthoglide is a new Delta-type PKM dedicated to three-axis rapid machining applications that was designed to meet the advantages of both serial three-axis machines (regular workspace and homogeneous performances) and parallel kinematic architectures (good dynamic performances). A systematic procedure has been provided to define the geometric parameters of the Orthoglide as functions of the size of a prescribed cubic Cartesian workspace and bounded velocity and force transmission factors.

The Orthoglide has been designed under isotropic conditions and limited transmission factors. Low inertia and intrinsic stiffness have been set as additional design requirements. Thus, three articulated parallelograms have been used, rather than legs subject to bending as in the fully isotropic mechanisms proposed in [15]–[17]. At the isotropic configuration, a displacement of a linear joint yields the same displacement of the tool in the corresponding Cartesian direction, as in a serial machine. The Cartesian workspace is simple, regular, and free of singularities and self collisions. It is fairly regular and the performances are homogeneous throughout the Cartesian workspace. Thus, the entire Cartesian workspace is really available for tool paths. These features make the Orthoglide a novel design, compared with the existing Delta-type PKM structures. A small-scale prototype Orthoglide has been built at IRCCyN to demonstrate the feasibility of the design. Dynamic model-based control laws will be implemented [30] and first machining experiments with plastic parts will be conducted.

Appendix

To calculate the joint limits on θ and β, we solve the followings inequations, from (11)

$$|2\tan(\theta) - 1| \leq \psi_{\max} \quad \frac{1}{|2\tan(\theta) - 1|} \leq \psi_{\max}. \tag{14}$$

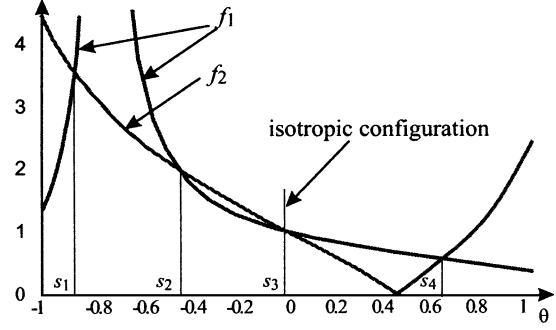
Fig. 12. f_1 and f_2 as functions of θ along $(Q_1 Q_2)$.

Thus, we note

$$f_1 = |2\tan(\theta) - 1| \quad f_2 = 1/|2\tan(\theta) - 1|. \tag{15}$$

Fig. 12 shows f_1 and f_2 as functions of θ along $(Q_1 Q_2)$. The four roots of $f_1 = f_2$ in $[-\pi \ \pi]$ are

$$s_1 = -\arctan\left(\left(1 + \sqrt{17}\right) \big/ 4\right) \tag{16a}$$

$$s_2 = -\arctan(1/2) \tag{16b}$$

$$s_3 = 0 \tag{16c}$$

$$s_4 = \arctan\left(\left(-1 + \sqrt{17}\right) \big/ 4\right) \tag{16d}$$

with

$$f_1(s_1) = \left(-3 + \sqrt{17}\right) \big/ 4 \quad f_1(s_2) = 2 \tag{16e}$$

$$f_1(s_3) = 1 \quad f_1(s_4) = \left(3 + \sqrt{17}\right) \big/ 4. \tag{16f}$$

The isotropic configuration is located at the configuration where $\theta = \beta = 0$. The limits on θ and β are in the vicinity of this configuration. Along the axis $(Q_1 Q_2)$, the angle θ is lower than 0 when it is close to Q_2, and greater than 0 when it is close to Q_1.

To find θ_{Q_1}, we study the functions f_1 and f_2, which are both decreasing on $[0 \ \arctan(1/2)]$. Thus, we have

$$\theta_{Q_1} = \arctan\left(\frac{\psi_{\max} - 1}{2\psi_{\max}}\right) \tag{17a}$$

$$\beta_{Q_1} = -\arctan\left(\frac{\psi_{\max} - 1}{\sqrt{5\psi_{\max}^2 - 2\psi_{\max} + 1}}\right). \tag{17b}$$

In the same way, to find θ_{Q_2}, we study the functions f_1 and f_2 on $[s_1 \ 0]$. The three roots s_1, s_2, and s_3 define two intervals. If $\psi_{\max} \in [f_1(s_1) \ f_1(s_2)]$, we have

$$\theta_{Q_2} = -\arctan\left(\frac{\psi_{\max} - 1}{\psi_{\max}}\right) \tag{18a}$$

$$\beta_{Q_2} = \arctan\left(\frac{\psi_{\max} - 1}{\sqrt{2\psi_{\max}^2 - 2\psi_{\max} + 1}}\right) \tag{18b}$$

otherwise, if $\psi_{\max} \in [f_1(s_2) f_1(s_3)]$

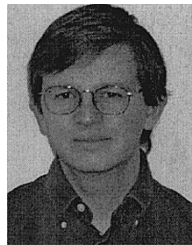$$\theta_{Q_2} = -\arctan\left(\frac{\psi_{\max} - 1}{2}\right) \tag{18c}$$

$$\beta_{Q_2} = \arctan\left(\frac{\psi_{\max} - 1}{\sqrt{\psi_{\max}^2 - 2\psi_{\max} + 5}}\right). \tag{18d}$$

REFERENCES

[1] J. Tlusty, J. Ziegert, and S. Ridgeway, "Fundamental comparison of the use of serial and parallel kinematics for machine tools," *Ann. CIRP*, vol. 48, no. 1, pp. 351–356, 1999.

[2] P. Wenger, C. Gosselin, and B. Maille, "A comparative study of serial and parallel mechanism topologies for machine tools," in *Proc. PKM'99*, Milan, Italy, 1999, pp. 23–32.

[3] J. Kim, C. Park, J. Kim, and F. C. Park, "Performance analysis of parallel manipulator architectures for CNC machining applications," in *Proc. IMECE Symp. Machine Tools*, Dallas, TX, 1997.

[4] P. Wenger, C. Gosselin, and D. Chablat, "A comparative study of parallel kinematic architectures for machining applications," in *Proc. Workshop Computational Kinematics*, Seoul, Korea, 2001, pp. 249–258.

[5] F. Rehsteiner, R. Neugebauer, S. Spiewak, and F. Wieland, "Putting parallel kinematics machines (PKM) to productive work," *Ann. CIRP*, vol. 48, no. 1, pp. 345–350, 1999.

[6] C.-M. Luh, F. A. Adkins, E. J. Haug, and C. C. Qui, "Working capability analysis of Stewart platforms," *Trans. ASME*, pp. 220–227, 1996.

[7] J.-P. Merlet, "Determination of 6D workspace of Gough-type parallel manipulator and comparison between different geometries," *Int. J. Robot. Res.*, vol. 19, no. 9, pp. 902–916, 1999.

[8] G. H. Golub and C. F. Van Loan, *Matrix Computations*. Baltimore, MD: Johns Hopkins Univ. Press, 1989.

[9] J.-K. Salisbury and J.-J. Craig, "Articulated hands: Force control and kinematic issues," *Int. J. Robot. Res.*, vol. 1, no. 1, pp. 4–17, 1982.

[10] T. Huang and D. Whitehouse, "Local dexterity, optimal architecture and optimal design of parallel machine tools," *Ann. CIRP*, vol. 47, no. 1, pp. 347–351, 1998.

[11] K. E. Zanganeh and J. Angeles, "Kinematic isotropy and the optimum design of parallel manipulators," *Int. J. Robot. Res.*, vol. 16, no. 2, pp. 185–197, 1997.

[12] T. Yoshikawa, "Manipulability of robot mechanisms," *Int. J. Robot. Res.*, vol. 4, no. 2, pp. 3–9, 1985.

[13] K. E. Neumann, "Robot," U. S. Patent 4 732 525, Mar. 22, 1988.

[14] J. M. Hervé and F. Sparacino, "Structural synthesis of parallel robots generating spatial translation," in *Proc. 5th Int. Conf. Advanced Robotics*, vol. 1, 1991, pp. 808–813.

[15] M. Carricato and V. Parenti-Castelli, "Singularity-free fully isotropic translational parallel manipulators," *Int. J. Robot. Res.*, vol. 21, no. 2, pp. 161–174, 2002.

[16] X. Kong and C. M. Gosselin, "Type synthesis of linear translational parallel manipulators," in *Advances in Robot Kinematic*, J. Lenarčič and F. Thomas, Eds. Norwell, MA: Kluwer, 2002, pp. 453–462.

[17] H. S. Kim and L. W. Tsai, "Evaluation of a Cartesian manipulator," in *Advances in Robot Kinematic*, J. Lenarčič and F. Thomas, Eds. Norwell, MA: Kluwer, 2002, pp. 21–38.

[18] L. W. Tsai and S. Joshi, "Kinematics and optimization of a spatial 3-UPU parallel manipulator," *ASME J. Mech. Des.*, vol. 122, pp. 439–446, 2000.

[19] R. Di Gregorio and V. Parenti-Castelli, "A translational 3-DOF parallel manipulator," in *Advances in Robot Kinematic*, J. Lenarčič and M. Husty, Eds. Norwell, MA: Kluwer, 1998, pp. 49–58.

[20] C. Reboulet and C. Lambert, "Dispositif manipulateur pour déplacer un objet dans l'espace parallèlement à lui-même," French Patent 90.15.846, Dec. 18, 1990.

[21] T. Toyama *et al.*, "Machine tool having parallel structure," U. S. Patent 5 715 729, Feb. 10, 1998.

[22] R. Clavel, "DELTA, a fast robot with parallel geometry," in *Proc. 18th Int. Symp. Robotic Manipulators*, 1988, pp. 91–100.

[23] G. Pritschow and K. H. Wurst, "Systematic design of hexapods and other parallel link systems," *Ann. CIRP*, vol. 46, no. 1, pp. 541–548, 1997.

[24] O. Company, F. Pierrot, F. Launay, and C. Fioroni, "Modeling and preliminary design issues of a 3-axis parallel machine tool," in *Proc. Int. Conf. PKM 2000*, Ann Arbor, MI, 2000, pp. 14–23.

[25] L. Baron and G. Bernier, "The design of parallel manipulators of star topology under isotropic constraint," in *Proc. DETC ASME*, Pittsburgh, PA, 2001, [CD-ROM].

[26] F. Majou, P. Wenger, and D. Chablat, "Design of a 3-axis parallel machine tool for high speed machining: The orthoglide," in *Proc. 4th Int. Conf. Integrated Design and Manufacturing in Mechanical Engineering*, Clermont-Ferrand, France, 2002, [CD-ROM].

[27] D. Zlatanov, G. Fenton, and B. Benhabib, "Singularity analysis of mechanism and robots via a velocity equation model of the instantaneous kinematics," in *Proc. IEEE Int. Conf. Robotics and Automation*, San Diego, CA, 1994, pp. 986–991.

[28] P. Wenger and D. Chablat, "Kinematic analysis of a new parallel machine tool: The orthoglide," in *Advances in Robot Kinematic*, J. Lenarčič and M. M. Stanišić, Eds. Norwell, MA: Kluwer, 2000, pp. 305–314.

[29] D. Chablat, P. Wenger, and J. P. Merlet, "Workspace analysis of the orthoglide using interval analysis," in *Advances in Robot Kinematic*, J. Lenarčič and F. Thomas, Eds. Norwell, MA: Kluwer, 2002, pp. 397–406.

[30] S. Guegan and W. Khalil, "Dynamic modeling of the orthoglide," in *Advances in Robot Kinematic*, J. Lenarčič and F. Thomas, Eds. Norwell, MA: Kluwer, 2002, pp. 387–396.

Damien Chablat received the Ph.D. degree in Génie Mécanique from the École Centrale de Nantes and University of Nantes, Nantes, France in 1998.

For one year, he was with the Centre of Intelligent Machines, McGill University, Montreal, QC, Canada. He joined the Centre National de la Recherche Scientifique (CNRS), Paris, France, in 1999 and is now with the Institut de Recherche en Communications et Cybernétique de Nantes, Nantes, France. His research interests include robotics, design of parallel manipulators, and virtual reality in design products.

Philippe Wenger received the Eng. Degree in mechanical engineering from École Centrale de Nantes, Nantes, France, in 1985, and the Ph.D. degree in robotics from University of Nantes, Nantes, France, in 1989.

Since 1990, he has been a Centre National de la Recherche Scientifique (CNRS) researcher at Institut de Recherche en Communications et Cybernétique de Nantes, Nantes, France, and a Professor of Robotics at École Centale de Nantes and École Supérieure d'Électricité, Rennes, France. He is responsible for the research group "Méthode de Conception en Mécanique" (Design Methods for Mechanical Engineering). His research interests include design and analysis of parallel mechanisms, robotics-CAD, and manipulator kinematics.

ELSEVIER

Design strategies for the geometric synthesis of Orthoglide-type mechanisms

A. Pashkevich [a,1], P. Wenger [b], D. Chablat [b,*]

[a] *Belarusian State University of Informatics and Radioelectronics, P. Brovka str, 220027 Minsk, Republic of Belarus*
[b] *Institut de Recherche en Communications et Cybernétique de Nantes [2], 1, rue de la Noë B.P. 6597,*
44321 Nantes Cedex 3, France

Abstract

The paper addresses the geometric synthesis of Orthoglide-type mechanism, a family of 3-DOF parallel manipulators for rapid machining applications, which combine advantages of both serial mechanisms and parallel kinematic architectures. These manipulator possess quasi-isotropic kinematic performances and are made up of three actuated fixed prismatic joints, which are mutually orthogonal and connected to a mobile platform via three parallelogram chains. The platform moves in the Cartesian space with fixed orientation, similar to conventional XYZ-machine. Three strategies have been proposed to define the Orthoglide geometric parameters (manipulator link lengths and actuated joint limits) as functions of a cubic workspace size and dextrous properties expressed by bounds on the velocity transmission factors, manipulability or the Jacobian condition number. Low inertia and intrinsic stiffness have been set as additional design goals expressed by the minimal link length requirement. For each design strategy, analytical expressions for computing the Orthoglide parameters are proposed. It is showed that the proposed strategies yield Pareto-optimal solutions, which differ by the kinematic performances outside the prescribed Cartesian cube (but within the workspace bounded by the actuated

---

* Corresponding author. Tel.: +33 2 40 37 69 54; fax: +33 2 40 37 69 30.
  E-mail addresses: pap@bsuir.unibel.by (A. Pashkevich), philippe.wenger@irccyn.ec-nantes.fr (P. Wenger), damien.chablat@irccyn.ec-nantes.fr (D. Chablat).
[1] Tel.: +375 17 239 86 73; fax: +375 17 231 09 14.
[2] IRCCyN: UMR no 6597 CNRS, École Centrale de Nantes, Université de Nantes, École des Mines de Nantes.

joint limits). The proposed technique is illustrated with numerical examples for the Orthoglide prototype design.

1. Introduction

Parallel kinematic machines (PKM) are commonly claimed to offer several advantages over their serial counterparts, such as high structural rigidity, better payload-to-weight ratio, high dynamic capacities and high accuracy [1–3]. Thus, they are prudently considered as promising alternatives for high-speed machining and have gained essential attention of a number of companies and researchers. Since the first prototype presented in 1994 during the IMTS in Chicago by Gidding and Lewis (the VARIAX), many other parallel manipulators have appeared. However, most of the existing PKM still suffer from two major drawbacks, namely, a complex workspace and highly non-linear input/output relations [4,5].

For most PKM, the Jacobian matrix, which relates the joint rates to the output velocities, is not isotropic. Consequently, the performances (e.g. maximum speeds, forces, accuracy and rigidity) vary considerably for different points in the Cartesian workspace and for different directions at one given point. This is a serious disadvantage for machining applications [6,7], which require regular workspace shape and acceptable kinetostatic performances throughout. In milling applications, for instance, the machining conditions must remain constant along the whole tool path [8]. Nevertheless, in many research papers, this criterion is not taken into account in the algorithmic methods used for the optimization of the workspace volume [9,10].

In contrast, for the conventional XYZ-machines, the tool motion in any direction is linearly related to the motions of the actuated axes. Also, the performances are constant throughout the Cartesian parallelepiped workspace. The only drawback is inherent to the serial arrangement of the links, which causes poor dynamic performances. So, in recent years, several new parallel kinematic structures have been proposed. In particular, a 3-dof translational mechanism with gliding foot points was found in three separate works to be fully isotropic throughout the Cartesian workspace [11–13]. Although this manipulator behaves like the conventional Cartesian mechanism, its legs are rather bulky to assure stiffness. The latter motivates further research in PKM architecture that seeks for compromise solutions, which admit a partial isotropy in favour of other manipulator features.

One of such compromise solutions is the Orthoglide proposed by Wenger and Chablat [14], which was derived from a Delta-type architecture with three fixed linear joints and three articulated parallelograms. As follows from the previous works, this manipulator possesses good (almost isotropic) kinetostatic performances and also has some technological advantages, such as (i) symmetrical design; (ii) quasi-isotropic workspace; and (iii) low inertia effects [15]. In a previous work, the Orthoglide was optimised with respect to the Jacobian matrix conditioning and transmission factor limits throughout a prescribed Cartesian workspace [16].

This paper further contributes to the Orthoglide kinematic synthesis and focuses on the comparison of different design strategies and inherited criteria. It proposes a systematic design procedure to define the manipulator geometric parameters (the actuated joint limits and the link

lengths) as function of the prescribed cubic workspace size and performances measure bounds. The reminder of the paper is organized as follows. Section 2 briefly describes the Orthoglide kinematics and defines the design goals. Section 3 investigates the manipulator performances through the workspace. Section 4 deals with the design of the dextrous workspace with bounded manipulability, condition number and velocity transmission factors. Section 5 focuses on defining the largest cube inscribed in the dextrous workspace. Section 6 illustrates the proposed design strategies by numerical examples and also contains some discussions. And, finally, Section 7 summarises the main contributions of the paper.

2. Orthoglide kinematics and design goals

2.1. Manipulator geometry

The kinematic architecture of the Orthoglide is shown in Fig. 1. It consists of three identical parallel chains that may be formally described as PRP_aR, where P, R and P_a denote the prismatic, revolute, and parallelogram joints, respectively. The mechanism input is made up of three actuated orthogonal prismatic joints. The output machinery (with a tool mounting flange) is connected to the prismatic joints through a set of three parallelograms, so that it is restricted for translational movements only.

Because of its symmetrical structure, the Orthoglide can be presented in a simplified model, which consists of three bar links connected by spherical joints to the tool centre point at one side and to the corresponding prismatic joints at another side (Fig. 2a).

Thus, if the origin of a reference frame is located at the intersection of the prismatic joint axes and the x, y, z-axes are directed along them, the manipulator geometry may be described by the equations

$$(p_x - \rho_x)^2 + p_y^2 + p_z^2 = L^2, \quad p_x^2 + (p_y - \rho_y)^2 + p_z^2 = L^2, \quad p_x^2 + p_y^2 + (p_z - \rho_z)^2 = L^2, \tag{1}$$

where $\mathbf{p} = (p_x, p_y, p_z)$ is the output position vector, $\rho = (\rho_x, \rho_y, \rho_z)$ is the input vector of the prismatic joints variables, and L is the length of the parallelogram principal links. It should be noted
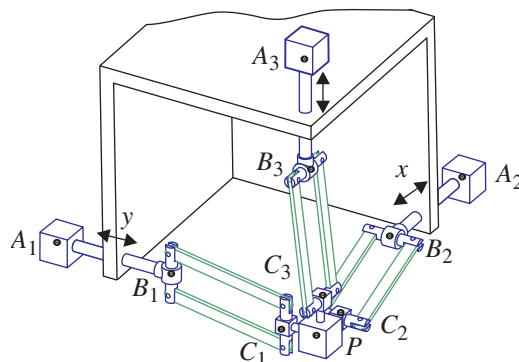

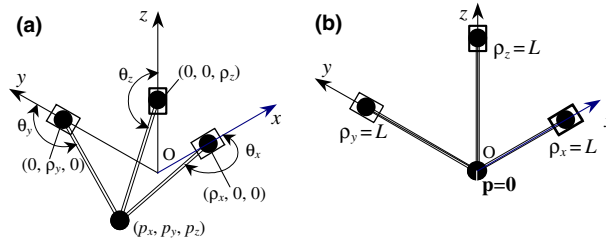Fig. 1. Kinematic architecture of the Orthoglide.

Fig. 2. Orthoglide simplified model (a) and its "zero" configuration (b).

that, for this convention, the "zero" position $\mathbf{p}_0 = (0,0,0)$ corresponds to the joints variables $\rho_0 = (L,L,L)$, see Fig. 2b.

It is also worth mentioning that the Orthoglide geometry and relevant manufacturing technology impose the following constraints on the joint variables:

$$0 < \rho_x \leqslant 2L, \quad 0 < \rho_y \leqslant 2L, \quad 0 < \rho_z \leqslant 2L, \tag{2}$$

which essentially influence on the workspace shape. While the upper bound is implicit and obvious, the lower one is caused by practical reasons, since safe mechanical design encourages avoiding risk of simultaneous location of prismatic joints in the same point of the Cartesian workspace. Hence the kinematic synthesis must produce required joint limits within (2).

2.2. Inverse kinematics

From Eq. (1), the inverse kinematic relations can be derived in a straightforward way

$$\rho_x = p_x + s_x\sqrt{L^2 - p_y^2 - p_z^2}, \quad \rho_y = p_y + s_y\sqrt{L^2 - p_x^2 - p_z^2}, \quad \rho_z = p_z + s_z\sqrt{L^2 - p_x^2 - p_y^2}, \tag{3}$$

where $s_x, s_y, s_z \in \{\pm 1\}$ are the configuration indices defined as signs of $\rho_x - p_x$, $\rho_y - p_y$, $\rho_z - p_z$, respectively. Their geometrical meaning is illustrated by Fig. 2a, where θ_x, θ_y, θ_z are the angles between the bar links and corresponding prismatic joint axes. It can be easily proved that $s = +1$ if $\theta_a \in (90°, 180°)$ and $s = -1$ if $\theta_a \in (0°, 90°)$, where the subscript a belongs to the set $a \in \{x,y,z\}$. It should be also stressed that the border ($\theta = 90°$) corresponds to the serial singularity (when the link is orthogonal to the relevant translational axis and the input joint motion does not produce the end-point displacement), so corresponding Cartesian points must be excluded from the Orthoglide workspace during the design.

It is obvious that expressions (3) define eight different solutions to the inverse kinematics and their existence requires the workspace points to belong to a volume bounded by the intersection of three cylinders $C_L = \{\mathbf{p} \mid p_x^2 + p_y^2 \leqslant L^2; p_x^2 + p_z^2 \leqslant L^2; p_y^2 + p_z^2 \leqslant L^2\}$. However, the joint limits (2) impose additional constraints, which reduce a potential solution set. For example, for the "zero" location $\mathbf{p}_0 = (0,0,0)$, Eq. (3) give eight solutions $\rho = (\pm L, \pm L, \pm L)$ but only one of them is feasible. As proved in [17], with respect to number of inverse kinematic solutions, the Orthoglide with joint limits (2) admits only 2 alternatives: (i) a single inverse kinematic solution ($s_x, s_y, s_z = +1$) inside the sphere $S_L = \{\mathbf{p} \in C_L \mid p_x^2 + p_y^2 + p_z^2 < L^2\}$; and (ii) eight inverse kinematic solutions ($s_x, s_y, s_z \in \{\pm 1\}$) inside $G_L = \{\mathbf{p} \in C_L \mid p_x, p_y, p_z > 0; p_x^2 + p_y^2 + p_z^2 > L^2\}$. It can be also proved that

the border between these two cases corresponds to the serial singularity. Hence, the kinematic synthesis must focus on the location of the workspace inside of the sphere S_L.

2.3. Direct kinematics

After subtracting three possible pairs of the equation (1) and analysis of the differences, the Cartesian coordinates p_x, p_y, p_z can be expressed as

$$p_x = \frac{\rho_x}{2} + \frac{t}{\rho_x}, \quad p_y = \frac{\rho_y}{2} + \frac{t}{\rho_y}, \quad p_z = \frac{\rho_z}{2} + \frac{t}{\rho_z}, \tag{4}$$

where t is an auxiliary scalar variable. This reduces the direct kinematics to the solution of a quadratic equation, $At^2 + Bt + C = 0$ with coefficients $A = (\rho_x\rho_y)^2 + (\rho_x\rho_z)^2 + (\rho_y\rho_z)^2$; $B = (\rho_x\rho_y\rho_z)^2$; $C = (\rho_x^2 + \rho_y^2 + \rho_z^2 - 4L^2)(\rho_x\rho_y\rho_z)^2/4$. The quadratic formula yields two solutions $t = (-B + m\sqrt{B^2 - 4AC})/(2A)$ that differ by the configuration index $m = \pm 1$, which, from a geometrical point of view, distinguishes two possible locations of the target point with respect to the plane passing through the prismatic joint centres. Algebraically, this index can be defined as $m = \mathrm{sgn}(p_x\rho_x^{-1} + p_y\rho_y^{-1} + p_z\rho_z^{-1} - 1)$. It should be stressed that the case $B^2 = 4AC$ corresponds to a parallel singularity, so corresponding joint coordinates must be excluded during the design.

It is obvious that the direct kinematic solution exists if and only if $B^2 \geqslant 4AC$, which defines a closed region in the joint variable space $\mathfrak{R}_L = \{\rho \mid (\rho_x^2 + \rho_y^2 + \rho_z^2 - 4L^2)(\rho_x^{-2} + \rho_y^{-2} + \rho_z^{-2})1\}$. Taking into account (2), the feasible joint space may be presented as $\mathfrak{R}_L^+ = \{\rho \in \mathfrak{R}_L \mid \rho_x, \rho_y, \rho_z \geqslant 0\}$. Hence, with respect to the number of direct kinematic solutions, the Orthoglide with joint limits (2) admits 2 alternatives [17]: (i) two direct kinematic solutions ($m = \pm 1$) inside the region $\mathfrak{R}_L^+$; and (ii) a single direct kinematic solution on the positive border of the region $\mathfrak{R}_L^+$. Since the second case corresponds to the singularity, the kinematic synthesis must focus on using the inner part of $\mathfrak{R}_L^+$.

2.4. Design goals and parameters

Because the Orthoglide is dedicated to general 3-axis machining, its kinematic performances should be close to the performances of the classical XYZ-machine. Therefore, the design goals may be stated as follows:

  (i) manipulator workspace should be close to a cube of prescribed size;
 (ii) kinematic performances within this cube should be quasi-isotropic;
(iii) link lengths should be minimal to lower the manufacturing costs.

The requirements (i) and (ii) will be satisfied in Section 4 by constraining the manipulability, condition number and/or velocity transmission factor inside the Cartesian workspace bounded by the joint limits. To fulfil requirement (iii), Section 5 evaluates the largest cube inscribed in this workspace, which defines the smallest link lengths required to achieve the prescribed cube size.

The design parameters to be optimised are the parallelogram length L, the actuated joint limits (ρ_{min}, ρ_{max}) and related location of the prescribed cube (p_{min}, p_{max}). Taking into account the linear relation between L and the workspace size, the design process is decomposed into two stages:

(i) defining the joint limits (ρ_{min}, ρ_{max}) and the largest cube size/location (p_{min}, p_{max}) to satisfy given kinematic performances for the normalised manipulator ($L = 1$);
(ii) scaling the normalised manipulator parameters to achieve the prescribed size of the cubic workspace.

Numerical example for this two-stage design process is given in Section 6.

3. Jacobian analysis

3.1. Jacobian matrix

As follows from the previous Section and a companion paper [17], the singularity-free workspace of the Orthoglide W_0 is located within the sphere S_L of radius L with the centre point $(0,0,0)$ and bounded by the parallel "*flat*" singularity surface in the first octant (Fig. 3). Also, the remaining part of the sphere surface corresponds to the parallel "*bar*" singularity. Hence, the kinematic design should define the inner part of this workspace that possesses the desired kinematic properties.

Mathematically, these properties are defined by the manipulator Jacobian describing the differential mapping from the jointspace to the workspace (or vice versa). For the Orthoglide, it is more convenient to express analytically the inverse Jacobian, which is derived from (1) in a straightforward way:
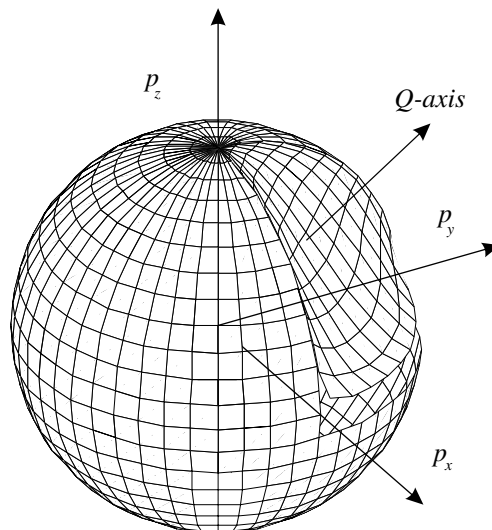

Fig. 3. The singularity-free workspace of the Orthoglide (97.2% of the sphere volume).

$$\mathbf{J}^{-1}(\boldsymbol{p}, \boldsymbol{\rho}) = \begin{bmatrix} 1 & p_y/(p_x - \rho_x) & p_z/(p_x - \rho_x) \\ p_x/(p_y - \rho_y) & 1 & p_z/(p_y - \rho_y) \\ p_x/(p_z - \rho_z) & p_y/(p_z - \rho_z) & 1 \end{bmatrix}. \tag{5}$$

Accordingly, the determinant of the Jacobian may be expressed as

$$\det(\mathbf{J}^{-1}) = \frac{p_x\rho_y\rho_z + \rho_x p_y \rho_z + \rho_x \rho_y p_z - p_x p_y p_z}{(p_x - \rho_x)(p_y - \rho_y)(p_z - \rho_z)} \tag{6}$$

and admits two cases of ill-conditioning, $\det(\mathbf{J}) = 0$ and $\det(\mathbf{J}^{-1}) = 0$, corresponding to the serial and parallel singularities mentioned above. It is also clear that the full isotropy is achieved only in the "zero" point $\mathbf{p}_0 = (0, 0, 0)$, where the Jacobian reduces to the identity matrix: $\mathbf{J}_0 = \mathbf{I}$.

3.2. Q-axis properties

Since the Orthoglide workspace is symmetrical with respect to the axes x, y, z, its kinematic design requires a detailed study of the points belonging to the Q-axis, which is the bisector line of the first octant [16]. For this axis, let us denote $p_x = p_y = p_z = p$ and, consequently, $\rho_x = \rho_y = \rho_z = \rho$. Then, as follows from (5), the inverse Jacobian may be presented as:

$$\mathbf{J}^{-1}(\chi) = \begin{bmatrix} 1 & \chi & \chi \\ \chi & 1 & \chi \\ \chi & \chi & 1 \end{bmatrix}, \tag{7}$$

where χ is the dimensionless scalar parameter expressed as $\chi = -p/\sqrt{L^2 - 2p^2}$ and related to the input/output variables via the expressions $p = -\chi L/\sqrt{1 + 2\chi^2}$; $\rho = (1 - \chi)L/\sqrt{1 + 2\chi^2}$. To define the feasible range of the parameter χ, let us consider specific points belonging to the Q-axis (see Fig. 4 and Table 1). They include three parallel singularity points P_1, P_2, P_3 and one serial singularity point P_4. As follows from the analysis, the singularity-free region of the Q-axis is bounded by the interval $\chi \in (-0.5, 1.0)$ which corresponds to the coordinate ranges $p \in (-L/\sqrt{3}, L/\sqrt{6})$; $\rho \in (0, \sqrt{3/2}L)$. It is important for the kinematic design that, within these limits, the relation between the coordinates p, ρ and the parameter χ is monotonously decreasing (see Table 1). It should be also noted that the employed parameterisation may be converted to the one used in
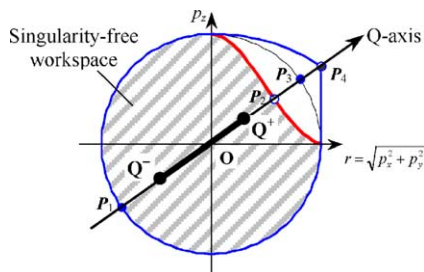

Fig. 4. Workspace regions for the Q-axis.

Table 1
Specific points in the Q-axis for the unit manipulator ($L = 1$)

Feature	P_1	O	P_2	P_3	P_4
p	$-\sqrt{1/3}$	0	$\sqrt{1/6}$	$\sqrt{1/3}$	$\sqrt{1/2}$
ρ	0	1	$\sqrt{3/2}$	$\sqrt{4/3}$	$\sqrt{1/2}$
χ	1	0	-0.5	-1	$-\infty$
$\det(\mathbf{J})$	∞	1	∞	∞	0

[16] by defining $\chi = -\tan(\theta)$, where θ is the angle between the manipulator links and corresponding prismatic joint axes.

4. Dexterity-based design

Since the design specifications require the manipulator to possess the quasi-isotropic kinematics [18–20], the original joint limits (2) must be narrowed to increase the distance from the dextrous workspace points to the singularities. In this section, the desired joint limits are computed using the Q-axis technique, which reduces the problem to locating two points Q^+ and Q^- on the bisector line (see Fig. 4). These points bound the Q-axis region with the required properties and, therefore, define the joint limits. It is obvious that the interval $[Q^+, Q^-]$ must include the fully-isotropic "zero" point O, and the kinematic performances at the points Q^+, Q^- should be similar. To compute the joint limits, we apply three different criteria evaluating the workspace dexterity. It should be also mentioned that all results of this section are valid for the "unit" manipulator ($L = 1$), which will be scaled on the subsequent design steps.

4.1. Constraining the manipulability

The manipulator manipulability $w = \sqrt{\det(\mathbf{J}^{-1}\mathbf{J}^{-T})}$ is the simplest performance measure assessing the dexterity [21], which is the product of the singular values of the Jacobian or its inverse. For the Q-axis, where $\mathbf{J}^{-1}$ is a square and symmetrical matrix, the manipulability can be computed as

$$w = |\det(\mathbf{J}^{-1})| = (1 - \chi)^2 \cdot |1 + 2\chi|, \tag{8}$$

where $\chi \in \,]-0.5, 1.0[$. As follows from (6), the maximum value of the manipulability w is equal to 1 and is achieved in the "zero" (isotropic) point

$$\det(\mathbf{J}^{-1}(\mathbf{p}_0)) = 1, \quad \det(\mathbf{J}^{-1}(\mathbf{p})) < 1 \quad \text{if } \mathbf{p} \neq \mathbf{p}_0. \tag{9}$$

Therefore, the joint limits can be found from the inequality

$$\det(\mathbf{J}^{-1}(\rho)) \geqslant \Delta \quad \forall \rho \in [\rho_{\min}, \rho_{\max}], \tag{10}$$

where Δ is the prescribed lower bound of the manipulability ($\Delta < 1$). Since the relation $\rho(\chi)$ is monotonous and $\chi = 0$ corresponds to the isotropic posture (see Section 3.2), the desired parameter range can be obtained from the cubic equation $2\chi^3 - 3\chi^2 + (1 - \Delta) = 0$ by selecting two roots closest to zero. Applying the trigonometric method, it can be obtained that $\chi_1 = 0.5 - \cos(\varphi/3)$,
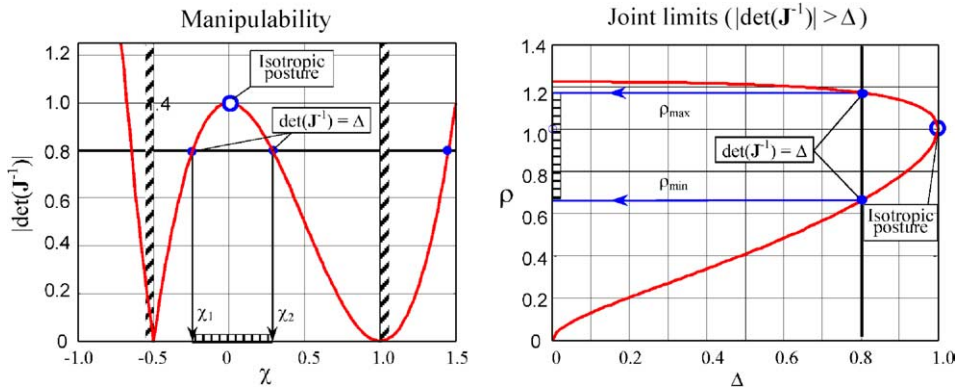
Fig. 5. Computing joint limits via the manipulability index.

$\chi_2 = 0.5 + \cos(\varphi/3 - \pi/3)$, where $\varphi = \mathrm{acos}(1 - 2\Delta)$, $\chi_1 < 0$, $\chi_2 > 0$, and, consequently, $\rho_{\min} = \rho(\chi_2)$; $\rho_{\max} = \rho(\chi_1)$ and $p_{\min} = p(\chi_2)$; $p_{\max} = p(\chi_1)$, where functions $\rho(\chi)$ and $p(\chi)$ are defined in Section 3.2. The graphical interpretation of this result is presented in Fig. 5. The open question, however, is how to interpret the manipulability design specification Δ in engineering sense, to be understandable for the designer with a practical background.

4.2. Constraining the condition number

The Jacobian condition number evaluates the distance to the singularities by the ratio of the largest to the smallest matrix eigenvalues, which is also the ratio of the largest and smallest axis length of the manipulability ellipsoid [21]. As follows from (5), the Orthoglide condition number achieves its best value (equal to 1) in the zero point, while in other workspace points it is greater than 1:

$$\mathrm{cond}(\mathbf{J}^{-1}(\mathbf{p}_0)) = 1, \quad \mathrm{cond}(\mathbf{J}^{-1}(\mathbf{p})) > 1, \ \text{if} \ \ \mathbf{p} \neq \mathbf{p}_0. \tag{11}$$

Hence, the joint limits can be found from the inequality

$$\mathrm{cond}(\mathbf{J}^{-1}(\rho)) \leqslant \delta \quad \forall \rho \in [\rho_{\min}, \rho_{\max}], \tag{12}$$

where δ is the admitted upper bound of this performance index ($\delta > 1$). Since along the Q-axis the inverse Jacobian is symmetrical, the condition number can be computed via the ratio of the largest to the smallest eigenvalues of $\mathbf{J}^{-1}$. The relevant characteristic equation $\det(\mathbf{J}^{-1} - \lambda\mathbf{I}) = 0$ may be rewritten as $\lambda^3 - 3\lambda^2 + 3(1 - \chi^2)\lambda - (1 - \chi)^2(2\chi + 1) = 0$. Its analytical solution yields $\lambda_1 = 1 + 2\chi$; $\lambda_{2,3} = 1 - \chi$. Therefore, the condition number for the Q-axis can be expressed as

$$\mathrm{cond}(\mathbf{J}^{-1}(\chi)) = \begin{cases} 1 + 3\chi/(1 - \chi) & \text{if } \chi \in]0, 1[, \\ 1 - 3\chi/(1 + 2\chi) & \text{if } \chi \in] - 0.5, 0] \end{cases} \tag{13}$$

and the desired parameter range $[\chi_1, \chi_2]$ can be obtained from the equations $\chi_1 = -(\delta - 1)/(2\delta + 1)$, $\chi_2 = (\delta - 1)/(\delta + 2)$. Hence, $\rho_{\min} = \rho(\chi_2)$; $\rho_{\max} = \rho(\chi_1)$ and $p_{\min} = p(\chi_2)$; $p_{\max} = p(\chi_1)$, where functions $\rho(\chi)$ and $p(\chi)$ are defined in Section 3.2. The graphical interpretation of this result is presented in Fig. 6. The question of defining a reasonable value of δ is simpler is this case because it possesses clearer geometric meaning and is rather understandable for practising engineers.
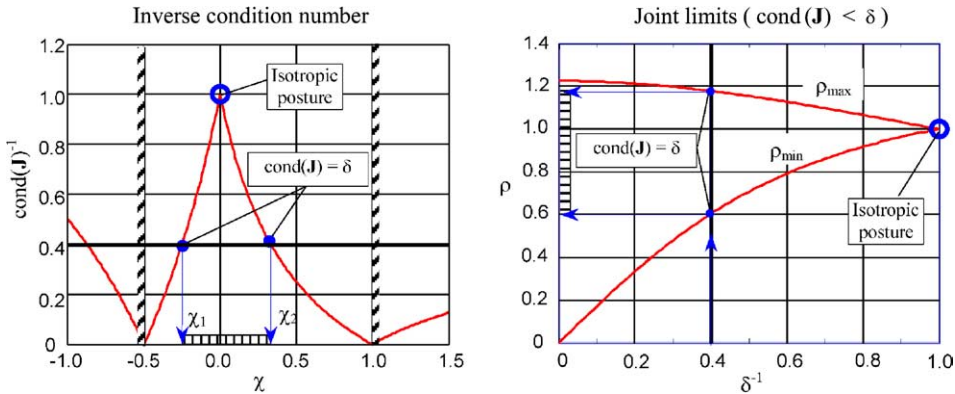
Fig. 6. Computing joint limits via the condition number.

4.3. Constraining the velocity transmission factor

The velocity transmission factor assesses the ratio of the manipulator end-point velocity and velocity of the corresponding point in the joint space. For a given workspace point p and direction of motion $\mathbf{e}$, it can be computed via the Jacobian as $\lambda(\mathbf{p},\mathbf{e}) = ||\mathbf{J}^{-1}(\mathbf{p}) \cdot \mathbf{e}||^{-1}$ where $\mathbf{e}^T\mathbf{e} = 1$. As known from the matrix theory, the deviation of this factor for the fixed p is bounded by the smallest and largest singular values of $\mathbf{J}$. Geometrically, this performance index is directly related to the manipulability ellipsoid, which in the previous section was evaluated by the ratio of its longest and shortest axes, while here these axes are assessed separately.

As follows from (5), the Orthoglide velocity transmission factor does not depend on the direction of motion in the zero point and in the remaining points it varies depending on $\mathbf{e}$

$$\min_{\mathbf{e}} \lambda(\mathbf{p},\mathbf{e}) < 1, \quad \max_{\mathbf{e}} \lambda(\mathbf{p},\mathbf{e}) > 1 \quad \text{if } \mathbf{p} \neq \mathbf{p}_0. \tag{14}$$

Hence, for this performance measure, the joint limits can be found from the inequality

$$\lambda_{\min} \leqslant \lambda(\rho,\mathbf{e}) \leqslant \lambda_{\max} \quad \forall \rho \in [\rho_{\min}, \rho_{\max}] \quad \forall \mathbf{e} : || \mathbf{e} || = 1, \tag{15}$$

where $\lambda(\rho,\mathbf{e})$ denotes the velocity transmission factor along the Q-axis, and $\lambda_{\min}$, $\lambda_{\max}$ are the design specifications ($\lambda_{\min} < 1 < \lambda_{\max}$).

Since along the Q-axis the Jacobian is symmetrical, the transmission factor range may be derived from the eigenvalues obtained in the Section 4.2. It has been also proved that the eigenvalue $\lambda_1 = 1 + 2\chi$ corresponds to the eigenvector directed along the Q-axis, and two remaining coinciding eigenvalues $\lambda_{2,3} = 1 - \chi$ correspond to the eigenvectors, which are perpendicular to this axis. So, the desired parameter range $[\chi_1, \chi_2]$ can be computed from the expressions

$$\chi_1 = \max\{1 - \lambda_{\max}, (\lambda_{\min} - 1)/2\}, \quad \chi_2 = \min\{1 - \lambda_{\min}, (\lambda_{\max} - 1)/2\}. \tag{16}$$

Graphical interpretation of this result is presented in Fig. 7. The question of defining reasonable values of $\lambda_{\min}$, $\lambda_{\max}$ is very clear in this case. For instance $\lambda \in [\mu, 1/\mu]$ with $\mu \in [0.5, 1.0]$ possesses sensible meaning and is quite understandable for practising engineers. Impact of the transmission
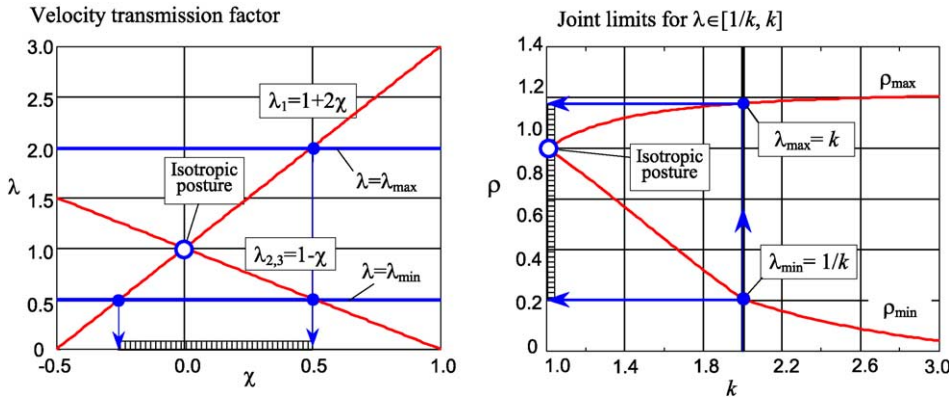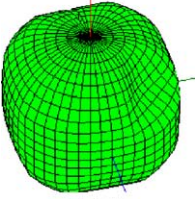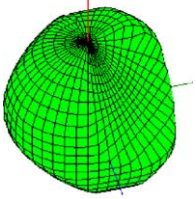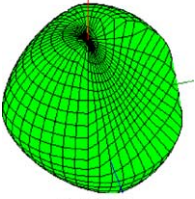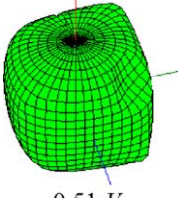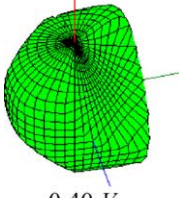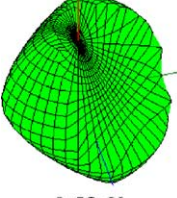
Fig. 7. Computing the joint limits the velocity transmission factors.

Table 2
Dextrous workspace for different bounds on the velocity transmission factor

Lower bounding	Two-sided bounding	Upper bounding
$\mu \geq 1/3$	$\mu \in [1/3, \ 3]$	$\mu \leq 3$
$0.84 \cdot V_0$	$0.67 \cdot V_0$	$0.72 \cdot V_0$
$\mu \geq 1/2$	$\mu \in [1/2, \ 2]$	$\mu \leq 2$
$0.51 \cdot V_0$	$0.40 \cdot V_0$	$0.52 \cdot V_0$

factor bounding on the dextrous workspace shape/size is also illustrated in Table 2, where all cases are quantified relative to the volume of the singularity-free workspace V_0 (see Fig. 3). To generate these shapes, we executed spanning of all possible directions from the isotropic point and dichotomic search for the line segments satisfying the kinematic constraints.

5. Workspace-based design

After applying the Q-axis technique, which yields the joint limits ensuring the prescribed dexterity for the bisector line, the whole workspace must be verified for kinematic performances. In this Section, this problem is solved by identifying and evaluating the workspace "critical points" and relevant definition of the joint limits. Then, the largest cube is inscribed in the dextrous workspace of the unit manipulator, which gives the scaling factor to meet the specifications for the desired cubic workspace size. It should be noted that here the manipulator dexterity is evaluated by the velocity transmission factors, which, as stated above, have advantages over the manipulability and condition number indices in practical applications. But the main results are also generalised for the manipulability and condition number criterions.

5.1. Workspace critical points

Let us consider first the unit Orthoglide ($L = 1$) with given joint limits $\rho_{min} \in [0, 1]$, $\rho_{max} \in [1, \sqrt{3/2}]$ and estimate the velocity transmission factors μ_{min}, μ_{max} over the corresponding workspace, which is bounded by six surfaces presented in Fig. 8. Since the manipulator has a symmetric geometric structure, the candidate points for extreme values of μ are located symmetrically on the workspace boundary and must be selected from the following sets:

(i) *vertex points*, for which all three joint coordinates ρ_x, ρ_y, ρ_z are equal to either ρ_{min} or ρ_{max};
(ii) *edge points*, for which 2 of 3 joint coordinates ρ_x, ρ_y, ρ_z are equal to either ρ_{min} or ρ_{max};
(iii) *face points*, for which 1 of 3 joint coordinates ρ_x, ρ_y, ρ_z is equal to either ρ_{min} or ρ_{max}.

It is also obvious that the inner workspace points possess better dexterity than their boundary counterparts (since the straight line motion from the zero point to any boundary point causes monotonous changing of the angles θ_x, θ_y, θ_z and corresponding decreasing of the transmission factors for each axis). Besides, as follows from a detailed investigation, only three types of points, Q, R, and S, compete to define the global measure of the workspace performances. Hence, the problem of this section is reduced to choosing the worst transmission factor from these points.
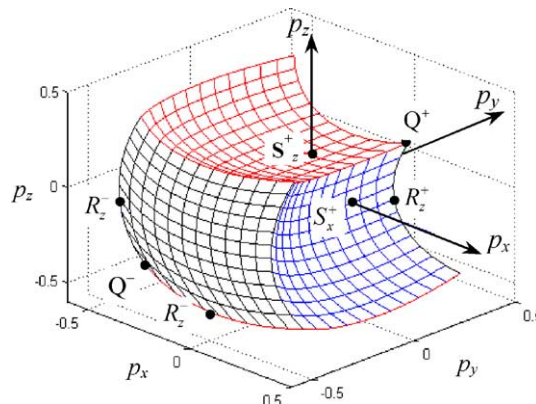

Fig. 8. The ρ-bounded workspace and its critical points.

5.1.1. Vertex points Q^+, Q^-

For the points Q^+ and Q^-, which are located at the intersection of the workspace boundary and the bisector line (i.e. the Q-axis)

$$Q^+ : \mathbf{p} = (p_1, p_1, p_1), \quad \rho = (\rho_{max}, \rho_{max}, \rho_{max});$$
$$Q^- : \mathbf{p} = (p_2, p_2, p_2), \quad \rho = (\rho_{min}, \rho_{min}, \rho_{min});$$

the Jacobian is symmetrical, so the transmission factors μ_i are equal to the inverses $1/\lambda_1$ and $1/\lambda_{2,3}$ of the eigenvalues $\lambda_1 = 1 + 2\chi$ and $\lambda_{2,3} = 1 - \chi$ (see Section 4.3). The parameter χ is related to the Cartesian coordinates $(p_x, p_y, p_z = p)$ by the expression $\chi = -p/\sqrt{1 - 2p^2}$, where p_1, p_2 are expressed as

$$p_1 = \frac{1}{3}\left(\rho_{max} - \sqrt{3 - 2\rho_{max}^2}\right), \quad p_2 = \frac{1}{3}\left(\rho_{min} - \sqrt{3 - 2\rho_{min}^2}\right) \tag{17}$$

and corresponds to Q^+ and Q^- respectively.

5.1.2. Edge points $R_x^+, \ldots, R_z^-$

For the points R_x^+ and R_x^-, which are defined at the intersection of the workspace boundary and the XY-plane

$$R_x^+ : \mathbf{p} = (p_1, p_1, 0), \quad \rho = (\rho_{max}, \rho_{max}, \rho_1),$$
$$R_x^- : \mathbf{p} = (p_2, p_2, 0); \quad \rho = (\rho_{min}, \rho_{min}, \rho_2)$$

the inverse Jacobian is

$$\mathbf{J}^{-1}(\chi) = \begin{bmatrix} 1 & \chi & 0 \\ \chi & 1 & 0 \\ \chi/\sqrt{1-\chi^2} & \chi/\sqrt{1-\chi^2} & 1 \end{bmatrix}, \tag{18}$$

where $\chi = -p/\sqrt{1 - p^2}$ and p is equal to either p_1 or p_2. Using the Orthoglide kinematic equation (1), the Cartesian coordinates may be expressed as

$$p_1 = \left(\rho_{max} - \sqrt{2 - \rho_{max}^2}\right)/2, \quad p_2 = \left(\rho_{min} - \sqrt{2 - \rho_{min}^2}\right)/2 \tag{19}$$

and, subsequently,

$$\rho_1 = \sqrt[4]{\rho_{max}^2(2 - \rho_{max}^2)} \in (1, \rho_{max}), \quad \rho_2 = \sqrt[4]{\rho_{min}^2(2 - \rho_{min}^2)} \in (\rho_{min}, 1). \tag{20}$$

Since the matrix (18) is asymmetrical, the velocity transmission factors are to be computed from the product of the Jacobian by its transpose

$$\left(\mathbf{J} \cdot \mathbf{J}^T\right)^{-1} = \begin{bmatrix} 1+\chi^2 & 2\chi & \left(\chi+\chi^2\right)/\sqrt{1-\chi^2} \\ 2\chi & 1+\chi^2 & \left(\chi+\chi^2\right)/\sqrt{1-\chi^2} \\ \left(\chi+\chi^2\right)/\sqrt{1-\chi^2} & \left(\chi+\chi^2\right)/\sqrt{1-\chi^2} & \left(1+\chi^2\right)/\left(1-\chi^2\right) \end{bmatrix}. \tag{21}$$

The corresponding characteristic equation may be presented as $(\sigma - (1 - \chi)^2) \cdot (\sigma^2 - A\sigma + B) = 0$, where $A = (1 + \chi)^2 + (1 + \chi^2)/(1 - \chi^2); \quad B = (1 + \chi)^2$. So, the singular values $\lambda = \sqrt{\sigma}$ are

$$\lambda_1 = 1 - \chi, \quad \lambda_{2,3} = \sqrt{\frac{1}{2}\left(A \pm \sqrt{A^2 - 4B}\right)} \tag{22}$$

and the velocity transmission factors can be computed as $1/\lambda_1$, $1/\lambda_2$, and $1/\lambda_3$. It is clear that, because of the symmetry, these assessments are also valid for the remaining points R_y^+, R_y^- and R_z^+, R_z^-.

5.1.3. Face points $S_x^+, \ldots, S_z^-$

For the points S_x^+ and S_x^-, which are defined at the intersection of the workspace boundary and the X-axis

$$S_x^+ : \quad \mathbf{p} = (p_1, 0, 0), \quad \rho = (\rho_{\max}, \rho_1, \rho_1),$$
$$S_x^- : \quad \mathbf{p} = (p_2, 0, 0), \quad \rho = (\rho_{\min}, \rho_2, \rho_2)$$

the inverse Jacobian is

$$\mathbf{J}(\chi)^{-1} = \begin{bmatrix} 1 & 0 & 0 \\ \chi & 1 & 0 \\ \chi & 0 & 1 \end{bmatrix}, \tag{23}$$

where $\chi = -p/\sqrt{1 - p^2}$ and p is equal to either p_1 or p_2. Using the basic kinematic equation (1), the latter may be expressed as $p_1 = \rho_{\max} - 1; \quad p_2 = \rho_{\min} - 1$, and, subsequently,

$$\rho_1 = \sqrt{\rho_{\max}(2 - \rho_{\max})} \in [1, \rho_{\max}], \quad \rho_2 = \sqrt{\rho_{\min}(2 - \rho_{\min})} \in [\rho_{\min}, 1]. \tag{24}$$

Since the matrix (23) is asymmetrical, the velocity amplification factors must be computed from the product of the Jacobian and its transpose

$$\left(\mathbf{J} \cdot \mathbf{J}^T\right)^{-1} = \begin{bmatrix} 2 + \chi^2 & \chi & \chi \\ \chi & 1 & 0 \\ \chi & 0 & 1 \end{bmatrix}. \tag{25}$$

The corresponding characteristic equation may be written as $(\sigma - 1) \cdot (\sigma^2 - 2(1 + \chi^2)\sigma + 1) = 0$. Hence, the singular values $\lambda = \sqrt{\sigma}$ are

$$\lambda_1 = 1, \quad \lambda_{2,3} = \sqrt{(1 + \chi^2) \pm \chi\sqrt{2 + \chi^2}} \tag{26}$$

and the velocity transmission factors can be computed as $1/\lambda_1$, $1/\lambda_2$, and $1/\lambda_3$. It is clear that similar results are also valid for the points S_y^+, S_y^- and S_z^+, S_z^-.

5.2. Global performance indices

After evaluation of the transmission factors at the points Q, R, S, these points can be classified with respect to the influence on the global performance indices $\mu_{\min}$, $\mu_{\max}$ throughout the work-

space W_ρ bounded by $\rho \in [\rho_{\min}, \rho_{\max}]$. Here, the global performance indices are defined as the lower and upper bounds of the velocity transmission factors within W_ρ. Since the prescribed workspace must be singularity-free, the allowable joint limits should belong to the rectangle $(\rho_{\min}, \rho_{\max}) \in [0, 1] \times [1, \sqrt{1.5}]$.

5.2.1. Contour plots of global indices

Detailed investigation of the joint limit rectangle based on both analytical and numerical tools has yielded results presented in Fig. 9, which contains the contour plots of $\mu_{\min}, \mu_{\max}$ on the plane $\rho_{\min}, \rho_{\max}$. These plots are labelled by the relevant values of the velocity transmission factors and divided in separate areas, which differ by a type of the critical points. For instance, the contour plot for the function $\mu_{\min}(\rho_{\min}, \rho_{\max})$ consists of four areas, S^-, R^-, Q^- and Q^+, where the global transmission factors are defined by the critical points $\{S_x^-, S_y^-, S_z^-\}$, $\{R_x^-, R_y^-, R_z^-\}$, Q^- and Q^+ respectively. For comparison purposes, we also show by the dashed/dotted lines the one-dimensional subset of the joint limit rectangle, which corresponds to the "symmetrical" design constrains (i.e. $\mu_{\min} = 1/\mu_{\max}$) imposed either on the full ρ-bounded workspace or along the Q-axis only.

As follows from Fig. 9a, the global minimum of the transmission factor can be achieved in either points S_i^-, R_i^-, or Q^-, where $i \in \{x, y, z\}$ and all these indices are equivalent with respect to the $\mu_{\min}, \mu_{\max}$ because of the symmetry. It has been proved, that particular expressions for computing of $\mu_{\min}$ are

$$\mu_{\min}(\rho_{\min}, \rho_{\max}) = \begin{cases} \lambda_2(S_i^-)^{-1} & \text{for } \rho_{\min} \in]0, \rho_{SR}], \\ \lambda_2(R_i^-)^{-1} & \text{for } \rho_{\min} \in]\rho_{SR}, \rho_{RQ}], \\ \lambda_2(Q^-)^{-1} & \text{for } \rho_{\min} \in]\rho_{RQ}, \varphi_{QQ}(\rho_{\max})], \\ \lambda_1(Q^+)^{-1} & \text{for } \rho_{\min} \in]\varphi_{QQ}(\rho_{\max}), \ 1], \end{cases} \quad (27)$$

where the subscripts of λ define the number of the critical singular value $(1, \ldots, 3$, in accordance with the above notation), and the critical points S_i^-, R_i^- and Q^- are separated by the vertical lines
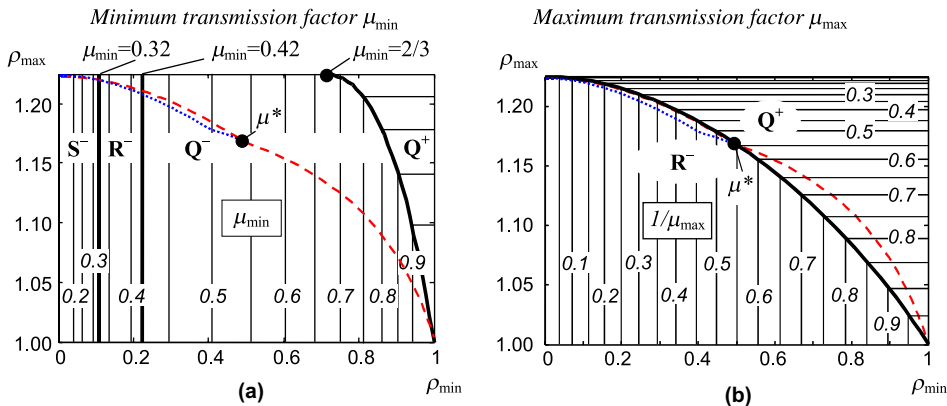

Fig. 9. Contour plots of the global transmission factors $\mu_{\min}$, $\mu_{\max}$ on the plane $\rho_{\min} \times \rho_{\max}$ (dashed/dotted lines correspond to symmetrical constraints for W_ρ / Q-axis; $\mu^* \approx 0.54$).

$\rho_{SR} = 0.1093$ and $\rho_{RQ} = 0.2240$ shown in bold in Fig. 9a (corresponding values of the transmission factor are $\mu_{\min}(\rho_{SR}) = 0.3232$ and $\mu_{\min}(\rho_{RQ}) = 0.4210$). The critical points Q^+, Q^- are separated by the curve $\rho_{\min} = \varphi_{QQ}(\rho_{\max})$, which can be obtained by equating the eigenvalues $\lambda_1 = 1 + 2\chi$ and $\lambda_2 = 1 - \chi$ for Q^+ and Q^-, respectively. Hence, using the relation between the auxiliary variable χ and the joint coordinate along the Q-axis $\rho = (1 - \chi)/\sqrt{1 + 2\chi^2}$, the equations for the function $\varphi_{QQ}(\rho_{\max})$ can be presented both in the parametric

$$\rho_{\min} = (1 - \chi)/\sqrt{1 + 2\chi^2}, \quad \rho_{\max} = (1 + 2\chi)/\sqrt{1 + 8\chi^2} \quad \chi \in \,]0, \ 1/4[\tag{28a}$$

and explicit form

$$\rho_{\max}^2 = 3(3 - 2\rho_{\min}^2) \Big/ \left((9 - 2\rho_{\min}^2) - 4\rho_{\min}\sqrt{3 - 2\rho_{\min}^2} \right), \quad \rho_{\min} \in \,]\sqrt{0.5}, \ 1.0[. \tag{28b}$$

It can be also shown that along this curve the corresponding velocity transmission factor $\mu_{\min} = 1/(1 + 2\chi)$ varies from 1 to 2/3, and the curve is bounded by the points $(1, 1)$ and $(\sqrt{0.5}, \sqrt{1.5})$.

Similar analysis for the global maximum of $\mu_{\max}$ (Fig. 9b) shows that it can be achieved in either point R_i^- or Q^+, i.e.

$$\mu_{\max}(\rho_{\min}, \rho_{\max}) = \begin{cases} \lambda_1(R_i^-)^{-1} & \text{for } \rho_{\max} \in \,]1, \ \varphi_{RQ}(\rho_{\min})], \\ \lambda_1(Q^+)^{-1} & \text{for } \rho_{\max} \in \,]\varphi_{RQ}(\rho_{\min}), \ \sqrt{1.5}[, \end{cases} \tag{29}$$

where the subscripts of λ and R have similar meaning as in (27), and the critical points R_i^- and Q^+ are separated by the curve $\rho_{\min} = \varphi_{RQ}(\rho_{\max})$. This curve can be obtained by equating the eigenvalues $\lambda_1 = 1 - \chi$ and $\lambda_1 = 1 + 2\chi$, respectively, for R_i^- and Q^+. Hence, using the relations between the auxiliary variable χ and the joint coordinates of the Q-points $\rho_Q = (1 - \chi)/\sqrt{1 + 2\chi^2}$ and R-point $\rho_R = (1 - \chi)/\sqrt{1 + \chi^2}$, the equations for the function $\varphi_{RQ}(\rho_{\max})$ can be presented both in the parametric

$$\rho_{\max} = (1 - \chi)/\sqrt{1 + 2\chi^2}, \quad \rho_{\min} = (1 + 2\chi)/\sqrt{1 + 4\chi^2}, \quad \chi \in \,] - 1/2, 0[\tag{30a}$$

and explicit forms

$$\rho_{\min}^2 = \frac{9(3 - 2\rho_{\max}^2)}{(15 - 2\rho_{\max}^2) - 4\rho_{\max}\sqrt{3 - 2\rho_{\max}^2}} \quad \rho_{\max} \in \,]1, \ \sqrt{3/2}[. \tag{30b}$$

It can be also shown that along this curve the corresponding velocity transmission factor $\mu_{\max} = 1/(1 + 2\chi)$ varies from 1 to ∞, and the curve is bounded by the points $(1, 1)$ and $(0, \sqrt{1.5})$.

Neighbourhood of the isotropic point. Since the kinematic design seeks for the quasi-isotropic workspace, it is useful to obtain analytical expressions for $\mu_{\min}$ in the neighbourhood of the isotropic point $(1, 1)$, which is completely defined by the Q-axis (see Fig. 9a). As proved above, for both Q^+ and Q^- the auxiliary parameter χ may be expressed via the joint variable as $\chi_Q = (1 - \rho\sqrt{3 - 2\rho^2})/(2\rho^2 - 1)$, hence in this case (27) may be reduced up to

$$\mu_{\min} = \begin{cases} \frac{1}{3} + \frac{2\rho_{\min}}{3\sqrt{3 - 2\rho_{\min}^2}} & \text{if } \rho_{\max} \geqslant \varphi_{QQ}(\rho_{\max}), \\ \frac{2}{3} + \frac{\sqrt{3 - 2\rho_{\max}^2}}{3\rho_{\max}} & \text{otherwise.} \end{cases} \tag{31}$$

Rewriting these expressions with respect to $\mu_{\min}$ yields

$$Q^- : \; \rho_{\min} \geqslant \frac{3\mu_{\min} - 1}{\sqrt{6\mu_{\min}^2 - 4\mu_{\min} + 2}}, \quad Q^+ : \; \rho_{\max} \leqslant \frac{1}{3\mu_{\min}^2 - 4\mu_{\min} + 2}, \tag{32}$$

which allow to compute the joint limits $\rho_{\min}$, $\rho_{\max}$ for given design specification $\mu_{\min} \geqslant \mu^0$ (provided that $\mu_{\min} \geqslant \mu(\rho_{SR}) \approx 0.32$). For the wider range of $\mu_{\min}$, the relevant equation was solved numerically and corresponding plots are presented in Fig. 10.

Similar expressions for $\mu_{\max}$ can be derived by substitution of

$$\chi_R = \left(1 - \rho_{\min}\sqrt{2 - \rho_{\min}^2}\right) \Big/ (\rho_{\min}^2 - 1), \quad \chi_Q = \left(1 - \rho_{\max}\sqrt{3 - 2\rho_{\max}^2}\right) \Big/ (2\rho_{\max}^2 - 1)$$

into equations for the roots $\lambda_1 = 1 - \chi_R$ and $\lambda_1 = 1 + 2\chi_Q$ and relevant simplification:

$$\mu_{\max} = \begin{cases} \frac{1}{3} + \frac{2\rho_{\max}}{3\sqrt{3 - 2\rho_{\max}^2}} & \text{if } \rho_{\min} \leqslant \varphi_{RQ}(\rho_{\max}), \\ \frac{1}{2} + \frac{\sqrt{2 - \rho_{\min}^2}}{2\rho_{\min}} & \text{otherwise.} \end{cases} \tag{33}$$

Rewriting these expressions with respect to $\mu_{\max}$ yields

$$R^- : \; \rho_{\min} \geqslant \frac{1}{\sqrt{2\mu_{\max}^2 - 2\mu_{\max} + 1}}, \quad Q^+ : \; \rho_{\max} \leqslant \frac{2\mu_{\max} - 1}{\sqrt{6\mu_{\max}^2 - 4\mu_{\max} + 2}}, \tag{34}$$

which make it possible to compute the joint limits $\rho_{\min}, \rho_{\max}$ for given design specification $\mu_{\max} \leqslant 1/\mu$ (see Fig. 10).

5.2.2. Symmetrical design specification

The above results can be also used in the case of the "symmetrical" design specification, which assumes the inverse relations between the upper and lower bound on the transmission factor ($\mu_{\min} = 1/\mu_{\max}$), when the feasible workspace is defined by the expression

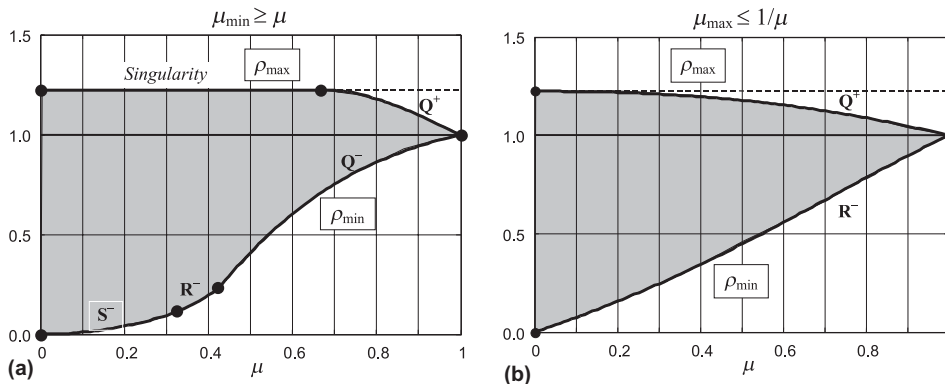$$\min_{\mathbf{p} \in W_\rho} \{\mu_{\min}(\mathbf{p}), \; 1/\mu_{\max}(\mathbf{p})\} \geqslant \mu \tag{35}$$

Fig. 10. Computing joint limits for non-symmetrical constraints (independent upper and lower bounding).

in which $\mu \in [0,1]$ is the value of the prescribed performance measure (for instance, it is natural to set the transmission factor to be in the range $[1/2, 2]$ or $[1/3, 3]$, as it was proposed in [8]). As follows from the related analysis, in this case only two combinations of critical points are possible: (Q^+, Q^-) if $\mu \geqslant \mu^*$ and (Q^+, R_i^-) if $\mu < \mu^*$, where $\mu^* \approx 0.5387$, $\rho_{\min}(\mu^*) \approx 0.4892$, $\rho_{\max}(\mu^*) \approx 1.1700$ (see Fig. 9). So, as follows from (31) and (33), the joint limits for the symmetrical design specification can be computed as

$$Q^+: \ \rho_{\max} \leqslant \frac{3-\mu}{\sqrt{2\mu^2 - 4\mu + 6}}, \quad 0 < \mu < 1, \tag{36a}$$

$$Q^-: \ \rho_{\min} \geqslant \frac{3\mu - 1}{\sqrt{6\mu^2 - 4\mu + 2}}, \quad \mu^* \leqslant \mu < 1, \quad R^-: \ \rho_{\min} \geqslant \frac{\mu}{\sqrt{\mu^2 - 2\mu + 2}}, \quad 0 < \mu < \mu^*. \tag{36b}$$

This relation is shown in Fig. 11a on the $\rho_{\min} \times \rho_{\max}$ plane and also plotted in Fig. 11b against the velocity transmission factor μ. They make it possible to evaluate the global manipulator performance for the whole ρ-bounded workspace W_ρ (for given joint limits) or to compute the joint limits that guarantee the desired performances throughout W_ρ.

5.3. Defining a cubic workspace

Since the prescribed Cartesian workspace has a cubic shape, let us first define the largest cube that ensures the desired transmission factors $[\mu, 1/\mu]$ through it, while temporarily releasing the joint limits constraints. It is obvious, that due to the Orthoglide symmetrical architecture, the cube faces must be parallel to the xy, xz and yz planes. So, the constraint (15) may be rewritten as

$$\min_{\mathbf{p} \in W_p} \{\mu_{\min}(\mathbf{p}), \ 1/\mu_{\max}(\mathbf{p})\} \geqslant \mu, \tag{37}$$

where W_p denotes the p-bounded workspace determined by $p_x, p_y, p_z \in [p_{\min}, p_{\max}]$. Applying the above notation, the cube may be also defined by its two opposite vertices Q^+, Q^- located on the
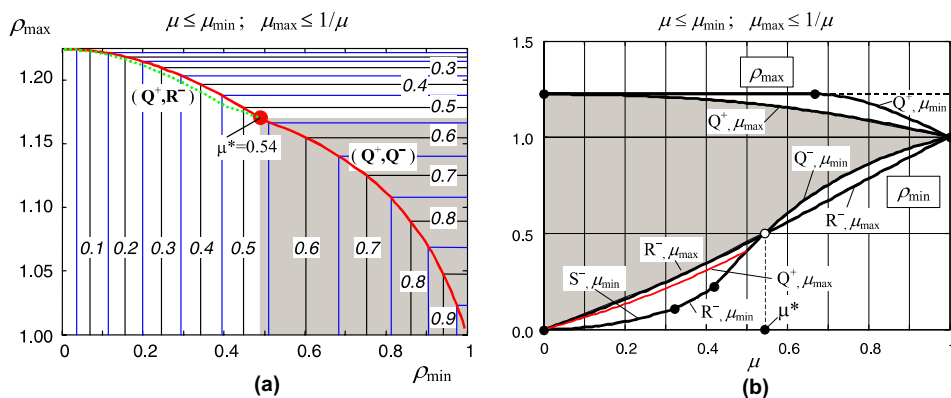

Fig. 11. Transmission factors (a) and joint limits (b) for symmetrical constraints within W_ρ (dashed line shows symmetrical constraints for Q-axis only).

bisector line. Detailed investigation of W_p using expressions from previous sub-sections is summarised in the following statement.

Proposition 1. *If the prescribed symmetrical bounds* $\mu(\mathbf{p}) \in [\mu, 1/\mu]$, $0 < \mu < 1$ *on the velocity transmission factors are satisfied at the Q-axis points* Q^+, Q^-, *then these bounds are satisfied throughout the cubic workspace* W_p *defined by the vertices* Q^+, Q^- *(and vice versa).*

The proof of the proposition uses convexity of the workspace hull bounded by $\mu(\mathbf{p}) \in [\mu, 1/\mu]$ and is based on comparing the Jacobian singular values in the critical points of the cubic workspace and on the expressions for the joint limits

$$\rho(Q^+) = \frac{3 - \mu}{\sqrt{2\mu^2 - 4\mu + 6}}, \quad \rho(Q^-) = \max\left\{ \frac{3\mu - 1}{\sqrt{6\mu^2 - 4\mu + 2}}, \frac{\mu}{\sqrt{2\mu^2 - 4\mu + 3}} \right\}, \tag{38}$$

which are derived from (31), (33). It should be noted that the ρ-bounded workspace defined by the same vertices Q^+, Q^- does not satisfy the bounds $[\mu, 1/\mu]$ if $\mu < \mu^* \approx 0.54$ (see Section 5.2), but the p-bounds remove the critical points R_x^+, R_y^+, ... R_z^-. Besides, utilising the cubic workspace with the vertices Q^+, Q^- requires a certain enlargement of the upper joint limit. Really, as follows from the basic Orthoglide equation (1), the p-bounded Cartesian workspace maps into the joint space portion, which is contained in the parallelepiped

$$\rho_x, \rho_y, \rho_z \in [\rho(Q^-), \ p(Q^+) + 1], \tag{39}$$

where $\rho(Q^-) = p_{\min} + \sqrt{1 - 2p_{\min}^2}$ is the joint coordinate at Q^-, $p(Q^+) = p_{\max}$ is the Cartesian coordinate at Q^+, and $p_{\min}, p_{\max}$ depend on the desired transmission factor bound μ and are computed from (31), (33). It can also be easily proved that $p(Q^+) + 1 > \rho(Q^+)$, since $\rho(Q^+) = p_{\max} + \sqrt{1 - 2p_{\max}^2}$ (see Section 5.1). Hence, this increase in the upper joint limit may lead to the singularities included in the corresponding ρ-bounded workspace, which can be avoided only by adding some "software joint limits" (based on verifying of inequalities more complicated than $\rho_{\min} \leqslant \rho_x \leqslant \rho_{\max}$ and similar). Relevant computations showed that the singularity problem arises for the transmission factors $\mu \leqslant 1 - \sqrt{\sqrt{1.5} - 1} \approx 0.53$ for which $p(Q^+) + 1 \sqrt{1.5}$.

The alternative approach for defining the cubic workspace assumes that the joint limits corresponding to Q^+, Q^- cannot be violated. Hence, the desired cube W_p^{o} should be completely enclosed in the ρ-bounded space W_ρ. It is obvious that $W_p^{\mathrm{o}} \subset W_p$, so within the cube W_p^{o} the manipulator possesses the desired kinematic properties. Dimension of the cube W_p^{o} and its spatial location are defined by the following proposition.

Proposition 2. *If the prescribed symmetrical bounds* $\mu(\mathbf{p}) \in [\mu, 1/\mu]$, $0 < \mu < 1$ *are satisfied in the Q-axis points* Q^+, Q^-, *then the largest cube enclosed in the ρ-bounded workspace W_ρ is defined by the vertices* Q_*^+ *and* Q^-, *where* $Q_*^+ \in [Q^+ Q^-]$ *and* $p(Q_*^+) = \rho(Q^+) - 1$.

The proof of this proposition is based on comparing the Cartesian coordinates for the critical points Q, R, S (see Fig. 8) and also uses the expression for the upper joint limit from Proposition 1. It is clear, that in this case the ρ-bounded workspace defined by Q^+, Q^- is singularity-free, but its global performances may be out of the design specifications in R_2-points and their neighbourhood if $\mu < 0.54$ (see Section 5.2). So, the designer may choose the third design strategy, which guarantees satisfaction of the design specification both in the ρ-bounded and p-bounded

workspaces W_ρ and W_p^o. The latter is based on the following corollary combining results from Propositions 1 and 2.

Corollary 1. *If the prescribed symmetrical bounds $\mu(\mathbf{p}) \in [\mu, 1/\mu]$, $0 < \mu < 1$ are satisfied within the ρ-bounded workspace defined by the vertices Q^+, Q^-, then they are also satisfied within the p-bounded workspace defined by the vertices Q_*^+ and Q^-, with $p(Q_*^+) = \rho(Q^+) - 1$.*

These Propositions and Corollary give the designer three different methods ("design strategies") for computing the joint limits and dextrous Cartesian workspace of the normalised manipulator ($L = 1$), which afterwards must be scaled to achieve the prescribed workspace size. The methods are summarised in Table 3 and yield three Pareto-optimal solutions with respect to the design goals stated in Section 2. As follows from the propositions, all strategies ensure satisfaction of the design specification within the prescribed cubic workspace W_p, but differ by the manipulator performances in the remaining part $W_\rho \backslash W_p$. It should be noted, that the primary version of the first method, for $\mu \geqslant \mu^*$, was developed in the previous paper [16], while here it is generalised for the full range of the transmission factor.

It is obvious that correctness of the above statements for the transmission factor guarantees their correctness for the manipulability and condition number indices, which may be directly expressed via the singular values. Also, for real-life problems, the designer can prefer one of the solutions to other ones taking into account a number of additional engineering constraints and objectives, which cannot be implicitly expressed in the frames of the model used in this paper.

6. Numerical examples and discussions

To compare the proposed design approaches, let us apply them to the design of the Orthoglide for the unit Cartesian workspace $c \times c \times c$, $c = 1$ with the transmission factors bounds $0.5 \leqslant \mu \leqslant 2.0$. As stated above, the design process includes two main stages: (i) defining the joint limits ρ_{min}, ρ_{max} for the normalised manipulator with the link length $L = 1$, and (ii) scaling the manipulator parameters $(\rho_{min}, \rho_{max}, p_{min}, p_{max}, L)$ to achieve the prescribed workspace size.

For the normalised manipulator, the Q-axis technique gives the following ranges for the joint/Cartesian coordinates and corresponding transmission factors within the ρ- and p-bounded workspaces $\mu(W_\rho)$, $\mu(W_p)$, which are called below J-space and C-space, respectively (i.e. "Joint-coordinate bounded space" and "Cartesian-coordinate bounded space"):

J-space$_0$: $\rho \in [0.4082, 1.1785]$, $\Delta\rho = 0.7703$; $\mu(W_\rho) \in [0.50, 2.16]$,

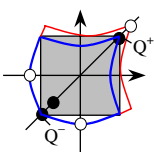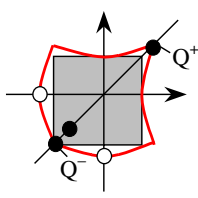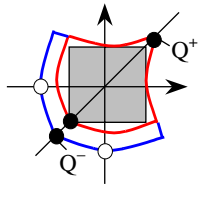C-space$_0$: $p \in [-0.4082, 0.2357]$, $\Delta\rho = 0.6440$; $\mu(W_p) \in [0.50, 2.00]$.

Strategy #1 assumes that the cube with the edge Δp is used as the prescribed Cartesian workspace. It requires increasing the upper joint limit to make all points of the cube attainable. According to Section 5.3, the enlarged joint space is defined as

J-space$_1$: $\rho \in [0.4082, 1.2357]$; $\Delta\rho = 0.8275$; $\mu(W_\rho) = [0.50, \infty[$.

So, since $\rho_{max} > \sqrt{1.5}$, the obtained ρ-bounded workspace includes parallel singularities, which may be eliminated by additional software constrains on the joint coordinates. For instance, the inequality $\rho_x + \rho_y + \rho_z \leqslant 3\rho_{Q^+}$ removes the singularities from W_ρ and restores the original transmission factors $[0.50, 2.16]$.

Table 3
Computing joint limits for the unit Orthoglide (dots on the Q-axis show location of Q^+, Q^- for different design strategies)

Design strategies	Remarks
Design strategy #1 (i) Compute points Q^+, Q^- to achieve required transmission factors along segment Q^+Q^- (ii) Locate the cube vertices in points Q^+, Q^- to define the cubic workspace W_p (iii) Adjust the joint limits to include the p-bounded workspace W_p inside the ρ-bounded one	 $\rho_{\min} = \rho_{Q^-}, \ \rho_{\max} = 1 + p_{Q^+}$ $p_{\min} = p_{Q^-}, \ p_{\max} = p_{Q^+}$ Inside the cube, design specifications are satisfied, but outside it, they are violated and even singularities exist if $\mu \leqslant 0.53$
Design strategy #2 (i) Compute points Q^+, Q^- to achieve required transmission factor along segment $Q^+ Q^-$ and set joint limits according to these points (ii) Inscribe the cube inside the ρ-bounded workspace W_ρ to define the cubic workspace W_p	 $\rho_{\min} = \rho_{Q^-}, \ \rho_{\max} = \rho_{Q^+}$ $p_{\min} = p_{Q^-}, \ p_{\max} = \rho_{Q^+} - 1$ Workspace is singularity-free but, outside the cube, performances are out of design specifications if $\mu < 0.54$
Design strategy #3 (i) Compute points Q^+, Q^- to achieve required transmission factor within the ρ-bounded workspace W_ρ and set according joint limits (ii) Inscribe the cube inside the ρ-bounded workspace W_ρ to define the cubic workspace W_p	 $\rho_{\min} = \rho_{Q^-}, \ \rho_{\max} = \rho_{Q^+}$ $p_{\min} = p_{Q^-}, \ p_{\max} = \rho_{Q^+} - 1$ Both ρ- and p-bounded workspaces are singularity-free and meet design specifications

Strategy #2 keeps the original ρ-bounded workspace, within which is located the prescribed cube. Computing relevant parameters gives:

C-space$_2$: $\quad p \in [-0.4082, 0.1785]; \quad \Delta p = 0.5868; \quad \mu(W_p) = [0.50, 2.00].$

In this case, the cube is smaller but the workspace is singularity-free and possesses reasonable kinematic properties both inside and outside the cube.

Strategy #3 provides the desired transmission factors for the whole ρ-bounded workspace, which is computed in accordance with Table 3 and is defined as

J-Space$_3$: $\rho \in [0.4472, 1.1785]$; $\Delta\rho = 0.7313$, $\mu(W_\rho) = [0.52, 2.00]$.

Then, inscribing the largest cube gives

C-Space$_3$: $p \in [-0.3884, 0.1785]$; $\Delta p = 0.5669$, $\mu(W_p) = [0.52, 1.87]$

that overtakes the required kinematic performances for the cube but ensures them for the whole ρ-bounded workspace.

After defining normalised manipulator parameters, the obtained cubic workspaces must be adjusted to the prescribed size $c \times c \times c$ by scaling the manipulator dimensions and joint/Cartesian coordinates. Computing the scaling factor $\eta = c/\Delta\rho$ for $c = 1$ yields 1.553, 1.704 and 1.764 for the first, second and third design strategies respectively. Design results after scaling are summarised in Table 4, which also contains ratio of the actuated joints range $\Delta\rho$ to the cube size c. These results shows that all obtained solutions are Pareto-optimal with respect to the vector criterion $(L, \mu_{min}, \mu_{max})$ with the goals $L \to$ min and $\mu_{min}, \mu_{max} \to 1.0$. Indeed, Strategy #1 yields the smallest Orthoglide dimensions (about 12% less than the third one), but the worst kinematic properties outside the cube (with singularities). In contrast, Strategy #3 guarantees the best kinematic performances for the price of the largest manipulator links, while Strategy #2 gives an intermediate solution ensuring the compromise between the link length and transmission factors. Hence, none of the strategies can be given a preference within the frames of the kinematic model and, in real-life applications, all these solutions should be presented to the designer who may evaluate them by taking into account a number of additional technical constraints and goals.

Finally, let us demonstrate application of the proposed technique to the design of the Orthoglide prototype, which has been built in Institut de Recherche en Communications et Cybernétique de Nantes (IRCCyN). The prescribed performances of the manipulator are: Cartesian velocity and acceleration in the isotropic point 1.2 m/s and 14 m/s^2; payload 4 kg; cubic Cartesian workspace size $200 \times 200 \times 200$ mm; transmission factor range 0.5–2.0. Application of the design strategies #1,...,3 yielded the Orthoglide link lengths 310.6, 340.9, 352.8 mm, respectively. Taking into account additional technical goals related to the manipulator mass and dynamic performances, the preference was given to the solution with the smallest link length. Corresponding joint limits are $\rho_{min} = 126.8$ mm and $\rho_{max} = 383.8$ mm. To remove singularities, the software constraint $\rho_x + \rho_y + \rho_z 3\rho_{Q^+}$ were used where $3\rho_{Q^+} = 1098.1$ mm. As follows from simulation and laboratory experiments, the prototype ensures required transmission factors within the prescribed cubic

Table 4
Orthoglide parameters and performances for $W_p = 1 \times 1 \times 1$ and $0.5 \leqslant \mu \leqslant 2.0$

Design strategy	L	ρ_{min}	ρ_{max}	$\Delta\rho$	$c/\Delta\rho$	$\mu(W_p)$	$\mu(W_\rho)$
#1	1.553	0.634	1.919	1.285	0.7782	0.500...2.000	Singularity
#2	1.704	0.696	2.009	1.313	0.7618	0.500...2.000	0.500...2.158
#3	1.764	0.789	2.079	1.290	0.7752	0.518...1.869	0.518...2.000

workspace [0.50, 2.00] and also their reasonable values outside the cube [0.50, 2.16]. However, during tuning of the control system, it was noticed rather high sensitivity of the kinematic performances with respect to the joint encoder offset. For instance, the 5 mm offset leads to changing of the Cartesian cube transmission factors to [0.50, 2.42]. The 10 mm offset increases their range up to [0.50, 3.42]. This imposes strict requirements on the assembly accuracy and motivates dedicated research on the Orthoglide calibration.

7. Conclusions

The paper focuses on the parametrical synthesis of the Orthoglide, a parallel manipulator for 3-axis rapid machining applications, which combines advantages of both serial mechanisms (regular workspace and homogeneous performances) and parallel kinematic architectures (good dynamic performances). Three strategies have been proposed to define the Orthoglide geometric parameters as functions of a cubic workspace size and dextrous properties expressed by bounds on the velocity transmission factors, manipulability or the Jacobian condition number. Low inertia and intrinsic stiffness have been set as additional design goals expressed by the minimal link length requirement.

In contrast to previous works, we proposed several Pareto-optimal solutions of the design problem, which differ by the manipulator performances outside the prescribed Cartesian cube (but within the workspace bounded by the actuated joint limits). Taking into account linear relation between the manipulator parameters and the cubic workspace size, the design process is decomposed in two stages: (i) defining the actuated joint limits and the largest cube size/location to satisfy the dexterity goals for the normalised manipulator; (ii) scaling the normalised manipulator to satisfy a specification on the cubic workspace size.

For each design strategy, we proposed analytical expressions for computing the Orthoglide parameters, which were based on the "critical points" concept that allows evaluating the global performance indices through the joint-bounded or cubic workspaces without their exhaustive exploration. We also proved two propositions describing relations between these workspace sizes and kinematic performances within them. It was shown, that independently of the applied strategy, the workspace includes the fully-isotropic point where any linear joint displacement yields similar manipulator tool displacement, like in a serial XYZ-machine. So, the synthesis is aimed at specifying the cubic volume around this point, which meets the dexterity goals. The related design parameters are the actuated joint limits and manipulator link lengths.

The proposed design strategies have been illustrated by numerical examples with the dexterity specification expressed by the velocity transmission factor. We obtained three Pareto-optimal solutions ensuring the required kinematic properties within the cubic workspace but providing wider range of the transmission factor outside the cube (this range is decreased monotonously while the manipulator link length is increased). Hence, no one of the strategies can be given a preference within the frames of the kinematic model and, in real-life applications, all the solutions should be presented to the designer who should evaluate them taking into account additional technical constraints and goals.

The developed technique has been also applied to the design of the Orthoglide prototype, which has been successfully built and tested in IRCCyN (Nantes, France). However, experiments with

this manipulator showed rather high sensitivity of the kinematic performances with respect to the joint encoder offsets, which motivates further research on the Orthoglide calibration.

References

[1] J.-P. Merlet, Parallel Robots, Kluwer Academic Publishers, Dordrecht, 2000.
[2] J. Tlusty, J.C. Ziegert, S. Ridgeway, Fundamental comparison of the use of serial and parallel kinematics for machine tools, CIRP Annals 48 (1) (1999) 351–356.
[3] P. Wenger, C. Gosselin, B. Maille, A comparative study of serial and parallel mechanism topologies for machine tools, in: Proceedings of PKM'99, Milan, Italy, 1999, pp. 23–32.
[4] L.W. Tsai, Robot Analysis: the Mechanics of Serial and Parallel Manipulators, John Wiley and Sons, New York, 1999.
[5] I. Bonev, The Parallel Mechanism Information Center, Available from: <http://www.parallemic.org>.
[6] J. Kim, C. Park, Performance analysis of parallel manipulator architectures for CNC machining applications, in: Proceedings of the IMECE Symposium on Machine Tools, Dallas, TX, 1997.
[7] Ph. Wenger, C. Gosselin D. Chablat, A Comparative Study of Parallel Kinematic Architectures for Machining Applications, in: Proceedings of the 2nd Workshop on Computational Kinematics, Seoul, Korea, 2001, pp. 249–258.
[8] F. Rehsteiner, R. Neugebauer, S. Spiewak, F. Wieland, Putting parallel kinematics machines (PKM) to productive work, CIRP Annals 48 (1) (1999) 345–350.
[9] C.-M. Luh, F.A. Adkins, E.J. Haug, C.C. Qui, Working capability analysis of Stewart platforms, Journal of Mechanical Design 118 (6) (1996) 89–91.
[10] J.-P. Merlet, Determination of 6D workspace of Gough-type parallel manipulator and comparison between different geometries, International Journal of Robotic Research 19 (9) (1999) 902–916.
[11] M. Carricato, V. Parenti-Castelli, Singularity-free fully-isotropic translational parallel mechanisms, International Journal of Robotics Research 21 (2) (2002) 161–174.
[12] X. Kong, C.M. Gosselin, A Class of 3-DOF Translational Parallel Manipulators with Linear I-O Equations, In: Workshop on Fundamental Issues and Future Research Directions for Parallel Mechanisms and Manipulators, Quebec, Canada, 2002, pp. 161–174.
[13] H.S. Kim, L.W. Tsai, Design optimization of a cartesian parallel manipulator, Journal of Mechanical Design 125 (1) (2003) 43–51.
[14] P. Wenger, D. Chablat, Kinematic analysis of a new parallel machine tool: The Orthoglide, in: J. Lenarčić, M.M. Stanisicć (Eds.), Advances in Robot Kinematic, Kluwer Academic Publishers, Norwell, MA, 2000, pp. 305–314.
[15] D. Chablat, P. Wenger, J.P. Merlet, Workspace analysis of the orthoglide using interval analysis, in: J. Lenarčić, F. Thomas (Eds.), Advances in Robot Kinematic, Kluwer Academic Publishers, Norwell, MA, 2002, pp. 397–406.
[16] D. Chablat, Ph. Wenger, Architecture optimization, of a 3-DOF parallel mechanism for machining applications the Orthoglide, IEEE Transactions On Robotics and Automation 19 (3) (2003) 403–410.
[17] A.Pashkevich, D. Chablat, P. Wenger, The Orthoglide: Kinematics and workspace analysis, 9th International Symposium on Advances in Robot Kinematic, Kluwer Academic Publishers, Norwell, MA, 2004.
[18] K.E. Zanganeh, J. Angeles, Kinematic isotropy and the optimum design of parallel manipulators, International Journal of Robotic Research 16 (2) (1997) 185–197.
[19] T. Huang, D. Whitehouse, Local dexterity, optimal architecture and optimal design of parallel machine tools, CIRP Annals 47 (1) (1998) 347–351.
[20] X.-J. Liu, Z.-L. Jin, F. Gao, Optimum design of 3-DOF spherical parallel manipulators with respect to the conditioning and stiffness indices, Mechanism and Machine Theory 35 (9) (2000) 1257–1267.
[21] T. Yoshikawa, Manipulability of robot mechanisms, International Journal of Robotic Research 4 (2) (1985) 3–9.

ELSEVIER

Parametric stiffness analysis of the Orthoglide

F. Majou [a,b], C. Gosselin [b], P. Wenger [a], D. Chablat [a,*]

[a] *Institut de Recherches en Communications et Cybernétique de Nantes, UMR CNRS 6597, 1 rue de la No, 44321 Nantes, France*
[b] *Département de Génie Mécanique, Université, Laval, Qué., Canada G1K 7P4*

Abstract

This paper presents a parametric stiffness analysis of the Orthoglide. A compliant modeling and a symbolic expression of the stiffness matrix are conducted. This allows a simple systematic analysis of the influence of the geometric design parameters and to quickly identify the critical link parameters. Our symbolic model is used to display the stiffest areas of the workspace for a specific machining task. Our approach can be applied to any parallel manipulator for which stiffness is a critical issue.
© 2006 Elsevier Ltd. All rights reserved.

Keywords: Parametric analysis; Stiffness; PKM design; Orthoglide

1. Introduction

Usually, parallel manipulators are claimed to offer good stiffness and accuracy properties, as well as good dynamic performances. This makes them attractive for innovative machine-tool structures for high speed machining [1–3]. When a parallel manipulator is intended to become a parallel kinematic machine (PKM), stiffness becomes a very important issue in its design [4–6]. This paper presents a parametric stiffness analysis of the Orthoglide, a 3-axis translational PKM prototype developed at IRCCyN [7].

Finite element methods (FEM) are mandatory to carry out the final design of a PKM [8]. However, a comprehensive three-dimensional FEM analysis may prove difficult, since one must repeatedly re-mesh the PKM structure to determine stiffness performances in the whole workspace, which is time consuming. Simpler and faster methods are needed at a pre-design stage. One of the first efficient stiffness analysis methods for parallel mechanisms was based on a kinetostatic modeling [9]. According to this approach, the stiffness of parallel mechanisms is mapped onto their workspace by taking into account the compliance of the actuated joints only. It is used and complemented in [10] to show the influence of the compliance of the prismatic joints as well as the torsional compliance of the links on the stiffness of the 3-*UPU* mechanism assembled for translation [11]. It is shown that the compliance of the links reduces the kinetostatic performances in a large part of

---

* Corresponding author. Tel.: +33 2 40 37 69 48; fax: +33 2 40 37 69 30.
  E-mail address: Damien.Chablat@irccyn.ec-nantes.fr (D. Chablat).

the workspace, compared to the stiffness model based on rigid links. Furthermore, the mobile platform can undergo small rotational motions because of the links' compliance, which departs from the expected translational kinematic behavior.

The analysis presented in [9] is not appropriate for PKM whose legs, unlike hexapods, are subject to bending [12]. This problem is solved in [13], where a stiffness estimation of a tripod-based overconstrained PKM is proposed. According to this approach, the PKM structure is decomposed into two substructures, one for the mechanism and another for the frame. One stiffness model is derived for each substructure. The superposition principle allows one to join the two models in order to derive the stiffness model of the whole structure. The influence of the geometrical parameters on the stiffness is also briefly studied. An interesting aspect of this method is that it can deal with overconstrained structures. However this stiffness model is not general enough. A more general model was proposed in [14]. The method is based on a flexible-link lumped parameter model that replaces the compliance of the links by localized virtual joints and rigid links. The latter approach differs from that presented in [13] on two main points, namely: (i) the modeling of the link compliances and (ii) the more general nature of the equations allowing the computation of the stiffness model.

In this paper, the method proposed in [14] is applied to the Orthoglide for a parametric stiffness analysis. A symbolic expression of the stiffness matrix is obtained which allows a global analysis of the influence of the Orthoglide's critical design parameters. No numerical computations are conducted until graphical results are generated. This paper is organized as follows: first the Orthoglide is presented. Then, the compliant model is introduced and the stiffness model is computed. Analytical expressions of the components of the stiffness matrix are obtained at the isotropic configuration, clearly showing the influence of each geometrical parameter. Finally, given a specific simulated machining task, it is shown how the general stiffness expressions allow one to easily display the stiffest subvolume of the Orthoglide's workspace.

2. Compliant modeling of the Orthoglide

2.1. Kinematic architecture of the Orthoglide

The Orthoglide is a translational 3-axis PKM prototype designed for machining applications. The mobile platform is connected to three orthogonal linear drives through three identical RP_aR serial chains (Fig. 1). Here, R stands for a revolute joint and P_a for a parallelogram-based joint. The Orthoglide moves in the Cartesian workspace while maintaining a fixed orientation. The Orthoglide was optimized for a prescribed workspace with prescribed kinetostatic performances [15]. Its kinematic analysis, design and optimization are fully described in [15].
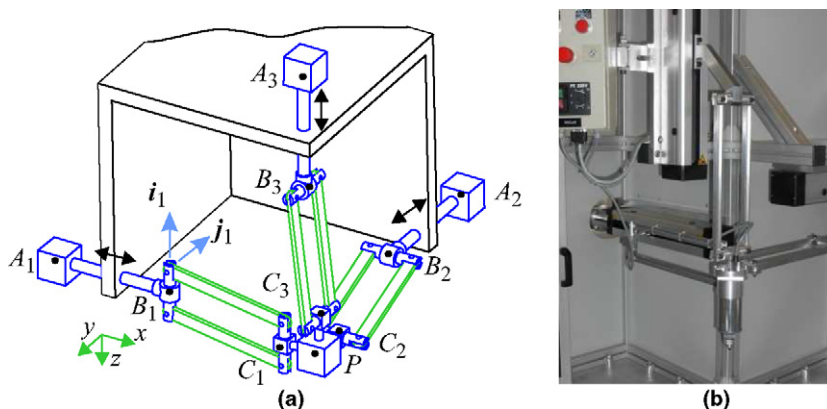

Fig. 1. The Orthoglide (a) kinematic architecture and (b) prototype.

2.2. Parameters for compliant modeling

The parameters used for the compliant modeling of the Orthoglide are presented in Fig. 2 and in Table 1. They correspond to a "beam-like" modeling of the Orthoglide legs' links. The foot has been designed to prevent each parallelogram from colliding with the corresponding linear motion guide. Three revolute joints are added, one on each leg (see Fig. 2), because the stiffness method used does not work with an overconstrained Orthoglide. This does not change the kinematics.

2.3. Compliant modeling with flexible links

In the lumped model described in [14], the leg links are considered as flexible beams and are replaced by rigid beams mounted on revolute joints plus torsional springs located at the joints (Fig. 3). Deriving the relationship between the force $\mathbf{F}$ and the deformation $y(x)$, the local torsional stiffness k can be computed:

$$EIy''(x) = F(L - x)$$
$$\vdots$$
$$EI_y(L) = FL^3/3$$
$$\rightarrow \theta \simeq y(L)/L = FL^2/3EI$$
$$k = FL/\theta$$
$$\rightarrow k = 3EI/L$$

If the Orthoglide leg actuator is locked, then one leg can withstand one force $\mathbf{F}$ and one torque $\mathbf{T}$ (Fig. 4), which are transmitted along the parallelogram bars and the foot. For a compliant modeling that uses virtual joints, it is important to understand how external forces are transmitted, and what their effect on the leg links is. Eight virtual joints are modeled along the Orthoglide leg. They are described in Table 2. The determination of all the virtual joint stiffnesses is not detailed here for brevity. However, they are derived based on the same principles used to calculate the torsional stiffness above.
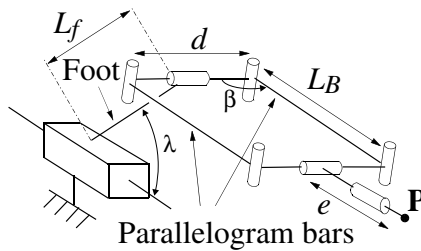

Fig. 2. Geometric parameters of the leg.

Table 1
Geometric parameters of the Orthoglide and dimensions of the prototype

| Parameter	Description	Values
L_f	Foot length, see Fig. 2	150 mm
h_f	Foot section sides	26 mm
b_f	Foot section sides	16 mm
$I_{f_1} = \frac{b_f.h_f^3}{12}$	Foot section moment of inertia 1	
$I_{f_2} = \frac{h_f.b_f^3}{12}$	Foot section moment of inertia 2	
$I_{f_0} = h_f.b_f(h_f^2 + b_f^2)/12$	Foot section polar quadratic moment	
λ	Angle between foot axis and actuated joint axis, see Fig. 2	45°
d	Distance between parallelogram bars, see Fig. 2	80 mm
L_B	Parallelogram bar length, see Fig. 2	310 mm
S_B	Parallelogram bar cross-section area	144 mm²
β	Rotation angle of the parallelogram	
e	See Fig. 2	
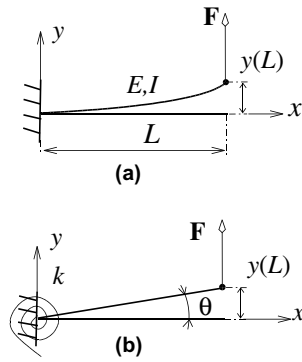
Fig. 3. General model for a flexible link: (a) flexible beam and (b) virtual rigid beam.
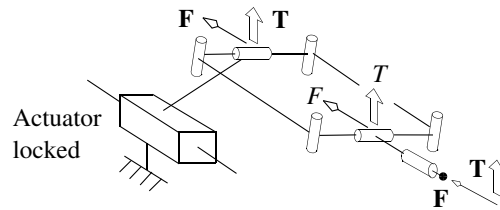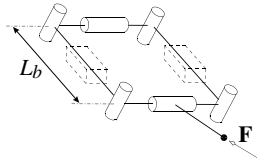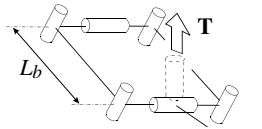

Fig. 4. Forces transmitted in a leg.

Table 2
Virtual joints modeling

Virtual joints i	Figure
$k_1 = k_{\text{act}}$: translational stiffness of the prismatic actuator	
$k_2 = \frac{3EI_{f_1}}{L_f}$: Foot bending due to force **F**	
$k_3 = \frac{2EI_{f_2}}{L_f}$: Foot bending due to torque **T**	
$k_4 = \frac{GI_{f_0}}{L_f}$: Foot tension due to torque **T**	
$k_5 = \frac{EI_{f_2}}{L_f}$: Foot section rotation due to torque **T**	

Table 2 (continued)

Virtual joints i	Figure
$k_8 = \frac{2ES_B}{L_B}$: Parallelogram bars tension/compression due to force $\mathbf{F}$	L_b $\mathbf{F}$
$k_{10} = \frac{ES_B d^2 \cos(\beta)}{2L_B}$: Differential tension of parallelogram bars due to Torque $\mathbf{T}$	$\mathbf{T}$ L_b

The actuated joint is assumed to be much stiffer than the virtual joints. The leg links compliances modeled in Table 2 were selected beforehand as the most significant ones. Indeed, selecting only the most significant compliances plays an important role in reducing the computing time required to derive the stiffness matrix symbolically (Par. 3). The kinematic joints' compliances are not taken into account because our purpose is to determine the links compliance influence only. Angle β is a parameter that depends on the Cartesian coordinates.

3. Symbolic derivation of the stiffness matrix

In this section, the derivation of the Orthoglide stiffness matrix—based on the virtual joints described in the previous section—is conducted with a stiffness model that was fully described in [14]. Therefore, the description of the model will only be summarized here. Fig. 5 represents the lumped model of a leg with flexible links. The Jacobian matrix $\mathbf{J}_i$ of the ith leg of the Orthoglide is obtained from the Denavit–Hartenberg parameters of the ith leg with flexible links. This matrix maps all leg joint rates (including the virtual joints) into the generalized velocity of the platform, i.e.,

$$\mathbf{J}_i \dot{\boldsymbol{\theta}}_i = \mathbf{t} \quad \text{where } \dot{\boldsymbol{\theta}}_i^{\mathrm{T}} = [\dot{\theta}_{i_1} \ \dot{\theta}_{i_2} \ \dot{\theta}_{i_3} \ \dot{\theta}_{i_4} \ \dot{\theta}_{i_5} \ \dot{\theta}_{i_6} \ \dot{\theta}_{i_7} \ \dot{\theta}_{i_8} \ \dot{\theta}_{i_9} \ \dot{\theta}_{i_{10}} \ \dot{\theta}_{i_{11}}]$$

is the vector containing the 11 actuated, passive and virtual joint rates of leg i and $\mathbf{t}$ is the twist of the platform. The P_a joint parameterization imposes $\dot{\theta}_{i_7} = -\dot{\theta}_{i_{7bis}}$, which makes $\dot{\theta}_{i_7}$ and $\dot{\theta}_{i_{7bis}}$, is dependent. $\dot{\theta}_{i_7}$ is chosen to model the circular translational motion, and finally $\mathbf{J}_i$ is written as

$$\mathbf{J}_i = \begin{bmatrix} 0, & \mathbf{e}_{i_2}, & \mathbf{e}_{i_3}, & \mathbf{e}_{i_4}, & \mathbf{e}_{i_5}, & \mathbf{e}_{i_6}, & 0, & 0, & \mathbf{e}_{i_9}, & \mathbf{e}_{i_{10}}, & \mathbf{e}_{i_{11}} \\ \mathbf{e}_{i_1}, & \mathbf{e}_{i_2} \times \mathbf{r}_{i_2}, & \mathbf{e}_{i_3} \times \mathbf{r}_{i_3}, & \mathbf{e}_{i_4} \times \mathbf{r}_{i_4}, & \mathbf{e}_{i_5} \times \mathbf{r}_{i_5}, & \mathbf{e}_{i_6} \times \mathbf{r}_{i_6}, & \mathbf{e}_{i_7} \times \mathbf{r}_{i_7}, & -\mathbf{e}_{i_{7bis}} \times \mathbf{r}_{i_{7bis}}, & \mathbf{e}_{i_8} \times \mathbf{r}_{i_8}, & \mathbf{e}_{i_9} \times \mathbf{r}_{i_9}, & \mathbf{e}_{i_{10}} \times \mathbf{r}_{i_{10}}, & \mathbf{e}_{i_{11}} \times \mathbf{r}_{i_{11}}, \end{bmatrix}$$
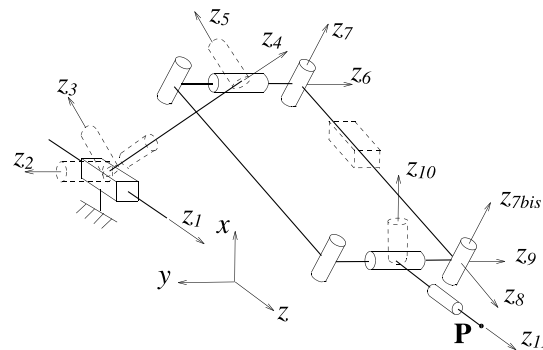

Fig. 5. Flexible leg.

in which $\mathbf{e}_{i_j}$ is the unit vector along joint j of leg i and $\mathbf{r}_{i_j}$ is the vector connecting joint j of leg i to the platform reference point. Therefore the Jacobian matrix of the Orthoglide can be written as

$$\mathbf{J} = \begin{bmatrix} \mathbf{J}_1 & \mathbf{0} & \mathbf{0} \\ \mathbf{0} & \mathbf{J}_2 & \mathbf{0} \\ \mathbf{0} & \mathbf{0} & \mathbf{J}_3 \end{bmatrix}$$

One then has

$$\mathbf{J}\dot{\boldsymbol{\theta}} = \mathbf{R}\mathbf{t} \text{ with } \mathbf{R} = \begin{bmatrix} \mathbf{I}_6 & \mathbf{I}_6 & \mathbf{I}_6 \end{bmatrix}^{\mathrm{T}} \quad \text{and} \quad \mathbf{t} = \begin{Bmatrix} \boldsymbol{\omega} \\ \mathbf{v} \end{Bmatrix} \tag{1}$$

$\dot{\boldsymbol{\theta}}$ being the vector of the 33 joint rates, that is $\dot{\boldsymbol{\theta}} = [\dot{\boldsymbol{\theta}}_1^{\mathrm{T}} \dot{\boldsymbol{\theta}}_2^{\mathrm{T}} \dot{\boldsymbol{\theta}}_3^{\mathrm{T}}]^{\mathrm{T}}$. $\mathbf{I}_6$ stands for the 6×6 identity matrix. Unactuated joints are then eliminated by writing the geometric conditions that constrain the two independent closed-loop kinematic chains of the Orthoglide kinematic structure:

$$\mathbf{J}_1\dot{\boldsymbol{\theta}}_1 = \mathbf{J}_2\dot{\boldsymbol{\theta}}_2 \quad \text{and} \quad \mathbf{J}_1\dot{\boldsymbol{\theta}}_1 = \mathbf{J}_3\dot{\boldsymbol{\theta}}_3 \tag{2}$$

From (2), one can obtain $\mathbf{A}\dot{\boldsymbol{\theta}}' = \mathbf{B}\dot{\boldsymbol{\theta}}''$ (see [14] for details), where $\dot{\boldsymbol{\theta}}'$ is the vector of joint rates without passive joints and $\dot{\boldsymbol{\theta}}''$ is the vector of joint rates with only passive joints. Hence:

$$\dot{\boldsymbol{\theta}}'' = \mathbf{B}^{-1}\mathbf{A}\dot{\boldsymbol{\theta}}'$$

Then a matrix $\mathbf{V}$ is obtained (see [14] for details) such that:

$$\dot{\boldsymbol{\theta}} = \mathbf{V}\dot{\boldsymbol{\theta}}' \tag{3}$$

From (1) and (3) one can obtain:

$$\mathbf{J}\mathbf{V}\dot{\boldsymbol{\theta}}' = \mathbf{R}\mathbf{t} \tag{4}$$

As matrix $\mathbf{R}$ represents a system of 18 compatible linear equations in 6 unknowns, one can use the least-square solution to obtain an exact solution from (4):

$$\mathbf{t} = (\mathbf{R}^{\mathrm{T}}\mathbf{R})^{-1}\mathbf{R}^{\mathrm{T}}\mathbf{J}\mathbf{V}\dot{\boldsymbol{\theta}}'$$

Now let $\mathbf{J}'$ be represented as $\mathbf{J}' = (\mathbf{R}^{\mathrm{T}}\mathbf{R})^{-1}\mathbf{R}^{\mathrm{T}}\mathbf{J}\mathbf{V}$. Then one has

$$\mathbf{t} = \mathbf{J}'\dot{\boldsymbol{\theta}}' \tag{5}$$

According to the principle of virtual work, one has

$$\boldsymbol{\tau}^{\mathrm{T}}\dot{\boldsymbol{\theta}}' = \mathbf{w}^{\mathrm{T}}\mathbf{t} \tag{6}$$

where $\boldsymbol{\tau}$ is the vector of forces and torques applied at each actuated or virtual joint and $\mathbf{w}$ is the external wrench applied at the end effector, point $\mathbf{P}$. Gravitational forces are neglected. By substituting (5) in (6), one can obtain:

$$\boldsymbol{\tau} = \mathbf{J}'^{\mathrm{T}}\mathbf{w} \tag{7}$$

The forces and displacements of each actuated or virtual joint can be related by Hooke's law, that is for the whole structure one has

$$\boldsymbol{\tau} = \mathbf{K}_J\Delta\boldsymbol{\theta}' \tag{8}$$

with

$$\mathbf{K}_J = \begin{bmatrix} \mathbf{A} & \mathbf{0} & \mathbf{0} \\ \mathbf{0} & \mathbf{A} & \mathbf{0} \\ \mathbf{0} & \mathbf{0} & \mathbf{A} \end{bmatrix}$$

and $\mathbf{A} = \mathrm{diag}\left(k_{\mathrm{act}}, \frac{3EI_{f_1}}{L_f}, \frac{2EI_{f_2}}{L_f}, \frac{GI_{f_O}}{L_f}, \frac{Eh_f b_f}{L_f}, \frac{EI_{f_2}}{L_f}, \frac{2ES_{\mathrm{B}}}{L_{\mathrm{B}}}, \frac{ES_{\mathrm{B}}d^2\cos(\beta)}{L_{\mathrm{B}}}\right)$.

$\Delta\boldsymbol{\theta}'$ only includes the actuated and virtual joints, that is by equating (7) with (8):

$$\mathbf{K}_J \Delta\boldsymbol{\theta}' = \mathbf{J}'^{\mathrm{T}}\mathbf{w}$$

Hence $\Delta\boldsymbol{\theta}' = \mathbf{K}_J^{-1}\mathbf{J}'^{\mathrm{T}}\mathbf{w}$. Pre-multiplying both sides by $\mathbf{J}'$ one obtains:

$$\mathbf{J}'\Delta\boldsymbol{\theta}' = \mathbf{J}'\mathbf{K}_J^{-1}\mathbf{J}'^{\mathrm{T}}\mathbf{w} \tag{9}$$

Substituting (5) into (9), one obtains:

$$\mathbf{d} = \mathbf{J}'\mathbf{K}_J^{-1}\mathbf{J}'^{\mathrm{T}}\mathbf{w}$$

with $\mathbf{d} = \mathbf{t}\Delta t$. Finally the compliance matrix $\boldsymbol{\kappa}$ is obtained as follows:

$$\boldsymbol{\kappa} = \mathbf{J}'\mathbf{K}_J^{-1}\mathbf{J}'^{\mathrm{T}}$$

In the Orthoglide case we obtain:

$$\boldsymbol{\kappa} = \begin{pmatrix} \kappa_{11} & 0 & 0 & \kappa_{14} & \kappa_{15} & \kappa_{16} \\ 0 & \kappa_{11} & 0 & \kappa_{24} & \kappa_{25} & \kappa_{26} \\ 0 & 0 & \kappa_{11} & \kappa_{34} & \kappa_{35} & \kappa_{36} \\ \kappa_{14} & \kappa_{24} & \kappa_{34} & \kappa_{44} & \kappa_{45} & \kappa_{46} \\ \kappa_{15} & \kappa_{25} & \kappa_{35} & \kappa_{45} & \kappa_{55} & \kappa_{56} \\ \kappa_{16} & \kappa_{26} & \kappa_{36} & \kappa_{46} & \kappa_{56} & \kappa_{66} \end{pmatrix} \tag{10}$$

And the Cartesian stiffness matrix is

$$\mathbf{K} = \boldsymbol{\kappa}^{-1} = (\mathbf{J}'\mathbf{K}_J^{-1}\mathbf{J}'^{\mathrm{T}})^{-1}$$

4. Parametric stiffness analysis at the isotropic configuration

In this section, we study the influence of the geometric parameters on the stiffness of the Orthoglide at the isotropic configuration, since this configuration provides a good evaluation of the overall performances [15]. Another interest is that the stiffness matrix is then diagonal which makes it easier to analyze.

4.1. Simple symbolic expressions

At the isotropic configuration, $\boldsymbol{\kappa}$ is diagonal and the symbolic expressions of the components κ_{ij} are simple. This is convenient because it is then possible to invert $\boldsymbol{\kappa}$ within a Maple worksheet and then analyze the symbolic expressions of the components of matrix $\mathbf{K}$. We have:

$$\mathbf{K} = \mathrm{diag}(K_a, K_a, K_a, K_b, K_b, K_b)$$

where K_a is the torsional stiffness and K_b is the translational stiffness.

$$K_a = \frac{E}{\dfrac{2L_{\mathrm{B}}}{S_{\mathrm{B}}d^2} + \dfrac{2L_p(78b_{\mathrm{f}}^2 + \cos^2\lambda(45h_{\mathrm{f}}^2 - 33b_{\mathrm{f}}^2))}{5h_{\mathrm{f}}b_{\mathrm{f}}^3(b_{\mathrm{f}}^2 + h_{\mathrm{f}}^2)}} \qquad K_b = \frac{1}{\dfrac{1}{k_{\mathrm{act}}} + \dfrac{L_{\mathrm{B}}}{2S_{\mathrm{B}}E} + \dfrac{4L_{\mathrm{f}}^3\sin^2\lambda}{Eh_{\mathrm{f}}^3b_{\mathrm{f}}}} \tag{11}$$

Analyzing the Orthoglide's stiffness at the isotropic configuration allows us to manipulate simple and meaningful symbolic expressions that are easy to interpret: this is the purpose of the following subsections.

4.2. Qualitative analysis of K_a and K_b

By inspection of the symbolic expression of K_a a few observations can be made:

- Young's modulus E appears at the numerator, which makes its influence easy to understand: when E increases, K_a increases, which is in accordance with intuition;

- The term $\frac{2L_B}{S_B d^2}$ shows the influence of virtual joint 10 (differential tension of parallelogram bars). When the bar length L_B increases or when S_B decreases, K_a decreases which is also in accordance with intuition. K_a decreases when d increases, which is a less intuitive result;[1]

- The expression $\frac{2L_p(78b_f^2 + \cos^2\lambda(45h_f^2 - 33b_f^2))}{5h_f b_f^3(b_f^2 + h_f^2)}$ shows the influence of virtual joints 3, 4 and 5 (foot bending and torsion). K_a decreases when L_f increases, which is not surprising. The degrees of h_f and b_f in the numerator and denominator of K_a tend to prove that the rotational stiffness increases with h_f or b_f, which is in accordance with intuition. The influence of λ depends on the sign of $(45h_f^2 - 33b_f^2)$.

Similarly, by inspection of the symbolic expression of K_b one notes:

- The term $\frac{1}{k_{act}}$ shows the influence of the prismatic actuator; it is not surprising that the translational stiffness increases when k_{act} increases. The term $\frac{L_B}{2S_B E}$ snows the influence of virtual joint 8 (parallelogram bars tension/compression): K_b increases when S_B or E increase, and decreases when L_B increases, which is in accordance with intuition;

- The term $\frac{4L_f^3 \sin^2\lambda}{E h_f^3 b_f}$ shows the influence of the *foot related* virtual joints (tension/compression and bending): when λ increases, with $\lambda \in [0\ \pi/2]$,[2] then $\sin^2\lambda$ increases and consequently K_b decreases. According to intuition, increasing L_f decreases K_b, while increasing h_f or b_f increases K_b.

4.3. Quantitative analysis of K_a and K_b

As we have seen, the qualitative analysis of K_a and K_b provides interesting information on the influence of the geometrical parameters on the rotational and translational stiffness. Quantitative information about the parameters' influence on the Orthoglide's stiffness can also be obtained from the symbolic expressions by studying the consequences of a $-100/+200\%$ variation of the parameters on K_a and K_b. A variation of -100% corresponds to a zero parameter, while $+200\%$ corresponds to an extreme increase. Such a wide range of variation gives a global picture of the parameter's influence. The initial values of the parameters used for the computation are given in Table 1 and correspond to the dimensions of the prototype of the Orthoglide developed at IRCCyN. Parameters k_{act} and E are considered constant because our analysis is restricted to geometrical parameters only. We choose $E = 7 \times 10^4$ N mm^{-2} (aluminum) and $k_{act} = 10^5$ N mm^{-1}. The stiffness of the actuated prismatic joint depends on many parameters (mechanical components, electrical motor power, control). The chosen value is a commonly used one, however it is still much stiffer than the virtual joints, which is in accordance with our assumptions.

In order to clearly show the relative influence of each parameter, we are going to superimpose several curves on a same chart. Each curve represents a ratio $\frac{K_a(t)}{K_{a_{initial}}}$ (resp. $\frac{K_b(t)}{K_{b_{initial}}}$), in which t is the percentage of variation of one of the parameters (L_f, b_f, h_f, λ, L_B, S_B or d), while the other parameters remain at their initial value, and $K_{a_{initial}}$ (resp. $K_{b_{initial}}$) is the initial value of the torsional (resp. translational) stiffness when the parameters are at their initial value. Obviously, all $\frac{K_a(t)}{K_{a_{initial}}}$ (resp. $\frac{K_b(t)}{K_{b_{initial}}}$) curves cross when $t = 0\%$.

For example let us replace each parameter in the symbolic expression of K_a by its initial value except L_f. A one variable analytical expression $K_a(L_f)$ is then obtained:

$$K_a(L_f) = \frac{0.56 \times 10^9}{L_f}$$

---

[1] Note that should d increase above a certain limit, other links compliances previously ruled out as less significant may then need to be taken into account.

[2] If $\lambda \geqslant \pi/2$ the foot does not anymore "move away" the parallelogram from the prismatic actuated joint, which is one of its main functions (i.e. avoiding collisions between the actuator and the parallelogram); furthermore we must have $\lambda \geqslant 0$ to avoid interference between the foot and the actuated prismatic joint.

In this expression, let us replace L_f by $L_{f_{initial}}(1 + t)$. A new expression $K_a(t)$ is obtained:

$$K_a(t) = \frac{0.56 \times 10^9}{150(1 + t)}$$

where t represents the percentage of variation of L_f. $K_a(t = 0)$ gives the value for $K_{a_{initial}}$. We assume that t varies from -100% to $+200\%$ as explained above. All $K_a(t)/K_{a_{initial}}$ curves obtained for all parameters are superimposed on a same chart so as to compare the parameters relative influence.

4.3.1. Quantitative analysis of K_a

Fig. 6 shows the influence of the parameters on K_a. L_B, d and S_B have little influence compared to L_f, h_f, b_f and λ.

$K_a(\lambda)$ is a maximum (52% increase) when λ increases by 100%, i.e. when $\lambda = \pi/2$. This result can also be obtained through observation of the symbolic expression of K_a: indeed, the initial values of h_f and b_f ($h_f = 26$, $b_f = 16$) make $(45h_f^2 - 33b_f^2)$ positive. Therefore, the denominator of K_a will be a minimum when $\lambda = \pi/2$. Moreover, when $\lambda = \pi/2$, the torque **T** that is transmitted by the leg no longer has a component along the axis of virtual joints 3 and 5 of the foot (Fig. 7). This is a physical explanation for $K_a(\lambda)$ being maximum when $\lambda = \pi/2$.

Furthermore, K_a increases more with b_f than with h_f for a same variation. Consequently, for a given foot weight increase, the torsional stiffness benefits more from an increase of b_f than from an increase of h_f. From a designer's point of view, this is valuable information. If the foot length L_f increases, K_a decreases since in this case the *foot and torque related* stiffness k_3, k_4, k_6 decrease. Conversely if L_f decreases then K_a increases tremendously.

Finally, we observe that when d, S_B, h_f or b_f tend towards zero, then so does K_a. This can be deduced from the symbolic expression of K_a, but also tends to a physical interpretation: if the foot or the parallelogram bars tend to have a very small cross section, or if the parallelogram tends not to be able to support any torque (when d tends towards zero), then the whole mechanism loses its torsional stiffness. Though h_f and λ play important roles in K_a, the two most important parameters are L_f and b_f.
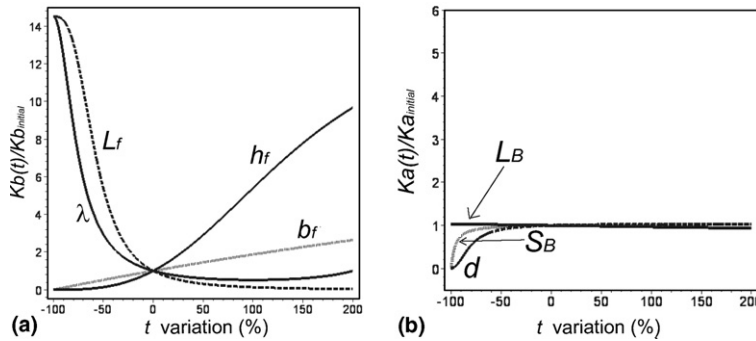

Fig. 6. Influence of the parameters on K_a. (a) $K_a(t)/K_{a_{initial}}$: most influent parameters and (b) $K_a(t)/K_{a_{initial}}$: least influent parameters.
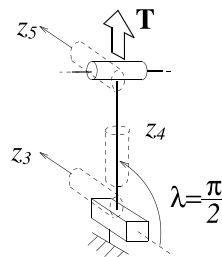

Fig. 7. Only virtual joints 4 of the foot is affected by **T** when $\lambda = \pi/2$.

4.3.2. Quantitative analysis of K_b

Fig. 8 shows the influence of the geometrical parameters on K_b. We can observe that L_B and S_B have little influence compared to L_f, h_f, b_f and λ. $K_b(\lambda)$ is a minimum (48% decrease) for a 100% increase of λ, i.e. when $\lambda = \pi/2$. This conclusion can be reached through the observation of the symbolic expression of K_b: indeed, we can see that the denominator of K_b will be a maximum when $\lambda = \pi/2$.

From the symbolic expression of K_b, one can also infer that if λ decreases, then the denominator will decrease and consequently K_b will increase. This was the opposite case for K_a. For a 100% decrease of λ, K_b will be a maximum: 14.4 times its initial value. This has a physical interpretation: when $\lambda = 0$, the virtual joint 2 is no longer affected by the force $\mathbf{F}$ that is transmitted by the leg (Fig. 9).

K_b is also a maximum (14.4 times its initial value) when $L_f = 0$. However, the physical interpretation is not the same. When $L_f = 0$, the stiffness of the virtual joints 2, 3, 4 and 5 tends toward $+\infty$ which makes them behave like infinitely stiff virtual joints, making the mechanism as a whole much more stiffer. One can also observe that K_b increases more with h_f than with b_f. This can be concluded from the symbolic expression of K_b. Indeed, from Eq. (11), we have:

$$K_b(h_f, b_f) = \frac{1}{0.00002537698413 + \frac{96.42857143}{h_f^3 b_f}}$$

Consequently, a 10% increase of h_f will make the denominator of K_b decrease faster than a 10% increase of b_f. Finally, if S_B, h_f or b_f tend towards zero, then K_b also tends towards zero. This can be concluded from the symbolic expression of K_b, but it also corresponds to the physical phenomenon that was explained for K_a.

The most important parameters for K_b are λ, L_f and h_f. Parameters λ and L_f have a similar influence: when they decrease, K_b increases, and conversely. Parameter h_f has the opposite influence: when h_f increases, K_b increases, and conversely. The symbolic expressions of K_b as univariate functions of these three parameters are of great help at a pre-design stage to analyze the translational stiffness.
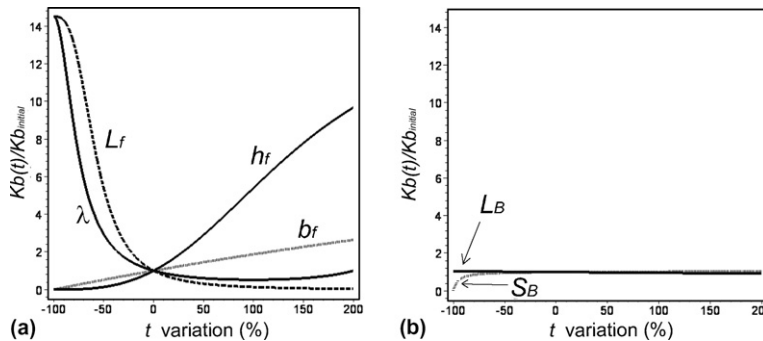

Fig. 8. Influence of the parameters on K_b: (a) $K_b(t)/K_{b_{initial}}$: most influent parameters and (b) $K_b(t)/K_{b_{initial}}$: least influent parameters.
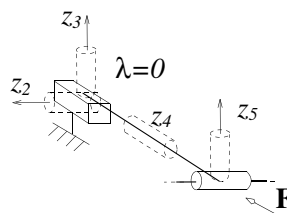

Fig. 9. Only virtual joint 3, 4 and 5 of the foot is affected by $\mathbf{F}$ when $\lambda = 0$.

4.4. Conclusions

The analysis of the symbolic expressions of K_a and K_b at the isotropic configuration allows us to plot the most influent parameters in this configuration, and the way their variation influences the mechanism's stiffness. A global analysis must be conducted in the whole workspace to determine the global influence of the parameters. This was achieved in [17], with the determination of a line along which the stiffness analysis results hold for the whole workspace. Such a procedure is required to simplify the global stiffness analysis. However, as mentioned above in the case of the Orthoglide, analyzing the stiffness at the isotropic configuration can give a good overview of the performances.

The use of simple symbolic expressions allows us to deduce helpful results in order to improve the Orthoglide's stiffness. However these modifications must be made while taking into account the technological constraints (collisions, interferences) of the prototype initial architecture. For example, if one sets λ to zero in order to increase K_b, then the offset between kinematic joints L_6 and L_1 disappears. However, this offset aims at preventing the parallelogram from colliding with the prismatic actuated joint. Therefore it is not possible to set L_f or λ to zero. It is better, either to only lower them and check how much the reachable workspace is then reduced, or to increase h_f, or both. Conversely, if one wants to increase the collision-free workspace by increasing L_f while keeping K_b constant, studying the simultaneous influence on the stiffness of L_f and h_f or L_f and b_f can then prove useful. One problem will be the foot weight increase that will require more powerful actuators to keep the dynamic performances at a similar level. We consider the issue of simultaneous variation of two parameters in the following section.

5. Influence of the simultaneous variation of two parameters

In this section, we study the influence on K_a and K_b of the simultaneous variation of two parameters L_f and h_f, or L_f and b_f, at the isotropic configuration. Analytical expressions of K_a and K_b as functions of two
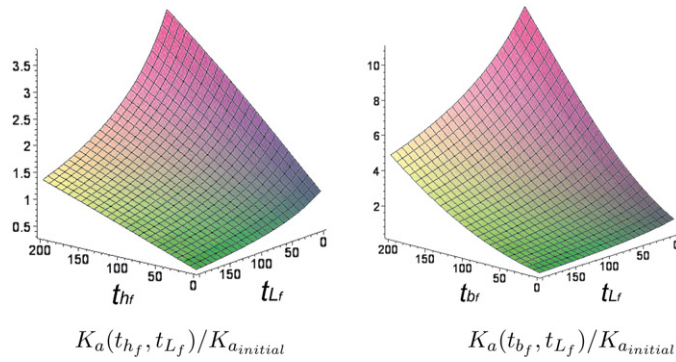

$$K_a(t_{h_f}, t_{L_f})/K_{a_{initial}} \qquad K_a(t_{b_f}, t_{L_f})/K_{a_{initial}}$$

Fig. 10. $K_a/K_{a_{initial}}$ as a function of h_f, b_f and L_f.

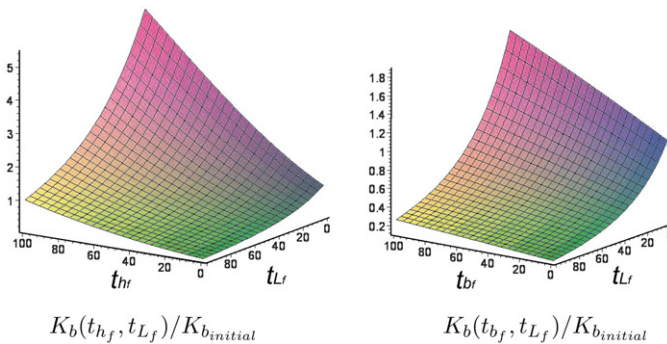$$K_b(t_{h_f}, t_{L_f})/K_{b_{initial}} \qquad K_b(t_{b_f}, t_{L_f})/K_{b_{initial}}$$

Fig. 11. $K_b/K_{b_{initial}}$ as a function of h_f, b_f and L_f.

variables are deduced from Eq. (11). Figs. 10 and 11 show plots of $K_a/K_{a_{initial}}$ and $K_b/K_{b_{initial}}$ when t_{h_f} (resp. t_{b_f})—which is the relative variation of h_f (resp. b_f)—and t_{L_f}—which is the relative variation of L_f—increase from 0% to 100% or 200% when relevant.

Fig. 10 shows that increasing h_f or b_f allows us to compensate for the decrease of K_a occurring when L_f increases. For example if L_f increases by 50%, h_f must increase by 34% or b_f must increase by 16% for K_a to remain at its initial value $K_{a_{initial}}$. Regarding the dynamic performances (i.e. the foot weight increase), it will be more interesting to increase b_f by 16%.

In Fig. 11, one can also observe that increasing h_f or b_f allows us to easily compensate for the decrease of K_b occurring when L_f increases. If L_f increases by 50%, h_f must increase by 48% or b_f must increase by 245% for K_b to remain at its initial value $K_{b_{initial}}$. Therefore, it seems more judicious to increase h_f rather than b_f in order to compensate for the stiffness loss due to the increase of L_f, because the foot weight increase is lower. This is a multi-criteria multi-parameters (L_f, h_f, b_f) optimization problem: increasing the collision-free workspace while keeping the same stiffness, with a minimum foot weight increase. Integrating the symbolic expressions of the stiffness in multicriteria optimization loops could be an interesting extension of our work.

6. Analysis of the tool displacements induced by external forces

Another interesting use of the symbolic expressions of κ_{ij} is to observe the tool compliant displacements when simulated cutting forces are applied on the tool. By multiplying these forces with the compliance matrix and analyzing the evolution of the compliant displacements obtained, as a function of the Cartesian coordinates, the stiffest zones of the mechanism's workspace can be determined. Thus, the global stiffness behavior is taken into account. As the simulated cutting forces correspond to a particular manufacturing operation, the stiffest zone will be specific to the application. The equations with which the stiffness matrix is computed are built using the principle of virtual work. Simulated cutting forces will then correspond to quasi-static conditions, which may not be realistic in some cases. In this section, a simple groove milling operation is simulated, which can be considered as a quasi-static operation.

The symbolic derivation of the stiffness matrix $\mathbf{K}$ using the method described above was achieved with Maple software on a 1 GHz, 256 MB RAM PC. The computation of $\mathbf{K}$ did not end within one day, which means that the components of matrix $\mathbf{K}$, i.e. the K_{ij}, are too large to be manipulated within a Maple worksheet. However, computing the components of the compliance matrix κ, i.e. the κ_{ij}, took 12 h only. This resulted in symbolic expressions that remained relatively easy to manipulate within a Maple worksheet. Therefore we choose to analyze the Orthoglide's stiffness through the analysis of the symbolic expressions of the κ_{ij}: the main idea is that when the κ_{ij} increase, then the Orthoglide's stiffness decreases.

6.1. Compliant displacements

Vector $\mathbf{w}$ is the static wrench of the cutting forces applied on the tool during the groove milling operation along the y-axis. We have

$$\mathbf{w} = \begin{Bmatrix} \mathbf{T} \\ \mathbf{F} \end{Bmatrix} \quad \text{with } \mathbf{F} = \begin{bmatrix} F_x & F_y & F_z \end{bmatrix}^T \quad \text{and} \quad \mathbf{T} = \begin{bmatrix} -F_y h_z & F_x h_z & 0 \end{bmatrix}^T \tag{12}$$

The compliant displacements of the mobile platform are computed as follows:

$$\mathbf{d} = \boldsymbol{\kappa}\mathbf{w} \quad \text{with } \mathbf{d} = \begin{Bmatrix} \boldsymbol{\Omega} \\ \mathbf{V} \end{Bmatrix}, \quad \boldsymbol{\Omega} = \begin{bmatrix} \omega_x & \omega_y & \omega_z \end{bmatrix}^T \quad \text{and} \quad \mathbf{V} = \begin{bmatrix} v_x & v_y & v_z \end{bmatrix}^T$$

The compliant displacements at the tool tip are then:

$$\mathbf{d}_{tool} = \begin{Bmatrix} \boldsymbol{\Omega} \\ \mathbf{V} + \boldsymbol{\Omega} \times h_z\mathbf{z} \end{Bmatrix}$$

6.2. Determination of the stiffest working zones for a given task

With the symbolic expressions of the tool displacement, one can evaluate the tracking error along the groove path. Using the symbolic expression of the tracking error, a stiffness favorable working zone, i.e. a working zone in which the tracking error is low, can be determined. To simulate cutting forces during the groove milling operation, a High Speed Machining (HSM) simulation software is used [18]. Depending on the manufacturing conditions, this software provides the average cutting forces. The manufacturing conditions chosen for the groove milling are:

- Spindle rate is $N = 20{,}000$ tr min^{-1};
- Feed rate $V_f = 40$ m min^{-1};
- Cutting thickness is 5×10^{-3} mm;
- The tool is a ball head of $\Phi = 10$ mm diameter with 2 steel blocks;
- Manufactured material is a common steel alloy with chromium and molybdenum.

The simulated cutting forces correspond to a HSM context, which is what PKM are $F_x = 215$ N, $F_y = -10$ N, $F_z = -25$ N. The above data allows us to simulate the tool compliant displacement along a groove path along the y-axis (see Fig. 12). $h_z = 100$ mm corresponds to the tool mounted on the prototype of the Orthoglide. The tracking error is the projection of the tool compliant displacement in the plane that is perpendicular to the path. We specify one groove path with its coordinates (x_t, z_t), and one point **P** with (x_t, y_P, z_t) coordinates located along this trajectory. The tracking error at point **P** is defined as $\delta_P = \sqrt{v_x^2 + v_z^2}$.

The paths are defined in a cube centered at the intersection of the prismatic joints, x_t and z_t vary within the interval $[-73.65; 126.35]$. We noticed that the maximum tracking errors were always located at one of the path ends. Fig. 13 shows the tracking error along a groove defined with the coordinates $(x_t, z_t) = (0, 0)$. We can see that the maximum error occurs when $y = -73.65$, i.e. at one of the path ends. Depending on the coordinates (x_t, z_t), the maximal tracking error is located at $y = -73.65$ or at $y = 126.35$. Fig. 14 shows the maximum
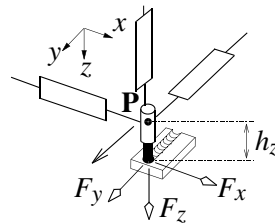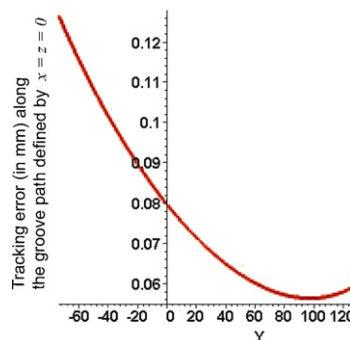

Fig. 12. Component forces of groove milling operation.

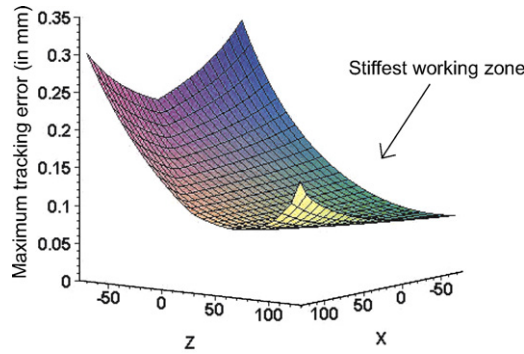Fig. 13. Tracking error along the groove path defined by $x = z = 0$.

Fig. 14. Maximum tracking error along y-axis groove paths.

tracking error for each groove path defined by its coordinates (x_t, z_t). The results clearly show a zone in which the maximum tracking error is low. In this working zone, x varies within the interval $[-73.65; 0]$ and z varies within $[50; 126.35]$. It is difficult to find a physical explanation for this result. It depends on the cutting forces applied, their magnitude and direction, and on each virtual joint reaction to the wrench transmitted by the leg, which depends on the Cartesian coordinates. The information obtained, i.e., the lowest tracking error working zone, is, however, of great interest for the end-user in order to place manufacturing paths in the workspace achieving the lowest tracking error due to structural compliance.

Another use of the symbolic expressions of the compliant displacements would be the optimization of the geometric parameters to minimize the tracking error for specific cutting forces. This would mean optimizing a PKM design for a specific task. Our opinion is that it is better to look for global stiffness improvement as we did in the previous section. This way, optimization brings stiffness improvement to all potential manufacturing tasks. However, given a PKM design, it is very interesting to determine the stiffest working zones for specific tasks, as we did in this section.

7. Comparison with a finite element stiffness model

By comparing our stiffness model with a finite element model (FEM) of the Orthoglide prototype, we will now show that our rigid link model is reasonably realistic [17]. A FEM was implemented in LARAMA (LAboratoire de Recherches en Automatique et Mécanique Avancée, Clermont-Ferrand, France) as part of a collaboration within project ROBEA, a research program sponsored by CNRS (Centre National de la Recherche Scientifique). Due to space limitations, the modeling assumptions of the FEM are not detailed here. The FEM allows to calculate the variation range of diagonal elements $\mathbf{Kt}_{1,1}$, $\mathbf{Kt}_{2,2}$, $\mathbf{Kt}_{3,3}$ of translational stiffness matrix $\mathbf{Kt}$, based on a CAD model of the Orthoglide implemented in the finite element software ANSYS [19]. The results obtained are presented in Table 3 (deterministic approximations and variation ranges) at the isotropic configuration. Our objective is to compare these results to those obtained with our Rigid Link Compliant Model (RLCM). Stiffnesses are expressed in N mm^{-1}. The numbers obtained from the FEM are comparable to those obtained from the RLCM. Even if deterministic values are not equal, this comparison shows that the RLCM of the Orthoglide is reliable enough for the purposes of pre-design. However, a more detailed FEM analysis and experimental results based on the Orthoglide prototype would be necessary to validate our RLCM. The main advantage of the RLCM is that it allows to spot critical links within the whole workspace

Table 3
Comparison of the RLCM and the FEM

	$\mathbf{Kt}_{1,1}$		$\mathbf{Kt}_{2,2}$		$\mathbf{Kt}_{3,3}$	
	FEM	RLCM	FEM	RLCM	FEM	RLCM
Isotropic configuration	3500	2715	3500/4000	2715	3500/4000	2715

much more easily and quickly than the FEM, because of the symbolic expressions of stiffness matrix elements. The RLCM is easier to use than a FEM at a pre-design stage. Once the RLCM is proved reliable enough, one can use it either to test alternative designs or choose manufacturing paths reducing the tool compliant displacement (tracking error or tracking rotational and translational compliant displacements) caused by structural compliance. Unfortunately, the FEM did not provide any results for the rotational compliance. This would be an interesting comparison since it would allow a verification of whether or not the torsional stiffness of the mobile platform obtained with the RLCM is lower compared to that of the overconstrained Orthoglide prototype described in [15,16] and modeled in the FEM.

8. Conclusions

In this paper, a parametric stiffness analysis of a 3-axis PKM prototype, the Orthoglide, was conducted. First, a compliant model of the Orthoglide was obtained, then a method for parallel manipulators stiffness analysis was applied, and the stiffness matrix elements were computed symbolically in the isotropic configuration. In this configuration, the influence of the geometric design parameters on the rotational and translational stiffness was studied through qualitative and quantitative analysis. The analysis provided relevant and precise information for stiffness-oriented optimization of the Orthoglide. Then, the analysis of the simultaneous influence on the stiffness of two variable parameters was conducted. Such an analysis is very useful to take into account both stiffness and another performance criterion such as workspace volume or the maximal acceleration of the mobile platform. Finally, we used the symbolic expressions of the components of the compliance matrix to determine the stiffest working zone for a specific manufacturing task. The stiffest zone depends on the task and applied cutting forces. The parametric stiffness analysis shows that simple symbolic expressions carefully built and interpreted provide much information on the stiffness features of parallel manipulators, which can be relevantly used for their design and optimization.

References

[1] J. Tlusty, J. Ziegert, S. Ridgeway, Fundamental comparison of the use of serial and parallel kinematics for machine tools, Annals of the CIRP 48 (1) (1999).
[2] P. Wenger, C.M. Gosselin, B. Maillé, A comparative study of serial and parallel mechanism topologies for machine tools, PKM'99, Milano, 1999, pp. 23–32.
[3] F. Majou, P. Wenger, D. Chablat, The design of parallel kinematic machine tools using kinetostatic performance criteria, in: 3rd International Conference on Metal Cutting and High Speed Machining, Metz, France, June 2001.
[4] G. Pritschow, K.-H. Wurst, Systematic design of hexapods and other parallel link systems, Annals of the CIRP 46 (1) (1997) 291–295.
[5] O. Company, F. Pierrot, Modelling and design issues of a 3-axis parallel machine-tool, Mechanism and Machine Theory 37 (2002) 1325–1345.
[6] T. Brogardh, PKM Research—Important Issues, as seen from a Product Development Perspective at ABB Robotics, Workshop on Fundamental Issues and Future Research Directions for Parallel Mechanisms and Manipulators, Quebec, Canada, October 2002.
[7] P. Wenger, D. Chablat, Kinematic Analysis of a new parallel machine tool, in: 7th International Symposium on Advances in Robot Kinematics, Piran-Portoroz, Slovenia, June 2000, pp. 305–314.
[8] B.C. Bouzgarrou, J.C. Fauroux, G. Gogu, Y. Heerah, Rigidity analysis of T3R1 parallel robot uncoupled kinematics, in: Proceedings of the 35th International Symposium on Robotics, Paris, March 2004.
[9] C.M. Gosselin, Stiffness mapping for parallel manipulators, IEEE Transactions on Robotics and Automation 6 (1990) 377–382.
[10] R. Di Gregorio, V. Parenti-Castelli, Influence of leg flexibility on the kinetostatic behavior of a 3-DOF fully parallel manipulator, in: 10th World Congress on the Theory of Machines and Mechanisms, Oulu, Finland, June 1999.
[11] L.-W. Tsai, S. Joshi, Kinematics and optimization of a spatial 3-UPU parallel manipulator, ASME Journal of Mechanical Design 122 (2000) 439–446.
[12] X. Kong, C.M. Gosselin, Kinematics and singularity analysis of a novel type of 3-CRR 3-DOF translational parallel manipulator, The International Journal of Robotics Research 21 (9) (2002) 791–798.
[13] T. Huang, X. Zhao, D.J. Whitehouse, Stiffness estimation of a tripod-based parallel kinematic machine, IEEE Transactions on Robotics and Automation 18 (1) (2002) 50–58.
[14] C.M. Gosselin, D. Zhang, Stiffness analysis of parallel mechanisms using a lumped model, International Journal of Robotics and Automation 17 (1) (2002) 17–27.
[15] D. Chablat, P. Wenger, Architecture optimization of the Orthoglide, a 3-DOF parallel mechanism for machining applications, IEEE Transactions on Robotics and Automation 19 (3) (2003) 403–410.
[16] www.irccyn.ec-nantes.fr/~wenger/Orthoglide, Orthoglide Web site, June 2002.

[17] F. Majou, Kinetostatic analysis of translational parallel kinematic machines, Ph.D. thesis, Université Laval, Québec, Canada and École Centrale Nantes, France, September 2004.

[18] A. Dugas, J.J. Lee, M. Terrier, J.Y. Hascoët, Virtual manufacturing for high speed milling, in: 35th CIRP International Seminar on Manufacturing Systems, Seoul, Korea, May 13–15, 2002, pp. 199–205.

[19] R. Abiven, Étude des rigidités statique et dynamique du robot Orthoglide, Master thesis, Université Blaise Pascal, IFMA, 2002.